MULTIFUNCTIONAL NANOMATERIALS FOR ADVANCED MOLECULAR IMAGING AND CANCER THERAPY

BY PRASAD SUBRAMANIAM

A dissertation submitted to the

Graduate School—New Brunswick

Rutgers, The State University of New Jersey

in partial fulfillment of the requirements

for the degree of

Doctor of Philosophy

Graduate Program in Chemistry and Chemical Biology

Written under the direction of

Professor Ki-Bum Lee

and approved by

_____

_____

_____

_____

New Brunswick, New Jersey

January, 2014

ABSTRACT OF THE DISSERTATION

Multifunctional Nanomaterials for Advanced Molecular Imaging and Cancer Therapy

by PRASAD SUBRAMANIAM

Dissertation Director: Professor Ki-Bum Lee

Nanotechnology offers tremendous potential for use in biomedical applications, including cancer and stem cell imaging, disease diagnosis and drug delivery. The development of nanosystems has aided in understanding the molecular mechanisms of many diseases and permitted the controlled nanoscale manipulation of biological phenomena. In recent years, many studies have focused on the use of several kinds of nanomaterials for cancer and stem cell imaging and also for the delivery of anticancer therapeutics to tumor cells. However, the proper diagnosis and treatment of aggressive tumors such as brain and breast cancer requires highly sensitive diagnostic agents, in addition to the ability to deliver multiple therapeutics using a single platform to the target cells. Addressing these challenges, novel multifunctional nanomaterial-based platforms that incorporate multiple therapeutic and diagnostic agents, with superior molecular imaging and targeting capabilities, have been presented in this work.

The initial part of this work presents the development of novel nanomaterials with superior optical properties for efficiently delivering soluble cues such as small interfering RNA (siRNA) into brain cancer cells with minimal toxicity. Specifically, this section details the development of non-toxic quantums dots for the imaging and delivery of siRNA into brain cancer and mesenchymal stem cells, with the hope of using these

quantum dots as multiplexed imaging and delivery vehicles. The use of these quantum dots could overcome the toxicity issues associated with the use of conventional quantum dots, enabled the imaging of brain cancer and stem cells with high efficiency and allowed for the delivery of siRNA to knockdown the target oncogene in brain cancer cells.

The latter part of this thesis details the development of nanomaterial-based drug delivery platforms for the co-delivery of multiple anticancer drugs to brain tumor cells. In particular, this part of the thesis focuses on the synthesis and use of a biodegradable dendritic polypeptide-based nanocarrier for the delivery of multiple anticancer drugs and siRNA to brain tumor cells. The co-delivery of important anticancer agents using a single platform was shown to increase the efficacy of the drugs manyfold, ensuring the cancer cell-specific delivery and minimizing dose limiting toxicities of the individual drugs. This would be of immense importance when used *in vivo*.

Acknowledgements

At the outset, I would like to express my deepest gratitude to my principal advisor, Prof. Ki-Bum Lee, for his limitless commitment to my work, for always prioritizing my interests, for educating and training me in all the methods and skills required for the completion of this thesis and for imparting in me his thorough and keen sense of perfection. I will always remember his words that Ph.D. is not just about doing research and publishing papers, it is about learning to be able to manage your resources well to be self-reliant and successful after the completion of the Ph.D. While several students often struggle with supervisors being very busy, there was never any time which was inconvenient to knock on his door. Even random meetings in the corridors turned into lab meetings. Most importantly, I would like to thank him for being a friend than an advisor, with whom I could talk about anything. He has always shared his experiences with me, trying to remind me not to make the same mistakes he made. Being one of his first students was a really enriching experience, and has prepared me well for a position in any career path I choose. I really thank him from the bottom of my heart and I thank God for giving me the opportunity to work with him.

I would also like to thank Prof. Eric Garfunkel, Prof. Ralf Warmuth and Prof. Nanjoo Suh for being a part of my thesis committee and providing valuable guidance throughout the years. Their constant support and words of encouragement through the tenure of my graduate study really helped me a lot. I would also like to thank all my collaborators, namely Prof. Junfeng Zhang, Dr. Gediminas Mainelis, Prof. Stephan Schwander, Lin Zhang, Valentin Starovoytov and Dr. Gunyoung Jung for their support in various projects.

I would like to express my gratitude to all the members of the KB Lee group. As one of the earliest members of this very diverse group, I have watched it grow over

the years and it has been a great pleasure in working with such intelligent and caring people. I still remember the days when we did not have any working lab space and how we set our lab up to become one of the most interdisciplinary and successful labs in the department. I would specifically like to thank Dr. Aniruddh Solanki and Birju Shah, who were there with me from the onset of my graduate study and who also happen to be my good friends in the department. I have shared numerous good and bad days with them in the lab and I'm grateful to them for everything they have done for me over the years. Ani, as you venture into your new job as a Postdoctoral Associate, I wish you the very best in everything you do. Birju, I wish you luck with your Ph.D. and also for taking over the reins as the unofficial lab manager. I will really miss you both. I would also like to thank Shreyas Shah, Sahishnu Patel and Sy-Tsong Chueng, for their help and support and for providing a lively atmosphere in the lab. Our days of playing fantasy football and mortal kombat videogames will definitely be one of the memorable moments spent with you guys. I would like to express my gratitude to all past and present group members, including postdoctoral associates and undergraduate students, who have contributed directly or indirectly to my thesis.

Pursuing a Ph.D. is one of the the most trying and difficult phases of a student's life, and its in this phase that friends and family provide a vital support, both mentally and physically. I'm blessed to have had the best of friends back home and here at Rutgers, on whom I could lean on during my bad days. I am greatly indebted to Soma Mandal, Dr. Deepankar Das, Satish Reddy Sangem, Manik Dhawan, Saket Kharsikar and Rochak Vig for being there for me all through these 5 years and for providing the love and support that one yearns for while being away from family. I will cherish each and every moment spent with you guys through these years. Another person, who has been the most vital for my existence here at Rutgers is Nisha Mittal. Words cannot express what she has done for me. She has always been there for all the problems I have had in my life, personal and professional. Her presence and words have helped me get back on track in my trying times. She has been more a sister to me than a friend and I thank her from the bottom of my heart for her unconditional love, care and support. I am not sure what I would have done without her help. I also wish to thank Dr. Vaishali

Thakral, an excellent scientist and my friend and sister, for her technical help on one of my projects and for her love and support, both personally and professionally.

Finally, I would like to thank my family for their love and blessings. I would first like to thank my parents, who made sure that I got the best education back home and without whom I would not have achieved so much in life. Despite all the trying times they had to go through in their life, they made sure that I did not suffer in any manner. I thank them for their blessings, love and care over all these years. I also wish to thank my brother, Dr. Prakash Subramayam and sister-in-law Dr. Aditi Bhattacharya, excellent neuroscientists themselves, for their guidance and love. I always looked up to them as role models and tried to emulate whatever they did. Lastly, I would like to thank my wife Smita Deivanayagam for her loving support during the last stages of my PhD. This has included listening to my endless scientific ramblings and not being able to give her enough time because of my experiments in lab. This PhD would not have been possible without her.

Dedication

I would like to dedicate this work to my parents A.V. Subramaniam and Shyamala Subramanyam, who have worked all their life for making sure I can achieve all my dreams. I would also like to dedicate this work to my late grandparents, who always wanted me to be succcessful in whatever I do and who are constantly showering their choicest blessings from above. Lastly, this work is dedicated to my and wife Smita Deivanayagam, my brother Dr. Prakash Subramanyam and sister-in-law Dr. Aditi Bhattarcharya, and all my friends here and back home for standing by me through this journey.

Table of Contents

Abstract ii

Acknowledgements iv

Dedication vii

List of Figures xii

1. Introduction 1

1.1. Nanomaterial-based Molecular Imaging and Multimodal Diagnostic Agents 4

1.1.1. Plasmonic Nanoparticles 6

1.1.2. Magnetic Nanoparticles 11

1.1.3. Fluorescent Nanoparticles 19

1.2. Nanomaterials for Drug Delivery and Effective Cancer Therapy 29

1.2.1. Inorganic Nanomaterials 30

Magnetic Nanoparticles 30

Gold Nanoparticles 39

1.2.2. Engineered Organic Nanomaterials 43

Dendrimers 43

Liposomes 46

1.2.3. Biodegradable Nanomaterials 50

PLGA Nanoparticles 50

Polypeptides 54

1.3. Conclusion 59

1.4. Overview of Dissertation 61

2. Nanomaterial-based Molecular Imaging and Multimodal Diagnostic Agents 63

2.1. Generation of a Library of Non-toxic Quantum Dots for Cellular Imaging and siRNA Delivery 64

2.1.1. Introduction 64

2.1.2. Results and Discussion 65

The photoluminescence of ZAIS QDs is composition-dependent and not size dependent 66

Physical characterization of the ZAIS QDs 68

ZAIS QDs as biocompatible and non-toxic molecular imaging probes 72

ZAIS QDs for simultaneous imaging and delivery of siRNA . . . 77

2.1.3. Conclusions 80

2.1.4. Materials and Methods 80

Synthesis of precursor complexes 81

Sonochemical synthesis of dodecylamine-capped ZnS-$AgInS_2$ quantum dots 81

Surface modification of ZAIS-QDs with 3-mercaptopropionic acid (MPA) 81

Physical characterization of the ZAIS QDs 82

Determination of PL stability of ZAIS QDs 82

Culture of human U87 glioblastoma cells, NIH-3T3 mouse fibroblasts and human mesenchymal stem cells 83

Cell viability assays 83

Cellular imaging using fluorescence microscopy 84

Cellular transmission electron microscopy 84

Attachment of siRNA to the MPA-coated ZAIS QDs 85

Culture of human U87-EGFP cells for siRNA knockdown experiments 85

Cytotoxicity assessment of ZAIS QDs in oxidative environment . 86

3. Nanomaterials for Drug Delivery and Effective Cancer Therapy . . 87

3.1. Dendritic Polypeptide-based Nanocarrier for the Delivery of Multiple Anticancer Drugs and siRNA to Brain Tumor Cells 88

3.1.1. Introduction 88

3.1.2. Results and Discussion 91

Synthesis of and characterization of the dendritic polypeptide . . 91

Loading multiple anticancer drugs onto the dendritic polypeptide 93

Controlled release of DOX and HDACi from polypeptide 96

Polypeptide-mediated delivery increases the efficacy of DOX and HDACi 98

Polypeptide-mediated siRNA delivery 100

Polypeptide-mediated codelivery of DOX and EGFRvIII siRNA to brain tumor cells 104

3.1.3. Conclusions 105

3.1.4. Materials and Methods 106

Synthesis of the thiol-based HDAC inhibitor 107

Synthesis of amino acid N-carboxy anhydrides (NCAs) 108

Synthesis of the polypeptide (with and without histidine) 109

Conjugation of DOX and HDACi to the polypeptide 110

MALDI-TOF Analysis 111

DLS and Zeta potential measurements 111

Loading efficiency of DOX and HDACi onto the polypeptide . . 111

pH-mediated DOX release from polypeptide 112

Glutathione-mediated HDACi release from polypeptide 112

Culture of human U87 glioblastoma cells and HeLa cells 113

Assessment of cytoxicity of HDACi and DOX in DMSO 113

Assessment of HDAC inhibition capability of synthesized HDACi 113

Assessment of cytoxicity of polypeptide-drug conjugates 114
Assesment of siRNA uptake and targeted delivery of Polypeptide-RGD-siRNA 114
Assessment of GFP knockdown using polypeptide-siEGFP 115
Delivery of polypeptide-DOX-siEGFRvIII 116

4. Conclusions and Perspectives 117

References 119

List of Figures

1.1. Range of scale of biomolecular interactions 2

1.2. Applications of nanotechnology in biology and medicine. 3

1.3. Schematic illustration of the optical properties of metallic nanoparticles for surface–enhaced Raman spectroscopy 7

1.4. Schematic illustration of the working Mechanism of MBA/SMART-AuNP in a melanoma cell 8

1.5. Molecular-specific imaging of cancer using gold nanoparticle/anti-EGFR conjugates 9

1.6. Immunotargeted gold nanoshells for *in vivo* imaging of breast cancer . . 11

1.7. Cancer cells labeled with iron oxide nanoparticles 12

1.8. Activation of cellular signaling processes by magnetized nanoparticles . 13

1.9. MRI of NP treated transgenic breast cancer mice 14

1.10. MRI/NIRF/PET trimodal imaging with SPIONs 16

1.11. Labeling of hMSCs using magnetized nanoparticles for tumor tropism . 17

1.12. Excitation and emission spectra of quantum dots in comparison to dyes and proteins 20

1.13. Multiplexed QD–IHC images of clinical prostate tissue specimens and quantitative analysis of cancer biomarkers 22

1.14. Accurate HER2 testing by QDs–IHC 23

1.15. *In vivo* NIR fluorescence imaging of U87MG tumor-bearing mice injected with RGD-QDs 24

1.16. *In vivo* fluorescence imaging of MCF–7/HER2 xenografts labeled with QD-immunoliposomes 25

1.17. Mesenchymal stem cells labeled with quantum dots 26

1.18. Multiplex imaging of embryonic stem cells labeled with quantum dots . 27
1.19. Nanomaterials for drug delivery and cancer therapy 30
1.20. Applications of Magnetic nanoparticles in drug delivery and biomedical research 31
1.21. MTX-modified SPIONs for the targeted delivery into breast cancer cells 32
1.22. Multifunctional magneto-polymeric nanohybrids for targeted detection and synergistic therapeutic effects on breast cancer 34
1.23. Schematic drawing of all-in-one nanoparticles of $MnFe_2O_4$–siGFP–Cy5/PEG–RGD for theranostics 35
1.24. A schematic representation of some of the unique advantages of magnetic nanomaterials for hyperthermia-based therapy and controlled drug delivery 37
1.25. Magnetically–triggered drug release system 38
1.26. Photothermal therapy using MBA/SMART-AuNPs 40
1.27. Photothermal effect of HER2-conjugated Au nanocagesNPs 41
1.28. Dendrimer-based gene delivery into mesenchymal stem cells 45
1.29. Tracking neural stem cells labeled with magnetodendrimers 46
1.30. Synthesis and functionalization of liposomes to confer multifunctionality for drug delivery and imaging 47
1.31. Liposomal co-delivery of siRNA and Doxorubiciin for overcoming multidrug resistance 48
1.32. Multifunctional PLGA nanoparticles for targeted and efficient drug delivery to tumors 50
1.33. Schematic illustration of the PLGA nanoparticles for co-delivery of docetaxel and doxorubicin 52
1.34. Convection-enhanced delivery of camptothecin-loaded polymer nanoparticles for treatment of intracranial tumors 53
1.35. Applications of cell -penetrating peptides as molecular delivery vehicles 55
1.36. Small molecule therapeutics successfully delivered by CPPs 56
1.37. CPP–mediated delivery of imaging and diagnostic agents 57

1.38. Schematic diagram of activatable CPPs 58
2.1. Synthesis of a library of ZnS-$AgInS_2$ QDs for simultaneous imaging and delivery of siRNA 66
2.2. Photoluminescent properties of the ZAIS QD library 67
2.3. Physical characterization of the Zn_xS-$Ag_yIn_{1-y}S_2$ QDs 69
2.4. Hydrodynamic size of the ZAIS QD 70
2.5. Quantum yields of ZAIS QDs 71
2.6. Colloidal and PL stability of ZAIS QDs 71
2.7. Colloidal and PL stability of ZAIS QDs at physiological conditions . . . 72
2.8. Biocompatibility and cellular imaging studies of ZAIS-QDs in mammalian cells 74
2.9. Cellular cytotoxicity of select ZAIS QD compositions in normal (NIH-3T3 mouse fibroblasts) cells 75
2.10. Cellular cytotoxicity of water-soluble ZAIS QD in an oxidative environment 76
2.11. Zeta potential measurements of ZAIS QD-MPA-PEI-siRNA to ensure appropriate layer-by-layer coating 78
2.12. *In vitro* testing of the ZAIS-QD-siEGFP cell uptake and silencing efficiency in stably transfected U87-EGFP glioblastoma cells 79
3.1. Schematic of the dendritic polypeptide for the stimuli responsive-release of multiple anticancer therapeutics 91
3.2. Synthesis of the dendritic polypeptide and subsequent conjugation of drugs 92
3.3. Measurement of the molecular weight of the polypeptide 93
3.4. Hydrodynamic size and surface charge of the polypeptide-drug conjugates 96
3.5. Stimuli-sensitive controlled release of the DOX and HDACi from the polypeptide 97
3.6. Stimuli-sensitive controlled release of the DOX and HDACi from the polypeptide 98
3.7. HDAC inhibition assay of the new HDACi (SAHA analogue) 99
3.8. Polypeptide-mediated siRNA uptake, release and gene knockdown . . . 102

3.9. Uptake and release of Cy-3 labeled siRNA using polypeptide lacking the histidine residues 103
3.10. Targeted delivery of Cy3®-labeled siRNA using our polypeptide 104
3.11. Synergistic inhibition of brain tumor cell proliferation by codelivery of siRNA and DOX using the polypeptide 105
3.12. Synthetic scheme for the synthesis of the new HDAC inhibitor 107
3.13. Synthetic scheme for the synthesis of the amino acid N-carboxy anhydrides (NCAs) 108
3.14. Synthetic scheme for conjugation of DOX and HDACi to the polypeptide 110

Chapter 1

Introduction

Nanotechnology is considered to be an emerging, disruptive technology that will have significant impact in all industrial sectors and across-the-board applications in cancer research. In 1959, the promise of nanotechnology was outlined by Nobel Prize laureate Richard Feynman in his famous talk, *"There's Plenty of Room at the Bottom"*. Since then, there has been tremendous investment in this area and an explosion of research and development efforts in recent years, particularly in the area of nanomedicine and cancer research. Nano refers to nanometer which is 1 x 10^9 m. Nanotechnology is the engineering, characterization, and application of man-made structures on the scale of 1–100 nm in at least one dimension. Materials engineered on this scale have unique properties that are not seen with materials on larger scales and materials at this scale have a favorable profile for interaction with cell surface and intercellular structures. We have witnessed tremendous progress of nanotechnology over the past few decades. The recent emergence of nanotechnology, however, has set very high expectations in biological and medical sciences. This is not surprising at all, given that the sizes of functional elements in biology such as proteins and polynucleic acids are in the nanometer scale range [1]. In addition, nanomaterials have novel electronic, optical, magnetic, and structural properties that cannot be obtained from either individual molecules or bulk materials. These unique features can be precisely tuned to explore biological phenomena through numerous innovative techniques. In fact, we believe the current nanotechnology-based approaches can resolve key questions concerning biological systems by giving us the ability to investigate, probe and manipulate these systems at the nanoscale. Currently, there are over several nanotechnology-based products in the

market for applications such as drug delivery, molecular diagnostics and cancer therapy. However, in order to apply nanotechnology to investigating and solving the key questions in cancer biology and medicine, particularly in the field of drug deliivery and molecular imaging, several conditions must be considered: i) the nanomaterials used must be designed to have superior physical/chemical properties and interact with proteins and cells without interfering with their biological activities, ii) nanomaterials must maintain their physical properties after surface modification, and iii) nanomaterials must be non-toxic.

One of the important technological aspects of nanotechnology-based applications lies in the ability to tune materials in a way that their spatial and temporal scales are compatible with biomolecules. That said, materials developed at the nanometer scale can investigate and control the interactions between biomolecules and their counterparts at almost the single molecule level. This, in turn, indicates that nanomaterials and nanodevices can be fabricated to show high sensitivity, selectivity, and control properties, which usually cannot be achieved in bulk materials. The wide range of the scale of materials and biointeractions is described in Figure 1.1.

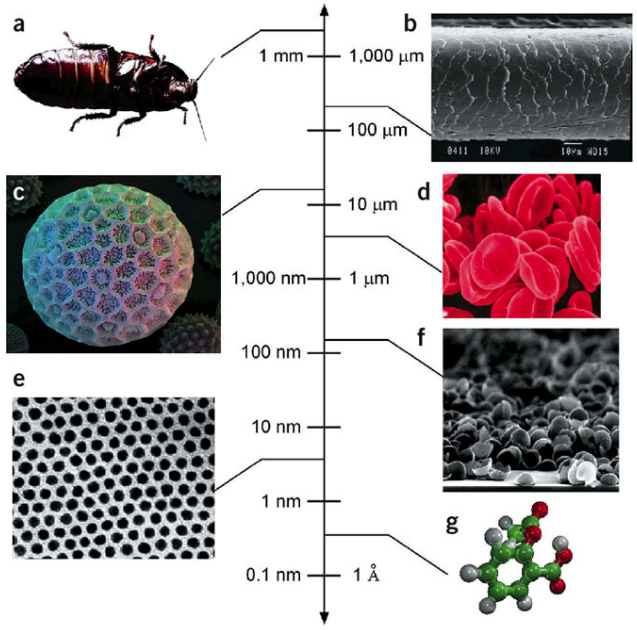

Figure 1.1: Range of scale of biomolecular interactions. a) a dust mite, b) SEM of a strand of hair, c) a virus, d) red blood cells, e) gold nanoparticles, f) side view of an SEM of clay mineral and g) small molecules.

The last decade has seen a surge in the use of nanomaterials for several biological applications such as molecular imaging, diagnostics, biosensing and most importantly for drug delivery. Even though, there are numerous studies on the use of nanomaterials for drug delivery and imaging, very few have actually reached the clinic. Successful clinical applications of nanomaterials for the treatment of cancer requires the ability to have (1) targeted delivery of drugs or biomolecules in a cell- or tissue-specific manner; (2) co-delivery of two or more drugs or therapeutic modalities for combination therapy; and (3) visualization of sites of drug delivery by combining therapeutic agents with imaging modalities; Furthermore, the nanomaterials must be non-toxic and biocompatible with favorable clearance properties.

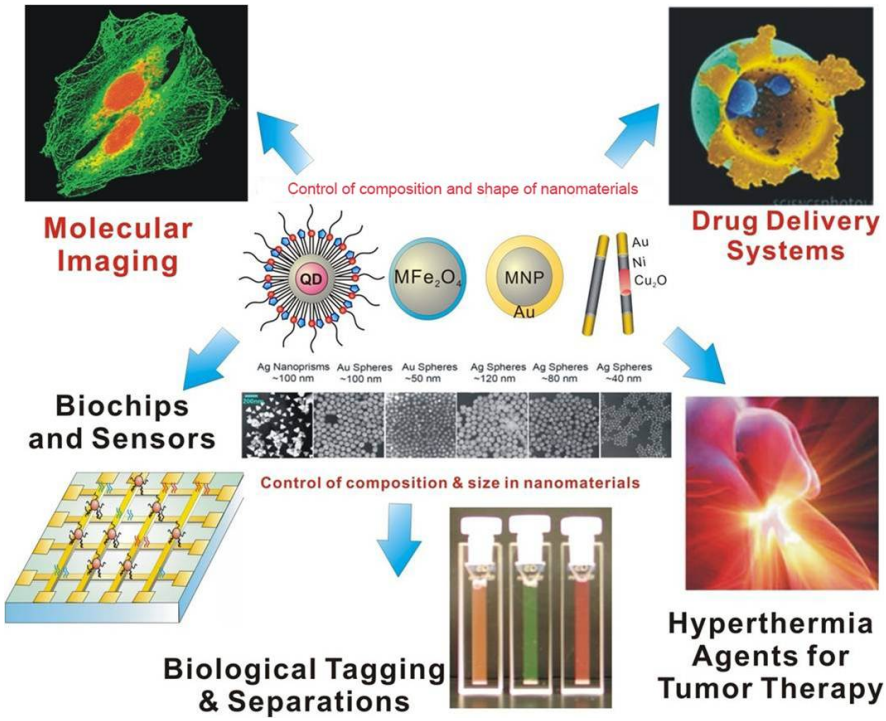

Figure 1.2: Applications of nanotechnology in biology and medicine.

Therefore, it is not surprising that the last decade has seen a significantly large proportion of chemists, materials scientists and biomedical engineers working hand-in-hand with medical experts to develop newer and better nanomaterials to address the current limitations in cancer diagnosis and therapy. Figure 1.2 summarizes some of the important applications of nanotechnology in biology and medicine. This chapter will broadly cover the applications of several novel nanomaterials in cancer biology with a focus on (i) Nanostructures as multimodal imaging and diagnostic probes, and (ii) Nanomaterials for drug delivery and effective cancer therapy.

1.1 Nanomaterial-based Molecular Imaging and Multimodal Diagnostic Agents

Since ancient times, visualization of the detailed inner spaces of the body, without surgery, was a physicians dream. Diagnostic imaging modalities are currently one of the most rapidly expanding domains in the eld of medicine, with several methods for imaging internal structures and functions of the body including X-ray, computed tomography (CT), positron emission tomography (PET), single-photon emission computed tomography (SPECT), ultrasound (US), and magnetic resonance imaging (MRI). Each method has its advantages and disadvantages according to the physical phenomena that are being employed to create imaging information. In CT, an X-ray beam is sent through an object and is differentially attenuated by the various structures of the object according to their densities. For example, in living organisms, bones impede most of the incident X-rays, while soft tissues and uids do not. X-rays blunting across the object are detected from multiple angles around the circumference of the scanner and a two–dimensional (2D) image of each slice of the object can be reconstructed by a computer. On the other hand, PET is an imaging method that uses a radioactive isotope incorporated in a metabolically active molecule, commonly Fluorodeoxyglucose (FDG). These radioactive tracers are injected into the circulating blood and decay by emitting a positron, which on annihilation by an electron results in a pair of photons moving in nearly opposite directions. These photons are then detected by a scintillator material in

the scanning device using photomultiplier tubes. SPECT also works on a similar principle, the difference being that SPECT images are collected using gamma cameras and the 2D images acquired from multiple angles are then tomographically reconstructed to obtain a three–dimensional (3D) image. Nuclear medicine imaging techniques (e.g., PET and SPECT) have the advantages of an excellent sensitivity and the possibility to create 3D images. However, the radiotracers could have dentrimental side effects. In this regard MRI has emerged to be a very safe method for human *in vivo* imaging that uses a powerful magnetic eld to align the nuclear magnetization of hydrogen atoms which are responsible for the majority of MRI signals. Hence, the water distribution in the body is shown by MRI to correlate with the anatomy of the body. MRI use the principles of nuclear magnetic resonance (NMR) for signal acquisition (i.e., interactions between nuclear spin and magnetic field). The distinguishing feature of MRI, in comparison with other available methods, is its unique potential to probe the *in vivo* molecular diffusion of water (i.e., its molecular movement along random paths).

Nanotechnology has contributed significantly to the advancement of medical imaging and thus has become recognized as a key enabler in pharmaceutical research and development. Advances in nanotechnology and their integration into imaging in analyses of cellular and tissue functions, drug discovery, and drug delivery have contributed to providing new and unique insights into the pathways and fates of drugs, nanosystems, and molecular species involved in promotion of pathological processes or functional repair. Nanoparticles (NPs), which are typically inorganic, organic and dendritic, are attractive due to several unique properties owing to their size. Size is known to have a profound effect on the properties of nanoparticles and by controlling the conditions of nanoparticle synthesis, the size and shape can be controlled within a very tight distribution [2]. Nanoparticles also have enormous surface-to-volume ratios which aids their modification with various ligands and functional groups that can help target, internalize or stabilize the NPs. While many of such properties may be described as intermediate between bulk materials and small molecules, other properties such as superparamagnetism and quantum confinement are unique to the nanoscale. These unique properties of nanoparticles make them very useful for medical imaging and diagnosis of debilitating

diseases such as cancer and neurodegenerative disorders.

The small size of these nanoparticles allows them to be easily taken up by the cell. In addition to the facile cellular uptake, they also exhibit unique pharmacokinetics, thus leading to increased bioavailaibilty and minimal renal filtration. Furthermore, the particles can interact with individual biomolecules at the molecular level. By making use of inorganic, organic, and surface chemistry techniques, biomolecules such as antibodies [3] or peptides [4] can be added to nanoparticles to include functionality for targeting, improve cellular uptake or for the conjugation of multiple imaging and therapeutic modalities. These NPs can then be used for delivery of the desired cargo into cells and most importantly, for tracking the release once uptaken by them *in vivo*. Important types of NPs used for imaging of cancer and stem cells, both *in vitro* and *in vivo*, with an overall goal of improving currently available medical imaging methologies, will be discussed.

1.1.1 Plasmonic Nanoparticles

Plasmonics refers to the study of enhanced electromagnetic properties of metallic nanostructures. The term is derived from plasmons, the quanta associated with longitudinal waves propagating in matter through the collective motion of large numbers of electrons. Metallic nanoparticles, usually made of gold or silver, show distinctive optical properties by virtue of their strong surface plamson resonance (SPR) (Figure 1.3) [5,6].

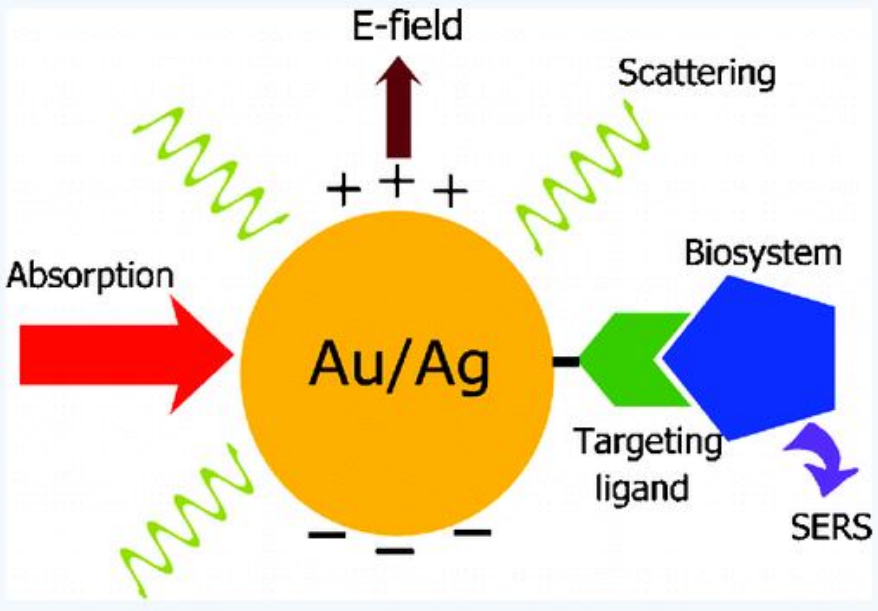

Figure 1.3: Schematic illustration of the optical properties of metallic nanoparticles for surface–enhaced Raman spectroscopy. Reprinted with permission from [5]. Copyright 2008 American Chemical Society.

The potential of metallic nanoparticles as optically active biological labels has led to the development of a variety of novel applications in medicine and biosensing with unprecedented sensitivity. [7–14] Typical scattering cross sections of metal nanoparticles greatly exceed the absorption cross-section of fluorescent dyes [15] and of fluorescent proteins [16, 17]. The photostability, water solubility and nontoxicity of gold nanoparticles make these probes advantageous for biological imaging. In addition, the facile surface chemistry and conjugation strategies to attach targeting or therapeutic moieties are well developed [18–21]. The development of gold nanoparticle-based contrast agents has given rise to new opportunities in optical imaging of cells and tissues; agents have been developed using gold-based nanoparticles with various geometries, including nanoshells [22–24], nanorods [25, 26] and nanocages [27].

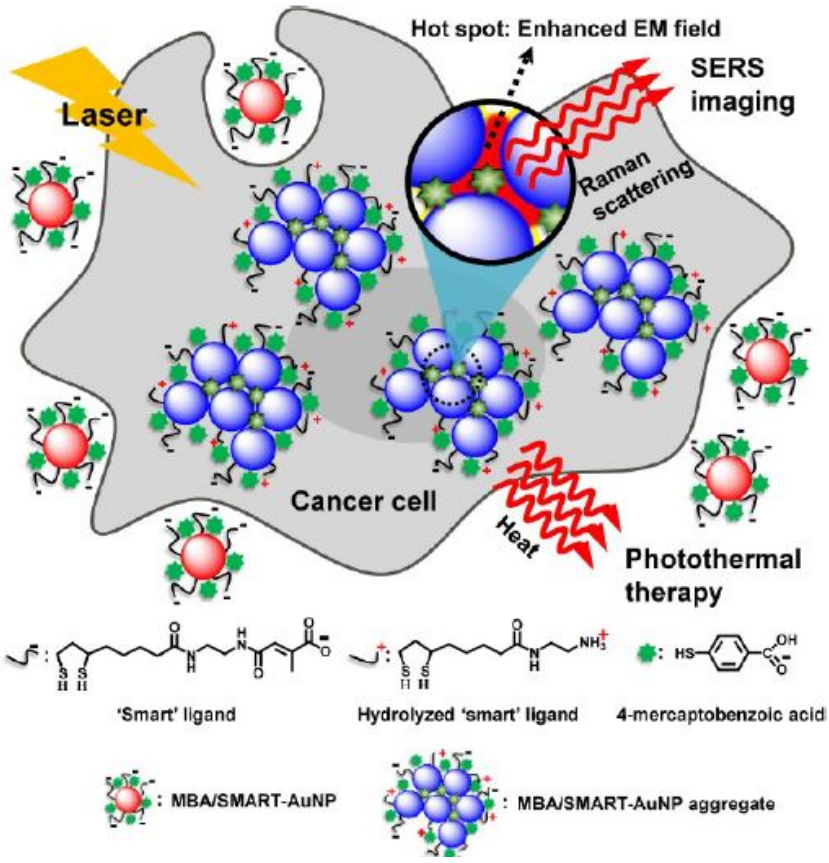

Figure 1.4: Schematic Illustration of the Working Mechanism of MBA/SMART-AuNP in a Melanoma Cell. Upon internalization by the cell, MBA/SMART-AuNPs form gold NP aggregates as the result of surface charge conversions of the NPs. The gold NP aggregates can form surface enhanced Raman scattering imaging probes at the internally created hot spots where Raman scatterings are greatly enhanced. Reprinted with permission from [28]. Copyright 2013 American Chemical Society.

Gold nanoparticles can provide optical contrast via either absorption, scattering or luminescence; the surface plasmon resonance peak of gold nanoparticles is strongly influenced by particle size, shape, material composition and interparticle spacing, and can be tuned from the visible (500–600 nm) to the NIR spectral region (700-850 nm), where tissue is the most transparent [29]. For instance, it was recently demonstrated that rapid aggregations of the gold NPs provided hot spots for a conjugated surface enhaced Raman spectral (SERS) probe with the enhancement factor reaching 1.3×10^4, thus shifting the absorption to far-red and near-infrared (which is optimal for deep tissue penetration) by the coupled plasmon resonances; this shift was successfully exploited for the successful Raman imaging of cancerous cells and also for low-threshold photothermal

therapy (Figure 1.4) [28].

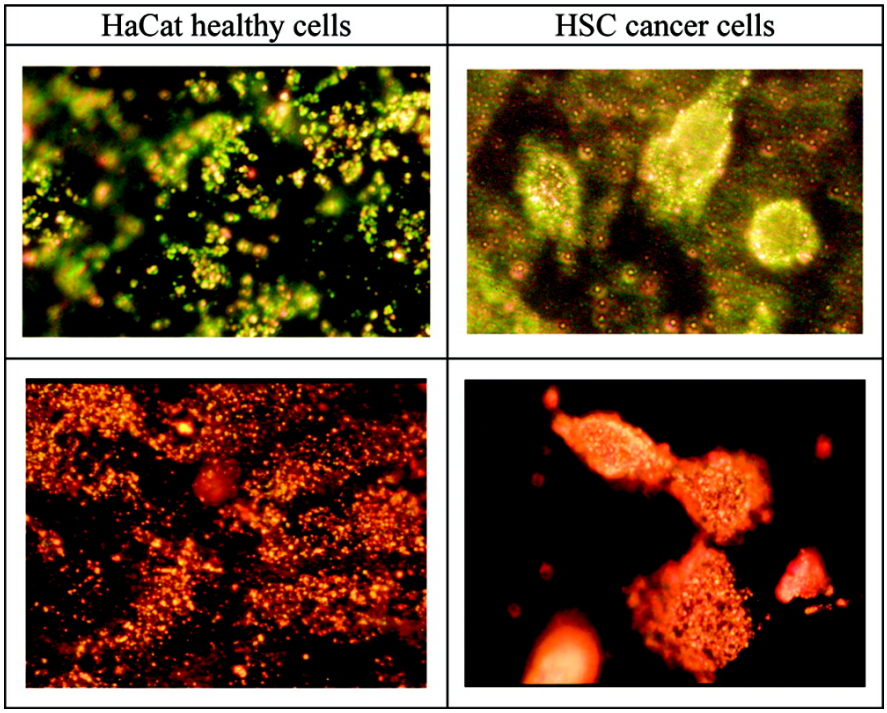

Figure 1.5: Molecular-specific imaging of cancer using gold nanoparticle/anti-EGFR conjugates. Dark-field microscopy shows (right) HSC cancer cells clearly defined by the strong LSPR scattering from (top) gold nanospheres and (bottom) gold nanorods bound specifically to the cancer cell surface, whereas (left) HaCat healthy cells have (top) gold nanospheres and (bottom) gold nanorods randomly dispersed without specific binding. The scattering color (LSPR frequency) of the nanospheres and nanorods can be clearly distinguished. Reprinted with permission from [30]. Copyright 2005 American Chemical Society.

It has also been shown that targeted gold nanoparticles can be used to provide high contrast images of cancer cells using a variety of optical modalities, including reflectance confocal microscopy [19, 29], dark-field microscopy [30], phase-sensitive optical coherence tomography [31] and photoacoustic imaging [32, 33]. For instance, El-Sayed et al used immunotargeted gold NPs for differentiating cancerous cells from non-cancerous cells using dark-field microscopy [30]. They reported that the anti-EGFR antibody–conjugated nanoparticles specifically and homogeneously bind to the surface of the cancer cells with 600% greater affinity than to the non–cancerous cells. This specific and homogeneous binding was found to give a relatively sharper SPR absorption

band with a red shifted maximum compared to that observed when added to the non–cancerous cells. These results suggest that SPR scattering imaging or SPR absorption spectroscopy generated from antibody conjugated gold nanoparticles can be useful in molecular biosensor techniques for the diagnosis and investigation of cancer cells *in vitro* and *in vivo* (Figure 1.5). The concept of plasmon coupling of gold nanoparticles has been explored extensively for molecular imaging of carcinogenesis [19, 29, 33]. A number of cancer-related targets exist as closely spaced hetero- and homodimers; the Epidermal Growth Factor Receptor (EGFR) is a prime example. Binding of the EGF ligand induces EGFR dimerization and receptor aggregation in the plasma membrane. Receptor mediated assembly of EGFR-targeted spherical gold nanoparticles on the cell membrane can result in a dramatic spectral shift of more than 100 nm [29], thereby allowing for the highly sensitive detection of labeled cells, even in the presence of single unbound gold bioconjugates.

In addition to the gold NPs, metallic nanoparticles with a dielectric core/metallic shell composition have been explored extensively as contrast agents for molecular imaging. In particular, the optical resonance of nanoshells with a silica core and thin gold coating can be tailored over a broad spectral range by simply changing the core size and the core–to–shell ratio. Optimizing nanoshells to have peak scattering in the NIR region imparts the highest imaging depth. The large optical cross-section of nanoshells is especially valuable for imaging modalities such as optical coherence tomography and confocal reflectance microscopy. Nanoshells targeted to human epiderml growth factor–2 (HER2) have been used for dark-field and reflectance confocal imaging of HER2–positive human breast carcinoma cells *in vitro* and *ex vivo* human tissue sections (Figure 1.6) [24, 34, 35].

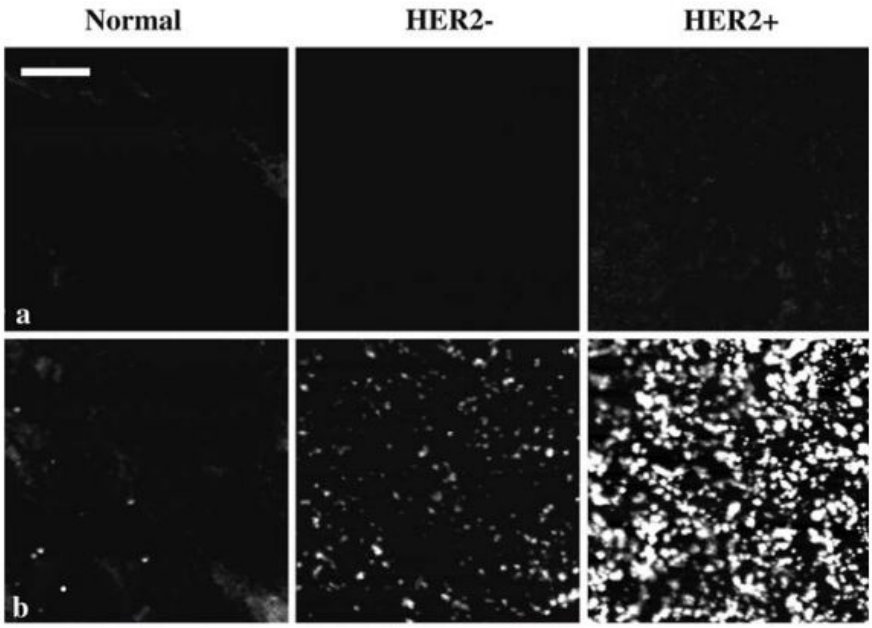

Figure 1.6: Reflectance confocal microscopy images of normal, HER2– cancerous, and HER2+ cancerous human tissue samples incubated with a PBS (a) or HER2-targeted nanoshells (b) for 5 min. Power for a and b at 0.4 mW and corresponding scale bar represents 50 μm. Reprinted with permission from [35].

Nanoshell composition can be altered to reduce particle outer diameter while retaining peak scattering in the NIR. For example, gold-gold sulfide nanoparticles (40 nm) targeted to HER2, which are smaller than silica–gold nanoshells (120-150 nm), have also been used for multiphoton imaging [36]. Multilayer, composite spherical nanoparticles have been designed to further optimize optical properties for optical imaging and therapeutic purposes. By altering the composition and thickness of three-layered nanospheres, ultra-sharp resonance peaks are possible, which could allow for multiple targets to be imaged simultaneously [21].

1.1.2 Magnetic Nanoparticles

The imaging of deep-rooted tumors such as brain cancer is an extremely challenging task. Several techniques such as magnetic resonance imaging (MRI), bioluminescence, positron emission tomography, and multiple photon microscopy are now available for *in vivo* imaging of such tumors. Of these, MRI offers several advantages such as high

resolution, speed, easy accessibility and three dimensional capabilities [37–39]. In addition to providing information about the tumor lesion, a significant advantage of MRI is that it provides information about the surrounding tissues (e.g. normal tissue, vasculature, edema or inflammation), which may give valuable information while performing tumor resections in the brain and breast. Superparamagnetic iron oxide nanoparticles (SPIONs) have garnered significant attention owing to their biodegradability and inherent contrast enhancement properties in MRI [40, 41]. Magnetic nanoparticles (MNPs), whose sizes can be precisely tuned, offer great potential for MRI applications. The magnetic nanocrystals tend to behave as a single magnetic domain in which all nuclear spins couple to create a single large magnetic domain. At certain temperatures and crystal sizes, these moments wander randomly (superparamagnetic), or become locked in one direction, making the material ferromagnetic [42]. Magnetic nanocrystals of differing compositions and sizes can be synthesized to generate ultra-sensitive molecular images as shown in Figure 1.7 [43].

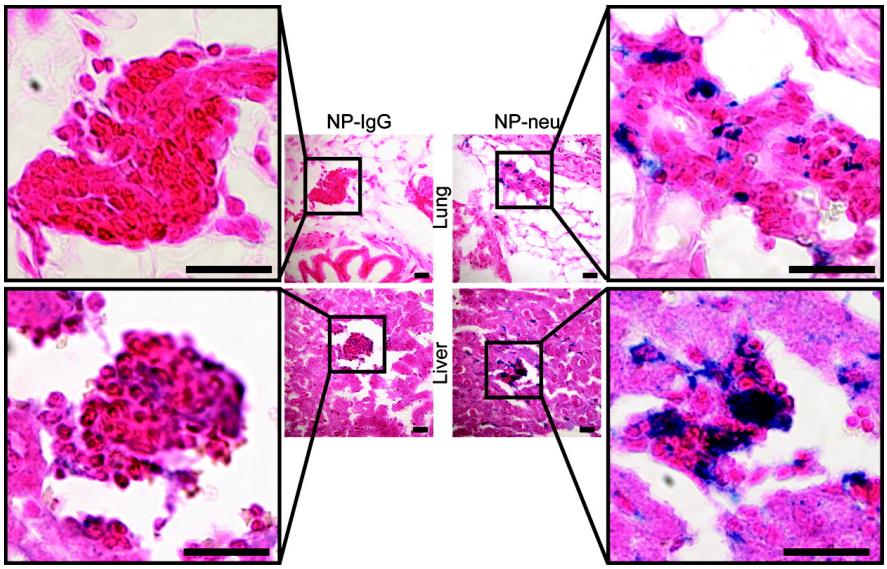

Figure 1.7: Cancer cells labeled with iron oxide nanoparticles. Prussian blue stained histology images of micrometastases in lungs and livers from NP-IgG (control) and NP-Neu (targeted) treated transgenic breast cancer mice. Scale bars correspond to 20 μm. Reprinted with permission from [43]. Copyright 2012 American Chemical Society.

Magnetic nanoparticles can either bind to the external cell membrane or be internalized into the cytoplasm. Particles that are bound externally do not affect cell viability

and can be used for remotely actuating the MNPs, which causes the activation of signaling pathways within the cells or causes the release of drugs from the MNPs Figure 1.8 [44, 45].

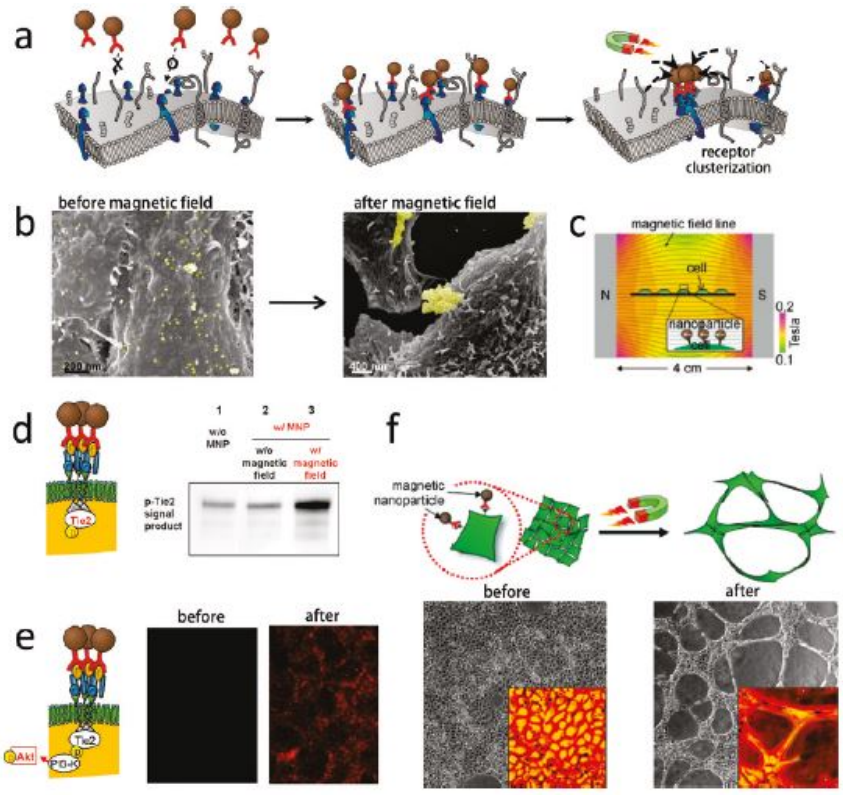

Figure 1.8: Activation of cellular signaling processes by magnetized nanoparticles. (a) Targeting and magnetic aggregation of cell surface receptors. (b) Scanning electron microscopy (SEM) image of before and after the magnetic field application. Nanoparticles are false-colored as yellow for clear visibility. (c) Magnet setup diagram for cell activations. (d) Phosphorylation of Tie2 (p-Tie2) and Western blot analysis. (e) Phosphorylation of Akt (p-Akt) and fluorescence confocal microscopy images of cell cytoplasm before and after application of a magnetic field. (f) Morphological change of HUVECs with Tie2 receptors before and after the application of magnetic field. Reprinted with permission from [44]. Copyright 2011 American Chemical Society.

On the other hand, the surfaces of MNPs can be modified to ensure that they are internalized within cells in a highly efficient manner, with minimum deleterious effects on the cells. For example, dextran or other similar polymers have been used to coat the surfaces of superparamagnetic iron oxide nanoparticles (SPIONs) to enhance the stability and solubility of SPIONs [46], prevent aggregation [47] and above all to increase their biocompatibility. The coated SPIONs are useful for imaging tumor vaculature and

also for tracking the delivery of anticancer therapeutics with MRI. For example, SPIONs coated with a copolymer of chitosan and polyethylene glycol (PEG) were labeled with a fluorescent dye for optical detection and conjugated with a monoclonal antibody against the Neu receptor (NP-Neu). SPIONs labeled with mouse IgG were used as a non–targeting control (NP-IgG). These SPIONs had desirable physiochemical properties for *in vivo* applications such as near neutral zeta potential and hydrodynamic size around 40 nm and were highly stable in serum containing medium. Only NP-Neu showed high uptake in Neu expressing mouse mammary carcinoma (MMC) cells which was reversed by competing free Neu antibody, indicating their specificity to the Neu antigen. *In vivo*, NP-Neu was able to tag primary breast tumors and further only NP-Neu was found to significantly bind to liver, lung, and bone marrow metastases in a transgenic mouse model of metastatic breast cancer, highlighting the necessity of targeting for delivery to metastatic disease. The SPIONs provided significant contrast enhancement in MR images of primary breast tumors; thus, they have the potential for MRI detection of micrometastases (Figure 1.9) and provide an excellent platform for further development of an efficient metastatic breast cancer therapy [43]

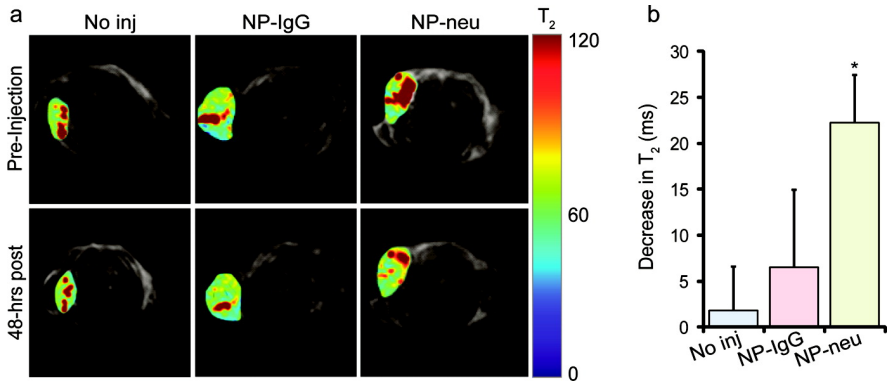

Figure 1.9: MRI of NP treated transgenic breast cancer mice. (a) Colorized T2 maps of the tumor site were overlaid onto anatomical images. Noninjected and control NP-IgG injected mice showed no significant T2 changes in their tumors 48 h postinjection. Targeted NP-Neu treated mice showed shortened T2 relaxation times in tumors 48 h postinjection, indicating that there was a significant uptake of NPs. (b) Decrease in T2 relaxation times 48 h after injection. A much larger decrease in T2 relaxation time was observed in tumors of NP-Neu treated mice (n = 3) as compared to no injection (n = 2) than NP-IgG (n = 3), suggesting a targeting role of NP-neu. $*$ indicates a statistical difference as compared to no injection. Reprinted with permission from [43]. Copyright 2012 American Chemical Society.

Integrating multiple modalities can result in a technique that enables deep tissue imaging with a traditional imaging modality to identify suspicious areas, together with a companion optical modality to interrogate these suspicious regions with higher spatial resolution to more precisely determine tumor location, monitor systemic particle distribution or to improve surgical margin planning. The use of multimodal particles to track stem cells *in vivo* exemplifies how whole-body imaging using traditional modalities (MRI) can be combined with high-resolution optical imaging to provide new capabilities that may ultimately be useful to improve diagnosis or to monitor targeted therapeutics [48]. While MRI using magnetic nanoparticles provides excellent soft-tissue contrast and multidimensional functional, structural and morphological information, it suffers from low sensitivity. Optical imaging provides high sensitivity and real-time tracking of biological processes. However it suffers from limited deep tissue penetration and background autofluorescence. SPECT and PET have high-sensitivity in tracking biological events but they have a poor spatial resolution. Therefore there is a growing interest in the use of multimodal imaging methods that combine several imaging techniques for preclinical and clinical studies. In this regard, more recent strategies have enabled the combination of traditional MRI-contrast agents together with both wide-field and high-resolution optical approaches. For instance, Xie and coworkers modified the the surface of SPIONs using fluorescent and isotope labels [49]. The magnetic nanoparticles used by the group consisted of small (15 nm) monocrystalline superparamagnetic iron oxide nanoparticle (IONPs) cores which were stabilized by coating with human serum albumin (HSA). These HSA-IONPs were labeled with Cy5.5® dye and ^{64}Cu-DOTA chelates and injected into a subcutaneous U87MG xenograft mouse model. NIRF/PET/MRI imaging and histopathology were performed to understand the particles' pharmacokinetics and to evaluate their potential role as theranostic platforms. (Figure 1.10) [50].

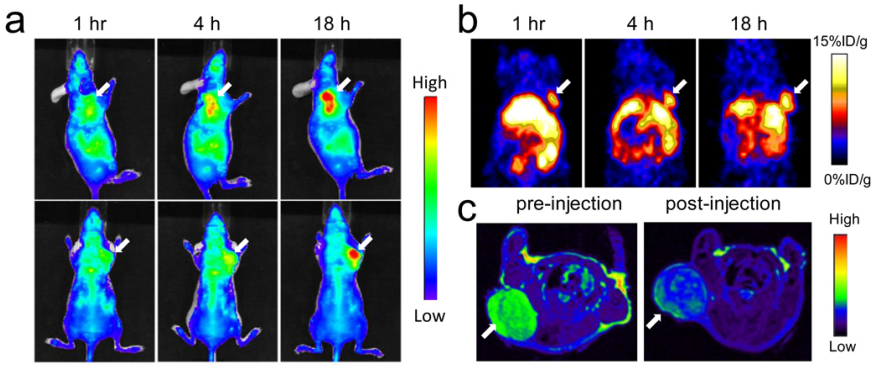

Figure 1.10: MRI/NIRF/PET trimodal imaging with MNPs that were conjugated with both ^{64}Cu–DOTA and Cy5.5. a) Representative *in vivo* NIRF images of mouse injected with HSA-IONPs. Images were acquired 1 h, 4 h and 18 h post injection. (b) In vivo PET imaging results of mouse injected with HSA-IONPs. Images were acquired 1 h, 4 h and 18 hours post injection. (c) MRI images acquired before and 18 h post injection. Reprinted with permission from [50].

Several other iron-based magnetic contrast agents such as zinc-doped iron oxide (Zn–Fe_2O_4), FePt and FeCo have also been used for multimodal imaging [51]. These nanoparticles have known to have a higher magnetization, thus, improving the MR signal in imaging, which in combination with Raman or NIR imaging, renders these nanoparticles as excellent multimodal imaging probes for cancer and other cells. For example, Dai and coworkers pioneered the use of Iron-cobalt magnetic NPs coated with a graphitic carbon shell (FeCo/GC) as a multimodal imaging probe using NIR, Raman and MR imaging techniques. They also demonstrated its use for vascular imaging *in vivo* in rabbits [52, 53].

In addition to the imaging of cancer cells, SPIONs are also being used for labeling stem cells. Considering the recent emergence of the cancer stem cell (CSC) hypotheisis [54] and the tumor tropism of mesenchymal (hMSCs) and neural stem cells (NSCs) for several types of cancer including brain cancer, the use of SPIONs for labeling and detecting transplated stem cells is of great importance in cancer diagnosis and therapy (Figure 1.11). Since their unique properties allow precise control of size and composition, MNPs offer great potential for highly specific MRI to track stem cells. The major transfer mechanism of nanoparticles through the cell membrane, in order to label stem cells, is endocytosis or more specifically pinocytosis [55–57]. For instance, Chien et al.

recently demonstrated the use of ferucarbotran and protamine (Fer-Pro) complexes for labeling human mesenchymal stem cells (hMSCs) for MRI tracking of glioma tropism *in vivo*. They found that Fer-Pro was highly efficient for labeling hMSCs *in vitro* and further that, cell labeling with Fer-Pro promoted the migration of hMSCs toward glioma U87MG cells *in vitro* [58].

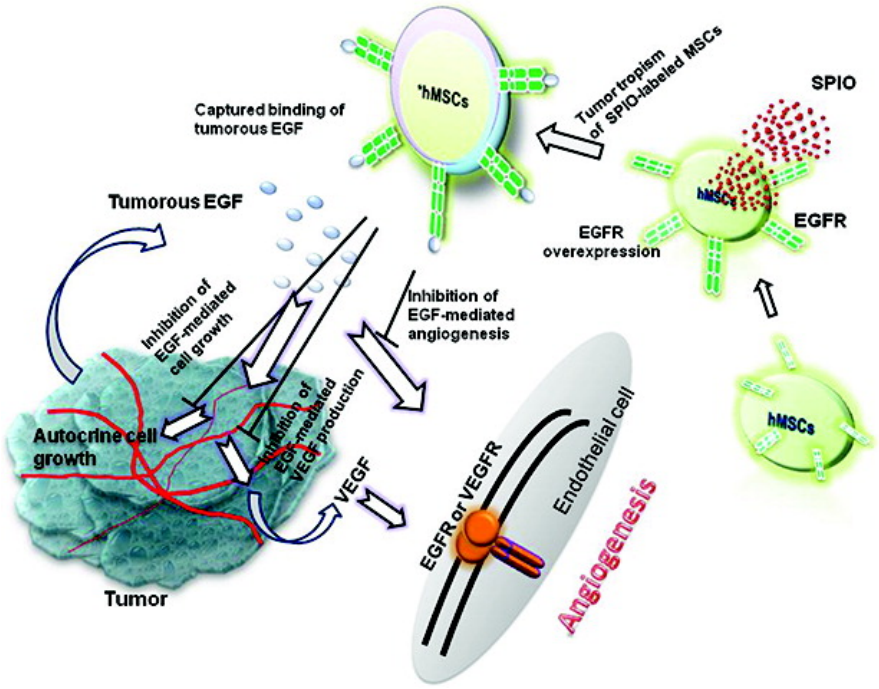

Figure 1.11: Labeling of hMSCs using magnetized nanoparticles for tumor tropism. The labeling of human mesenchymal stem cells (hMSCs) with ferucarbotran can induce epidermal growth factor receptor (EGFR) overexpression. Labeled hMSCs with their overexpressed EGFR were attracted by tumorous EGF and more effectively migrated toward tumor than unlabeled cells. Reprinted with permission from [59]. Copyright 2011 american Chemical Society.

In another study, Bulte and coworkers [60] demonstrated the potential of MRI in tracking magnetically labeled mesenchymal stem cells (MSCs) in a swine model of myocardial infarction. The mesenchymal stem cells were labeled with dextran-coated SPIONs (Feridex®) in order to noninvasively track the quantity and location of the MSCs after myocardial infarction. It was concluded that the MRI tracking of the MSCs labeled with Feridex® was feasible and represented a preferred method for studying engraftment of MSCs in myocardial infarction.

However, several studies have found that iron oxide nanoparticles, which tend to

dissolve within the cells, may increase the formation of free hydroxyl radicals and reactive oxygen species. These may have toxic effects, such as an increase in the rate of apoptosis or cell death and alterations in cellular metabolism [61], potentially due to the dissolved Fe^{2+} ions from the dissolved iron oxide nanoparticles. This is highly undesirable for labeling stem cells as they need to survive for longer periods. In order to protect stem cells from the toxic effects of SPIONs and to successfully track the behavior of stem cells *in vivo*, a very attractive alternative is to coat the SPIONs with gold. A gold coating provides an inert shell around the nanoparticles and protects them from rapid dissolution within the cytoplasmic endosomes [62]. In addition, the gold coated shell significantly enhances MRI contrast. More importantly, gold has very well defined surface chemistry with thiol (-SH) or amine ($-NH_2$) moieties. This offers an attractive and convenient route for further functionalization of the SPIONs with biomolecules via thiol or amine coupling chemistry [63]. For instance, magnetic iron oxide nanoparticles (MIONs) were coated with gold to form a typical core-shell structure [62]. These Au-MIONs, of 20 nm hydrodynamic size, were used to label NSCs obtained from the rat spinal cord. When the labeled NSCs were transplanted within the spinal cord, the Au-MION system offered a strong and durable signal such that, as little as 20 cells could be detected with relative ease under optimal conditions using MRI. In addition, the Au-MION labeling helped distinguish the labeled NSCs from the haemoglobin breakdown products *in vivo*. False positives obtained due to Prussian Blue staining of haemoglobin products in histology could be avoided by using a selective stain for gold.

Hence, we see that without a depth-penetration limit of the magnetic field in the human body, magnetic nanoparticles have been one of the ideal platform materials for targeted imaging of biological objects. Their additional capabilities are non-invasive and remote actuation for controlled drug release and cell signaling for therapeutics. These nanoparticles can also be used for targeted imaging of specific receptors and enzymes in disease processes and for the monitoring of the efficacy of the treatments. The current developmental stage of magnetic theranostic nanoparticles is still too early to predict their success, but rapid advances in new design concepts for next-generation

nanoparticles would have promising potential in that avenue.

1.1.3 Fluorescent Nanoparticles

One of the fundamental goals in biology is to understand the complex spatiotemporal interplay of biomolecules from the cellular to the integrative level. To study these interactions, researchers commonly use fluorescent labelling for both *in vivo* cellular imaging and *in vitro* assay detection. In this regard, the discovery and development of fluorescent inorganic nanoparticles called as quantum dots (QDs) has revolutionized the field of biological imaging. Quantum dots are semiconductor nanocrystals with diameters smaller than the Bohr excitation diameter (210 nm). The size-dependent optical properties are due to quantum confinement of electrons and holes. Apart from MNPs, QDs are being extensively used for applications in cell biology such as cell labeling, cell tracking, and *in vivo* imaging due to their potential in imaging and detection applications. Quantum dots overcome limitations of conventional imaging methods such as fluorescence microscopy and differential interference contrast microscopy. Quantum dots exhibit improved brightness due to their high extinction coefficients that are an order of magnitude higher than most fluorescent dyes. In addition, these particles have improved photostability compared with organic fluorophores, and their broad excitation bands and narrow emission spectra facilitate the simultaneous labeling of multiple biomarkers. For instance, multiple QDs with different emission wavelengths have been used in parallel for multiplex imaging of cancer and other mammlian cells [64–67]. (Figure 1.12) [68].

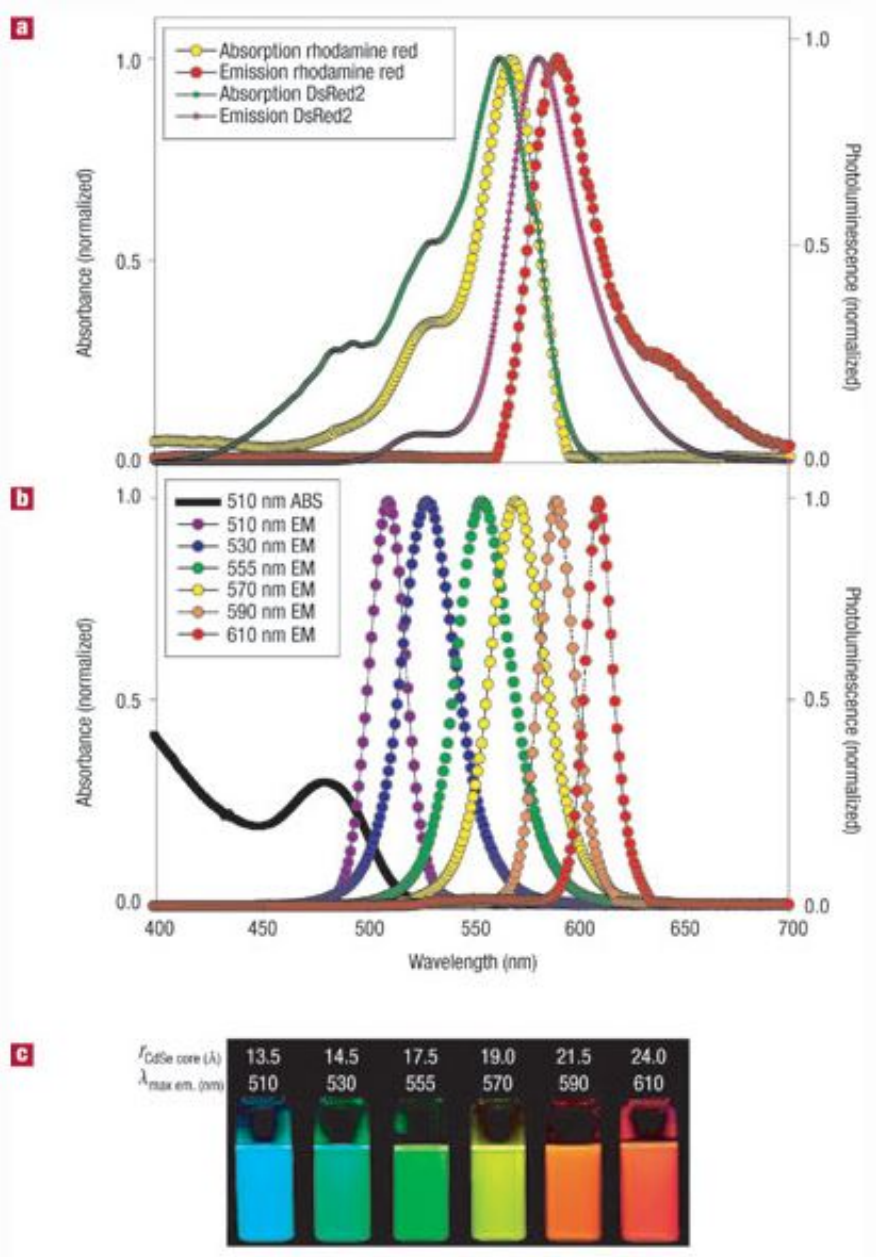

Figure 1.12: Excitation and emission spectra of CdSe quantum dots. a) Absorption (Abs) and emission (Em) of rhodamine red, a common organic dye and genetically encoded DsRed2 protein. b) Absorption and emission of six different QD dispersions. The black line shows the absorption of the 510-nm-emitting QDs. c) Photo demonstrating the size-tunable fluorescence properties and spectral range of the six QD dispersions plotted in b versus CdSe core size. All samples were excited at 365 nm with a UV source. For the 610-nm-emitting QDs, this translates into a Stokes shift of ∼250 nm. r = radius. Reprinted with permission from [69].

The interesting optical properties of QDs originate from the interactions between

electrons, holes, and their local environments, which can be precisely controlled to generate desired emission and absorption spectra. Since absorption and emission spectra exhibit sensitive changes depending on particle size, a wide range of emission spectra from ultraviolet (UV) to infrared (IR) can be obtained. Therefore, unique emission spectra by synthesizing particles with different diameters have been acquired [70–72]. In addition, the need for an external excitation source may be eliminated with particular quantum dots. Quantum dots generally have a core composed of heavy metals, such as Cadmium-Selenide (CdSe) and Cadmium-Telluride (CdTe), with a surrounding ZnS shell. The thickness of the shell can be tuned depending on the reaction time. Typically, the core/shell QDs with sizes ranging from 2-8 nm in diameter are synthesized by changing reaction conditions such as temperature, duration, and ligands. In addition to the CdSe/ZnS Qds, a new generation of QDs have recently become popular as their emission properties depend on the materials from which they are synthesized and not on their sizes. These are the ternary I-III-VI_2 type QDs [73–78] like $AgInS_2$ [75], $CuInS_2$ [74, 76] and ZnS-$AgInS_2$ [77], which offer better control of band-gap energies and demonstrate great potential as non-toxic molecular probes. Considering the toxicity of the heavy metals such as cadmium and selenide, the non-toxic ZAIS QDs seem to be an attractive choice for cellular delivery and molecular imaging.

The distinctive photophysical properties of QDs, coupled with their diverse biological applications make them very attractive probes for the imaging and diagnosis of cancer. Since the introduction of biocompatible QDs for imaging of cancer cells in 1998 [79,80], researchers have synthesized QD-based probes conjugated with cancer specific ligands, antibodies, or peptides for cancer imaging and diagnosis *in vitro* [81–88]. Compared with traditional immunohistochemistry (IHC), QD-IHC is more accurate and precise at low protein expression levels and can achieve quantitative detection which will provide much more information for personalized treatment. For instance, Xing and coworkers demonstated the use of boconjugated QDs for multiplexed and quantitative immunohistochemistry in tissue samples (Figure 1.13).

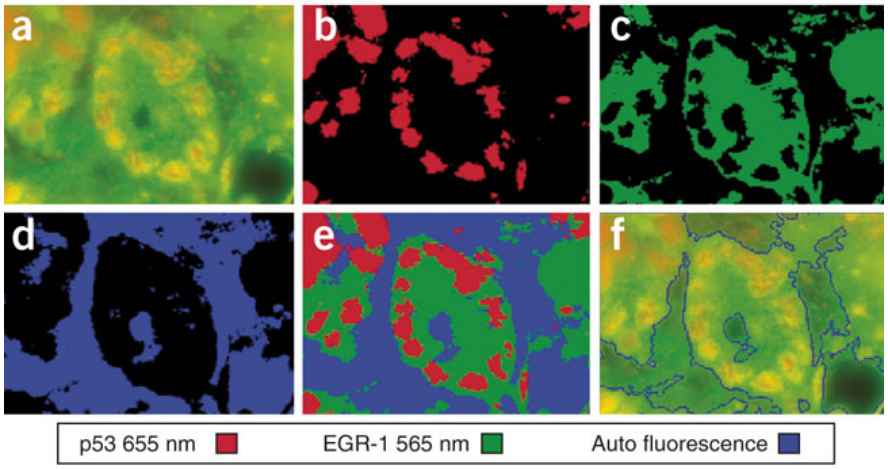

Figure 1.13: Multiplexed QD–IHC images of clinical prostate tissue specimens and quantitative analysis of cancer biomarkers. The fluorescence images were obtained with UV excitation, with the p53 marker stained red with QD655, the EGR-1 marker stained green with QD565, and the tissue background observed as blue. The color maps show the location where a biomarker (or the tissue background) is more pronounced than others. (a) Original multicolor image; (b) p53 protein (red); (c) EGR-1 protein (green); (d) tissue background fluorescence (blue); (e) combined map of dominant markers and background; and (f) automated boundary segmentation using level-set algorithms. Reprinted with permission from [89].

The results demonstrate that bioconjugated QDs can be used for multiplexed profiling of molecular biomarkers, and ultimately for correlation with disease progression and response to therapy. In another study, Chen et al [90] successfully detected breast cancer (BC) with QD-based probes which demonstrated that lower expression of HER2 could be clearly detected by QD-IHC compared with conventional IHC (Figure 1.14) and could also realize multiplexed QD-based detection simultaneously [91]. The results showed that BC can be divided into 5 subtypes with different 5-year survival rate. Thus, QD-based multiplexed imaging will provide more information about the individual events of tumor progression, personalized diagnosis, prognosis, and treatment. With excellent performance on biomedical imaging, QD-based imaging has become one of the most promising technologies for early diagnosis of cancer [92, 93].

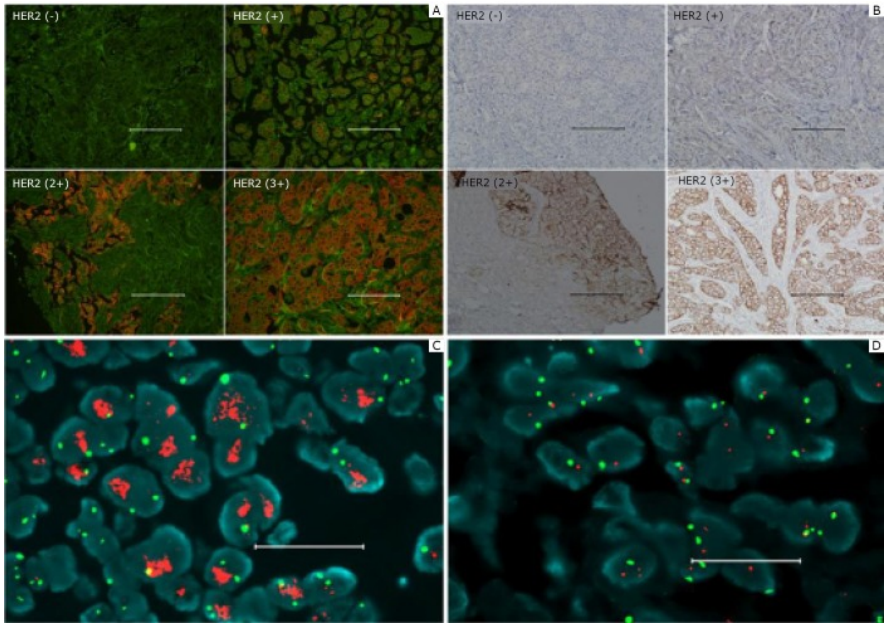

Figure 1.14: Accurate HER2 testing by QDs–IHC. (A) Specimens with different HER2–IHC scores detected by QDs–IHC. (B) Control for (A) by μm for (A) and (B) 20 μm for (C) and (D). Reprinted with permission from [90].

QDs have also been extensively used for *in vivo* imaging of tumors such as brain and breast tumor. For instance, Cai et al used peptide-labeled Near-Infrared CdTe QDs for imaging the brain tumor vasculature in mice [88]. Arginine-glycine-aspartic acid (RGD) peptide-conjugated QDs have been used to target integrin $\alpha_v\beta_3$, as it is significantly upregulated in tumors, but not in normal tissues. They found that the RGD peptide-conjugated CdTe QDs were found in the tumor within 6 hous post-injection, with a steady increase in the tumor fluorescence intensity over several hours (Figure 1.15). In a similar study, anti–HER2–CdSe/ZnS QDs were injected intravenously into nude mice bearing HER2–overexpressing MCF–7/HER2 xenografts implanted s.c. in the flank. Twenty-four hours following injection, fluorescence signals were readily detected at the tumor site, thus demonstrating that the QDs selectively and efficiently internalize in HER2-overexpressing tumor cells via receptor-mediated endocytosis. (Figure 1.16).

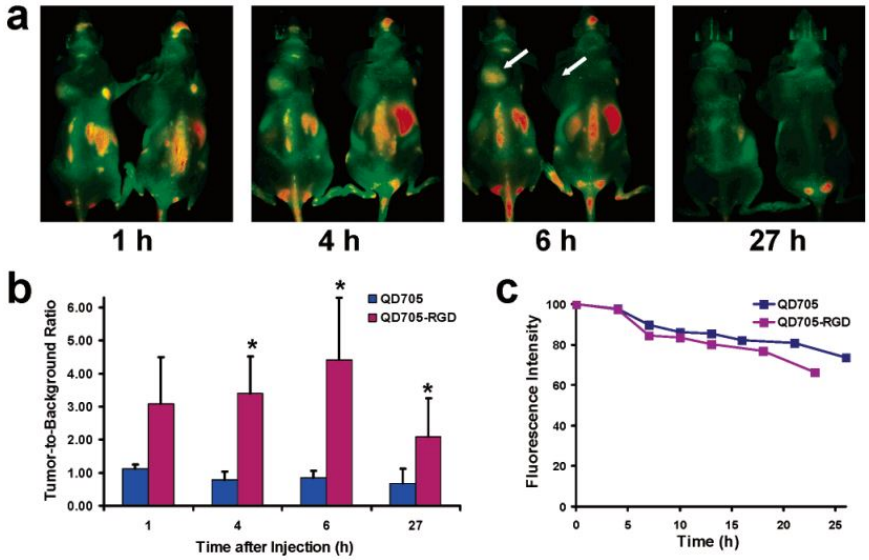

Figure 1.15: *In vivo* NIR fluorescence imaging of U87MG tumor–bearing mice (left shoulder, pointed by white arrows) injected with 200 pmol of QD705-RGD (left) and QD705 (right), respectively. All images were acquired under the same instrumental conditions. The mice autofluorescence is color coded green while the unmixed QD signal is color coded red. Prominent uptake in the liver, bone marrow, and lymph nodes was also visible. (b) Tumor-to-background ratios of mice injected with QD705 or QD705-RGD. The data were represented as mean ± standard deviation (SD). (c) Serum stability of QD705 and QD705-RGD in complete mouse serum over the course of 24 h. Reprinted with permission from [88]. Copyright 2006 American Chemical Society.

In addition to the labeling of and tracking of cancer cells, QDs are also beneficial for studying dynamic changes occurring in membranes of stem cells [94–97]. Functionalized QDs selectively bind to individual molecules on the cell surface and help in tracking the motion of those individual molecules. In a study by Chen et al. [98], functionalized QDs were used to demonstrate changes in the integrin dynamics during osteogenic differentiation of human bone marrow derived progenitor cells. In this study, quantum dots conjugated with integrin antibodies enabled precise optical identification of integrin molecules, which led to a detailed examination of the molecular dynamics of integrin molecules involved in osteogenic differentiation of the progenitor cells [98].

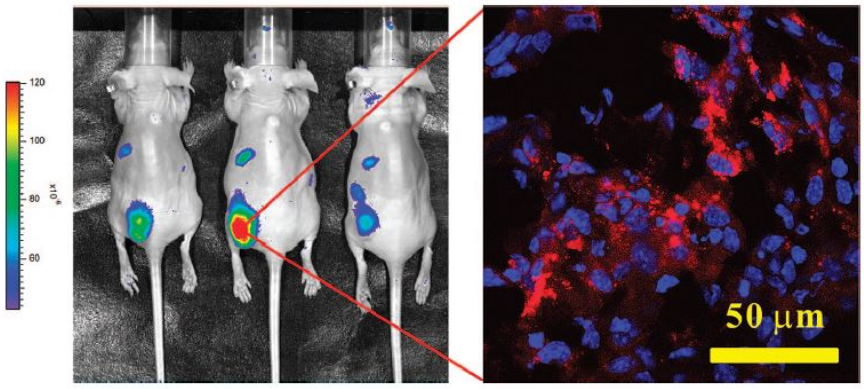

Figure 1.16: *In vivo* fluorescence imaging of three nude mice bearing MCF–7/HER2 xenografts implanted in the lower back 30 h after i.v. injection with anti-HER2 QD-ILs (Left panel). Imaging showed that QD–ILs had localized prominently in tumors as well as in MPS organs. (Right panel) A 5 μm section cut from frozen tumor tissues harvested at 48 h postinjection and examined by confocal microscopy. The tumor section was examined in two-color scanning mode for nuclei stained by DAPI (blue) and QD-ILs (red). Reprinted with permission from [99]. Copyright 2008 American Chemical Society.

In stem cell-based therapy, it is extremely important to monitor the survival and location of stem cells after they are transplanted to the desired location. Transplanted stem cells, which may be either embryonic or adult stem cells, are expected to remodel and differentiate in response to surrounding microenvironments, resulting in tissue regeneration and repair [100]. Mesenchymal stem cells labeled with bright, photostable QDs were shown to couple functionally with cardiomyocytes in co-culture, thus demonstrating the usefulness of QDs as labeling agents in culture (Figure 1.17) [101]. Human mesenchymal stem cells were labeled with QDs bioconjugated with RGD (arginine-glycine-aspartic acid) peptide during self-replication and multilineage differentiations into chondrogenic, androgenic, and adipogenic cells in a long–term labeling study. Human MSCs labeled with QDs remained viable as the unlabeled hMSCs from the same subpopulation, thus suggesting the use of QDs are useful probes from long term labeling of stem cells [102].

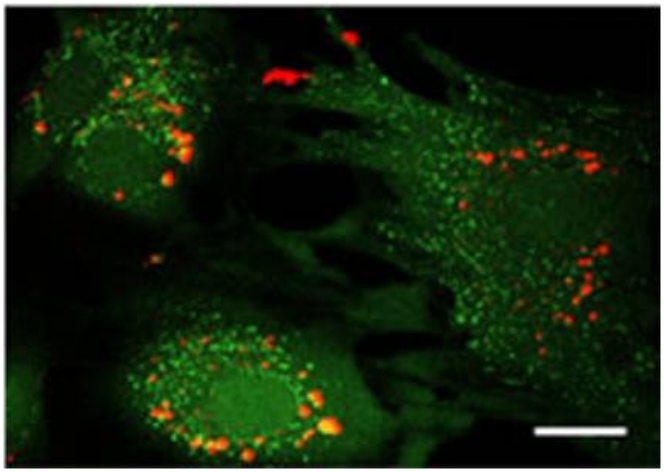

Figure 1.17: Mesenchymal stem cells (MSCs) labeled with QDs and co-labeled with calcein (green). The QDs were seen distributed within the perinuclear region within the MSCs. The QDs remained bright and were easy to detect even as the MSCs proliferated [101].

Quantum dots have also been shown to elucidate the mechanisms involved in mechanical integration of stem cells to the surrounding tissues and their differentiation into specific cell lineages *in vivo* [95]. In addition, multiplex imaging (i.e. tracking different cell populations labeled with QDs which exhibit different emission wavelengths at the same time) is one of the biggest advantages of using quantum dots for tracking stem cells *in vivo*. Wu and coworkers [68] successfully demonstrated *in vivo* multiplex imaging of mouse ESCs labeled with QDs. They subcutaneously injected ESCs labeled with six different QDs, having diverse emission wavelengths 525, 565, 605, 655, 705, and 800, into various locations on the back of athymic nude mice and detected the labeled cells *in vivo* using a single excitation wavelength (425 nm) as shown in Figure 1.18. They also concluded that within the sensitivities of the screening assays, the QDs did not affect the viability, proliferation, and differentiation capacity of the ESCs [68].

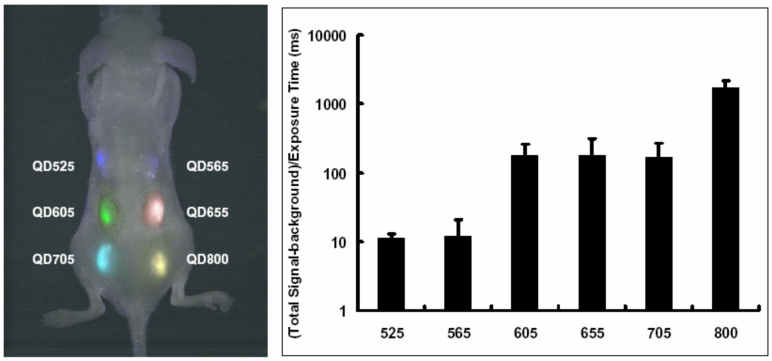

Figure 1.18: Multiplex imaging of embryonic stem cells (ESCs) labeled with QDs. (A) ESCs labeled with QD 525, 565, 605, 655, 705, and 800 were injected subcutaneously in back of athymic nude mice right after labeling, and imaged right after injection using a single excitation wavelength. (B) Quantified fluorescent signal intensity of QDs [68].

Despite having unique optical properties and a host of advantages over the conventional tracking agents, toxicity is a primary concern for the application of QDs in biology. Stem cells tend to be extremely sensitive, and thus toxicity is a primary determinant in deciding whether QDs would be feasible for stem cell tracking, especially *in vivo*. Some literature studies do suggest that QDs are nontoxic; nevertheless, recent data shows that cytotoxicity is dependent upon the physicochemical properties, dose and exposure concentrations [103]. Although the mechanism of cytotoxicity is not yet clearly known and is under thorough investigation, concerns about toxicity of QDs have been raised as they are used for cell tracking studies in live animals. Quantum dots contain heavy metals such as cadmium and selenium, and the cytotoxicity is observed due to the presence of Cd^{2+} and Se^{2-} ions [104, 105]. Toxicity can be considerably reduced by coating the core made of CdSe with a shell of a material such as ZnS, which significantly reduces toxicity by blocking the oxidation of CdSe by air [69]. Although the toxicity may not be critical at the low concentrations optimized for labeling, it could be detrimental for the embryo development at higher concentrations. Nevertheless, the problem could be solved by coating the QDs and making them biologically inert [69]. Larger molecules such as proteins (e.g. Streptavidin, bovine serum albumin) further slow down the photooxidation of the core [106]. Bioconjugation of QDs with biomolecules such as RGD did not show any toxic effect on hMSCs as compared to unlabeled hMSCs [102]. In a dose-dependent study involving the labeling of MSCs with

QDs, it was observed that if the exposure of QDs to MSCs was optimized and limited to low concentrations then the QDs were not significantly toxic [101]. Addressing the cytotoxicity issues concerning the application of QDs synthesized from heavy metals, Subramaniam at. al used ZAIS QDs to deliver siRNA into MSCs and GFP-labeled brain tumor cells [107]. The ZAIS QDs were found to be non-toxic towards both the cells and provided excellent imaging capabilities.

1.2 Nanomaterials for Drug Delivery and Effective Cancer Therapy

One of the most active research areas of nanotechnology is nanomedicine, which applies nanotechnology to highly specific medical interventions for the prevention, diagnosis and treatment of diseases. The surge in nanomedicine research during the past few decades is now translating into considerable commercialization efforts around the globe, with many products on the market and a growing number in the pipeline. Currently, nanomedicine is dominated by drug delivery systems, accounting for more than 75% of total sales. Nanomaterials fall into a size range similar to proteins and other macromolecular structures found inside living cells. As such, nanomaterials are poised to take advantage of existing cellular machinery to facilitate the delivery of drugs.

Nanoparticles (NPs) containing encapsulated, dispersed, absorbed or conjugated drugs have unique characteristics that can lead to enhanced performance in a variety of dosage forms. When formulated correctly, drug particles are resistant to settling and can have higher saturation solubility, rapid dissolution and enhanced adhesion to biological surfaces, thereby providing rapid onset of therapeutic action and improved bioavailability. In addition, the vast majority of molecules in a nanostructure reside at the particle surface, which maximizes the loading and delivery of cargos, such as therapeutic drugs, proteins and polynucleotides, to targeted cells and tissues. Highly efficient drug delivery, based on nanomaterials, can lower the cost and/or reduce the side effects associated with particular drugs. In additon, several nanoparticles, owing to their unique optical and magnetic properties, have been utilized as therapeutic agents themselves in the the form of hyperthermia or photothermal therapy, to elicit a synergistic respnse. Nanoparticle technologies for cancer therapy include polymeric nanoparticles [108], vesicle-based carriers such as liposomes [109,110], dendrimers [111,112], inorganic nanoparticles [113] and bacterial nanocarriers (Figure 1.19). A few of these NPs used for the delivery of therapeutic cargo and for multimodal cancer therapy, both *in vitro* and *in vivo*, with an overall goal of improving currently available cancer treatment methologies, will be discussed.

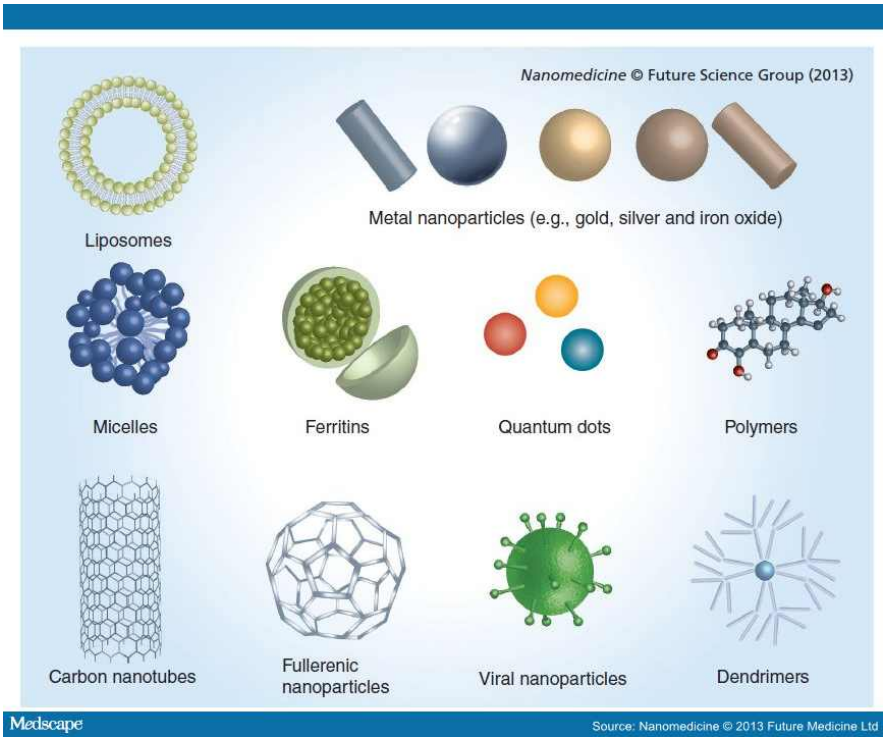

Figure 1.19: Nanomaterials for drug delivery and cancer therapy. [114]

1.2.1 Inorganic Nanomaterials

Magnetic Nanoparticles

Magnetic NPs have attracted a great deal of interest in biomedical research and clinical applications over the past decades specially for targeted drug delivery combined with magnetic resonance imaging (MRI) for non-invasive, early cancer detection, and treatment (Figure 1.20). Surface properties, specifically designed for cell targeting are required for this purpose. The general strategy involves creating a biocompatible polymeric or nonpolymeric coating and subsequently conjugating bioactive molecules to it. We have already seen the imaging and targeting caabilities of SPIONs in the previous section. Since SPIONs only exhibit magnetic properties in the presence of an applied magnetic field, they have the advantage of being used in both *in vitro* as well as in vivo applications such as hyperthermia [115], magnetic drug targeting (MDT), magnetic resonance imaging (MRI), gene delivery and wide range of applications in the detection, diagnosis, and treatment of cancer. SPIONs have shown clinical efficacy in cancer drug

delivery and imaging. Some formulations are now FDA-approved for use in the clinic.

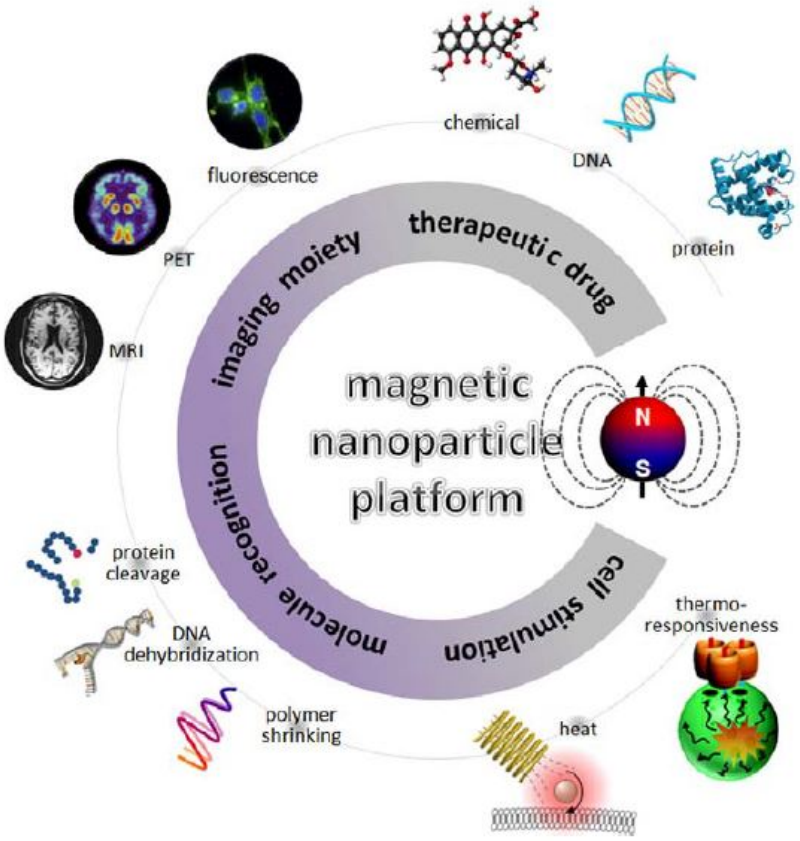

Figure 1.20: Applications of magnetic nanoparticles in drug delivery and biomedical research.

When loaded with a therapeutic payload, NPs that are appropriately designed, can act as efficient drug delivery systems, offering limited non-specific cell interactions, controlled therapeutic release, flexible drug loading (a variety of drugs can be loaded), and delivery tracking using an NP imaging modality. Like NPs developed for diagnostic imaging, drug-carrying NPs require careful physicochemical and targeting design, but also require additional considerations paid to drug loading, transport, and release [116–118]. First, the NP must be able to carry and protect a significant drug payload, typically determined by the type of coating and method of loading (e.g. covalent bonding). Second, multiple drugs can be loaded to overcome cellular drug resistance, and improve overall cell kill efficiencies, but requires careful NP planning to accommodate the different therapeutics. Third, the release mechanism and rate

of the therapeutic cargo unloading should be modulated for optimal therapeutic efficiency. Currently, several chemical drug formulations have been combined with MNPs, including paclitaxel, doxorubicin, and methotrexate (MTX), all specifically developed for cancer therapy [5, 119–121]. To successfully integrate a drug into a NP system, several design strategies can be explored, including physical complexation with hydrophobic drugs [120, 122–124], or covalent bonding with cleavable linkages for intracellular release [119]. Drugs loaded through hydrophobic interactions are typically encapsulated within the NP coating, limiting non-specific cell interactions. This approach is advantageous in applications where a drug being delivered could seriously harm non-targeted tissue. Alternatively, in applications where the drug, such as MTX has an affinity for the target cell, it can be advantageous to graft the drug to the surface of the NP [119, 125, 126]. For instance, Kohler et al. demonstrated that SPIONs can potentially serve both as a contrast enhancement agent in magnetic resonance imaging (MRI) and as a drug carrier in controlled drug delivery, targeted at cancer diagnostics and therapeutics.

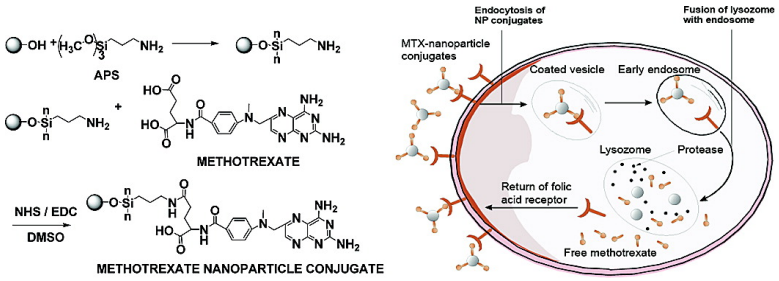

Figure 1.21: MTX-modified SPIONs for the targeted delivery into breast cancer cells. Reprinted with permission from [126]. Copyright 2005 American Chemical Society.

In their study, the conjugate was made of iron oxide nanoparticles covalently bound with methotrexate (MTX), a chemotherapeutic drug that can target many cancer cells whose surfaces are overexpressed by folate receptors. The nanoparticles were first surface-modified with (3-aminopropyl)trimethoxysilane to form a self-assembled monolayer and subsequently conjugated with MTX through amidation between the carboxylic acid end groups on MTX and the amine groups on the particle surface. Drug release experiments demonstrated that MTX was cleaved from the nanoparticles under

low pH conditions mimicking the intracellular conditions in the lysosome. Cellular viability studies in human breast cancer cells (MCF–7) and human cervical cancer cells (HeLa) further demonstrated the effectiveness of such chemical cleavage of MTX inside the target cells through the action of intracellular enzymes (Figure 1.21). Recently, Sun et al further modified the same SPION system with a peptide, namely chlorotoxin (CTX) to enhance the NP's targeting abilities against brain tumor cells [125].

In another study, Yang and colleagues [127] developed a new multifunctional hybrid nanosystem by combining magnetic nanocrystals, anticancer drugs and biodegradable amphiphilic block copolymers (Figure 1.22). In this study, there were about 41.7 wt% ($MnFe_2O_4$) and 40.9 wt% (Fe_3O_4) magnetic nanoparticles in the multifunctional magneto-polymeric nanohybrids (MMPNs), and the amount of Doxorubicin in the HER–MMPNs and entrapment efficiency were 3.3 wt% and 71.4%, respectively. In addition, anti–HER antibody was conjugated to the MMPNs by utilizing the carboxyl group on the surface of the particles. The injected HER–MMPNs were delivered in a target-specific manner to overexpressed HER2/neu receptors on NIH3T6.7 cells *in vivo* and were taken up by a receptor-mediated endocytosis process . The HER–conjugated MMPNs showed signifi cant synergistic effects on inhibition of tumor growth by DOXO. The antibody–conjugated nanoparticles also demonstrated ultrasensitive targeted detection by MRI in both *in vitro* and *in vivo* models.

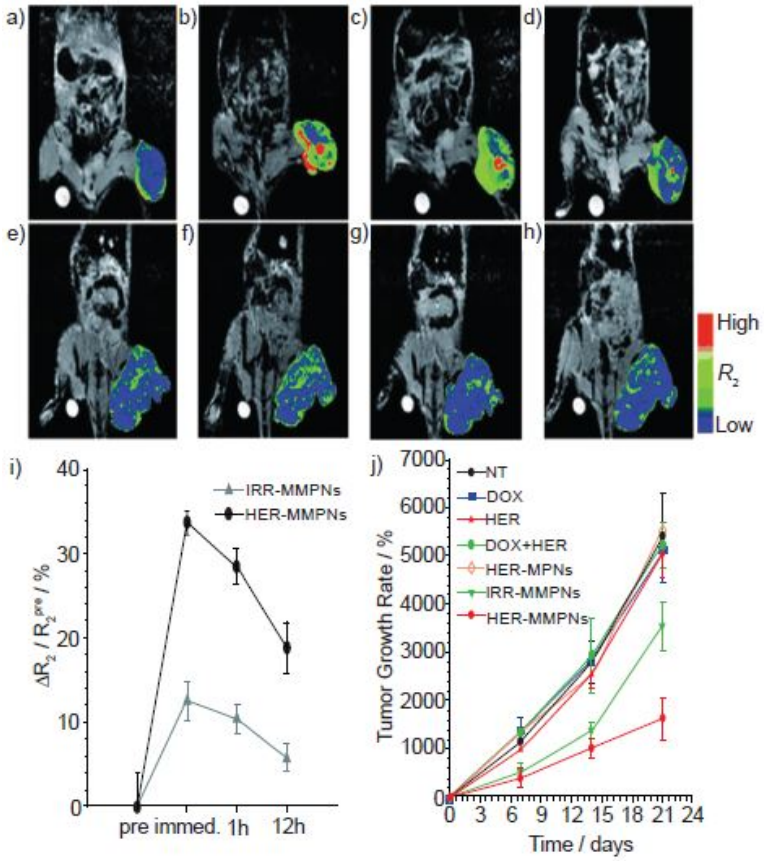

Figure 1.22: Multifunctional magneto-polymeric nanohybrids for targeted detection and synergistic therapeutic effects on breast cancer. MR images and their color maps (tumor region) of cancer-targeting events of HER-MMPNs (a-d) and IRR–MMPNs (e-h) in NIH3T6.7 cells implanted in mice at various time intervals: a,e)preinjection; b,f)immediately; c,g)1h; d,h)12h after injection of the MMPNs. i)ΔR2/R2^{pre} graph versus time before and after injection of MMPNs. j)Comparative therapeutic-efficacy study in an invivo model. Reprinted with permission from [127].

MNPs have also been explored for the delivery of small interfering RNA. RNA interference (RNAi) or gene therapy is a technique that uses DNA or oligonucleotides to treat and prevent disease. siRNA is one of the strong candidates for the next generation of gene therapy. siRNA binds mRNA to inhibit the translation processes of proteins in the cytoplasm [128]. Figure 1.23a shows a scheme for multifunctional magnetic nanoparticles for imaging and gene therapy. $MnFe_2O_4$ magnetic nanoparticles are conjugated with siRNA, fluorescence dye, surface stabilizing agent (polyethylene glycol,

PEG), and targeting Arg–Gly–Asp (RGD) peptide. RGD peptide targets $\alpha_v\beta_3$ integrin, which is overexpressed in certain endothelial and cancer cells. siRNA is bonded to nanoparticles via disulfide linkage which can be cleaved enzymatically for its facile release [129].

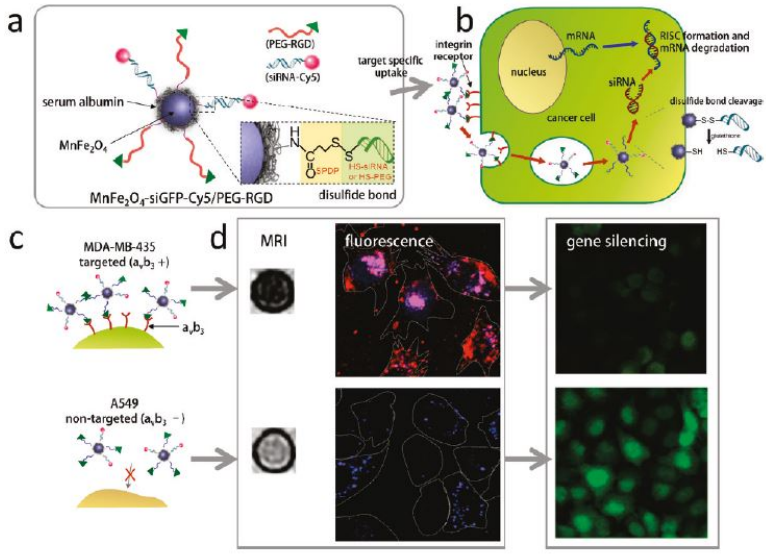

Figure 1.23: a) Schematic drawing of all-in-one nanoparticles of $MnFe_2O_4$–siGFP–Cy5/PEG–RGD for theranostics. (b) Schematic illustration of intracellular processes of $MnFe_2O_4$–siGFP–Cy5/PEG–RGD nanoparticles, from target-specific uptake to mRNA degradation. (c) Schematic illustration of the target specific binding of the nanoparticles to $\alpha_v\beta_3$ integrin positive cells. (d) T2-weighted MR images of MDA-MB-435 and A549 cells treated with MnFe2O4–siGFP–Cy5–PEG–RGD. Confocal microscopy images showing the distribution of $MnFe_2O_4$–siGFP–Cy5/PEG–RGD nanoparticles in cells. Gene-silencing effect of the multimodal nanoparticle systems with ($MnFe_2O_4$–siGFP–Cy5/PEG–RGD) and without a targeting moiety ($MnFe_2O_4$–siGFP–Cy5/PEG) on $\alpha_v\beta_3$ integrin positive (MDA-MB-435) and $\alpha_v\beta_3$ integrin negative (A549) cell lines. Reprinted with permission from [129].

The steps involved, starting from the target specific uptake of nanoparticles into the cells, to siRNA release are shown in Figure 1.23b, in which nanoparticles recognize the cancer cells via targeting RGD peptide, and after the endocytosed nanoparticles escape from the endosome, glutathione breaks the disulfide bond to release the siRNA for the inhibition of protein expression. The location of the therapeutic nanoparticles was monitored via MRI and fluorescence techniques (Figure 1.23d). The selective targeting

and theranostic effect of magnetic nanoparticles on $\alpha_v\beta_3$ receptor–expressing MDA-MB-435 human breast cancer cell lines are clearly shown with strong MRI signals and red fluorescence, and the gene silencing effect is apparent. In contrast, the control cell lines of receptor–free A549 do not show any such features. Red fluorescence in Figure 1.23d indicates that nanoparticles successfully escape the endosome. Therapeutic efficacy is clearly observed from the suppression of GFP by the released siRNA for MDA-MB-435cells, whereas bright green fluorescence is observed in the control cell line of A549 cells. As an alternative to the cationic coatings on the MNPs for complexation of siRNA, Medarova et al presented the covalent bonding of antisense RNA to CLIO NPs, while a cell penetrating peptide was used to facilitate transfection. This strategy proved to be highly successful for the delivery of therapeutic siRNAs to human colorectal carcinoma tumors *in vivo*, and represents the first targeted/siRNA–MNP used for therapeutic application [130].

The most attractive property of MNPs is their ability to emit heat when placed in an alterting magnetic field. This process of heating of the cancer tissues to temperatures above 40°C using magnetic nanoparticles, termed as hyperthermia, has been extensively exploited for multimodal and synergistic cancer therapy. Thus MNPs have been used for hyperthermia–based controlled drug release or in conjunction with siRNA-based treatment to enhance the downstream effects on cancer cell death (Figure 1.24).

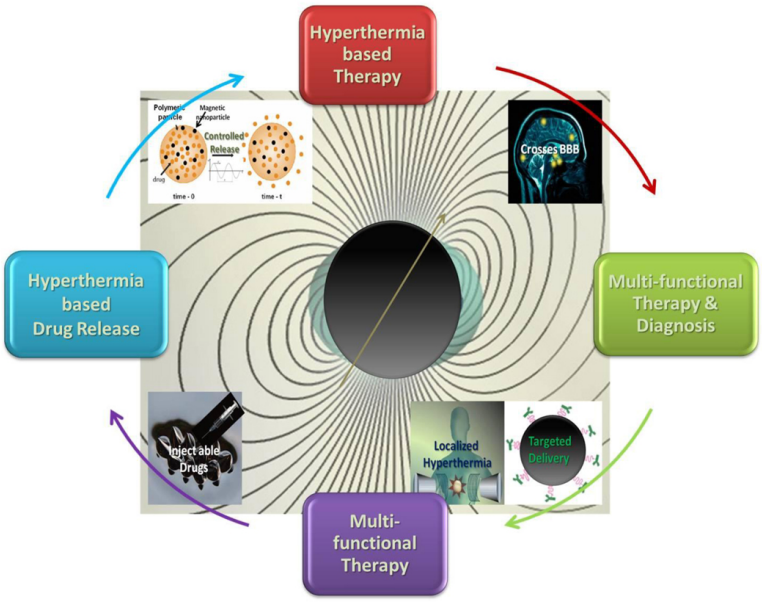

Figure 1.24: A schematic representation of some of the unique advantages of magnetic nanomaterials for hyperthermia-based therapy and controlled drug delivery. Reprinted with permission from [131].

For instance, in a report by Thomas and coworkers, the heating of Zn–doped Fe_2O_4 magnetic nanoparticles incorporated inside mesoporous silica nanoparticles carrying model cargo (like a drug) and capped with a molecular valve (curcubit[6]uril), was shown to be used as an external and remotely–controlled trigger for controlled drug release (Figure 1.25).

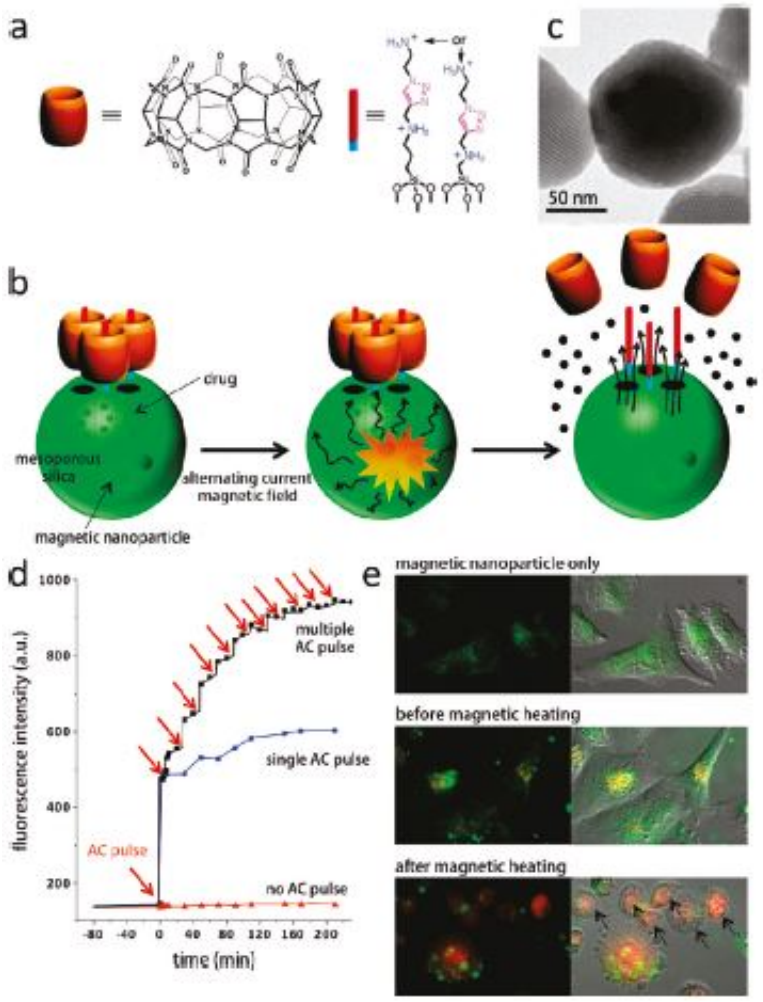

Figure 1.25: Magnetically triggered drug release system. (a) Chemical structure of thread and capping molecule. (b) Schematics of nanoparticles, molecular machines, assembly, and remote-controlled drug release. The particles and machines are not drawn to scale. (c) TEM image of Zn–Fe_2O_4 nanoparticles–encapsulated mesoporous silica nanoparticles. (d) Drug release profile monitored during the AC field application with multiple AC field pulse (red arrows), single initial pulse, and no pulse. (e) Fluorescence image and differential interference contrast (DIC) image of MDA-MB-231 cancer cells treated by magnetic nanoparticles only and drug with the nanoparticles in the silica carrier before and after the application of magnetic heating. Reprinted with permission from [45]. Copyright 2010 American Chemical Society.

The thermal energy of the MNPs when placed in an external magntic field, caused a significant pressure buildup and subsequent removal of the molecular valves and the release of the cargo (Figure 1.25b). The controlled cargo release is demonstrated by

the application of a pulsed magnetic field where the release of a fluorescent dye (Rhodamine B) is observed in each pulse in a staircase-like fashion (Figure 1.25d). Doxorubicin and magnetic nanoparticles-loaded porous nanoparticles with FITC (fluorescein isothiocyanate) for green fluorescence are tested for the treatment of cancer cells (Figure 1.25e). When cells transfected with silica nanoparticles containing doxorubicin are treated with an AC field, red fluorescence from the released doxorubicin from the silica particles and cell shrinkage and death are apparently observed. This result indicates that magnetic nanoparticles are effective as an actuator for controlled drug release from a carrier in a noninvasive and remote way.

Gold Nanoparticles

Apart from the use in delivery of therapeutic cargo like drugs and siRNA to tumor cells, metal nanostructures have garnered significant research attention because of their unique and tunable surface plasmon resonance (SPR) properties. At the resonant frequency, the incident photons can either be scattered (at the same frequency but in all directions) or absorbed and subsequently converted into phonons (i.e., vibrations of the lattice). Therefore, the SPR peak of a metal nanostructure typically includes both scattering and absorption components. The absorption component can be tuned by varying the the size, shape, and chemical composition of the nanostructures. Hence gold nanostructures serve as light-activated nanoscopic heaters, especially for the selective near-IR laser photothermolysis of cancer cells.

Gold nanoparticles conjugated to antibodies can be selectively targeted to cancer cells without significant binding to healthy cells [132, 133]. Irradiation of the cancer cells selectively labeled with the nanoparticles with a laser of frequency overlapping with the LSPR absorption maximum of the nanoparticles results in selective heating and destruction of cancer cells at much lower laser powers than those required to destroy healthy cells to which nanoparticles do not bind specifically. Gold nanoparticles (10–50 nm) offer 5 or more orders of magnitude larger absorption coefficients compared with conventional dyes; thus much lower laser energies can be used to achieve cell destruction, making therapy minimally invasive [132, 133]. Further, the therapy can be combined

with dark-field imaging, which is a significant advantage over other nanostructures such as quantum dots or carbon nanotubes, which can achieve only one of the two, imaging or therapy.

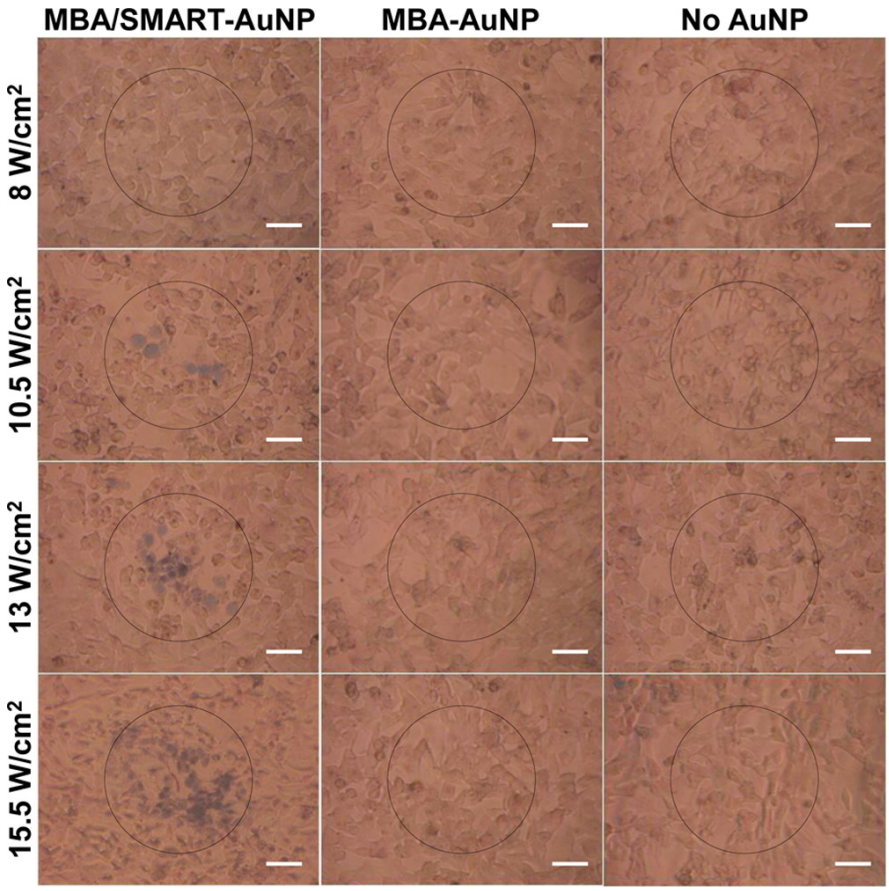

Figure 1.26: Photothermal therapy using MBA/SMART–AuNPs. B16 F10 cells were coincubated with MBA/SMART–AuNPs (left column), MBA–AuNPs (middle column), or with no NPs (right column). Laser fluence rates are 8, 10.5, 13, and 15.5 W/cm^2 from top to bottom rows. Circles: position of laser spot. Scale bar: 100 μm. Reprinted with permission from [28]. Copyright 2013 American Chemical Society.

For instance, it was recently demonstrated that rapid aggregations of the gold NPs shifted shifts the plasmon absorption to far-red and near-infrared. The absorption shift to longer wavelength was used for photothermal cancer therapy as it guarantees maximal tissue penetration for potential therapeutic applications. The gold nanoparticles show selective and efficient destruction of cancerous cells with an intensity threshold of 5 W/cm^2 to induce the thermal destruction. In the intensity range 515 W/cm^2,

the circular area of damaged cells increases linearly with the irradiation power density. This shows a new proof-of-concept for photothermal cancer therapy that exploits collective plasmon modes of metal nanoparticles. (Figure 1.26) [28]. Apart from gold nanoparticles, other gold nanostructures like Au nanocages, offer facile control of the LSPR peak into the near-IR region, which is of great use in biological systems. In a study by Xia and coworkers, the selective photothermal destruction of cancer cells *in vitro* using immuno–Au nanocages was successfully demonstrated [134].

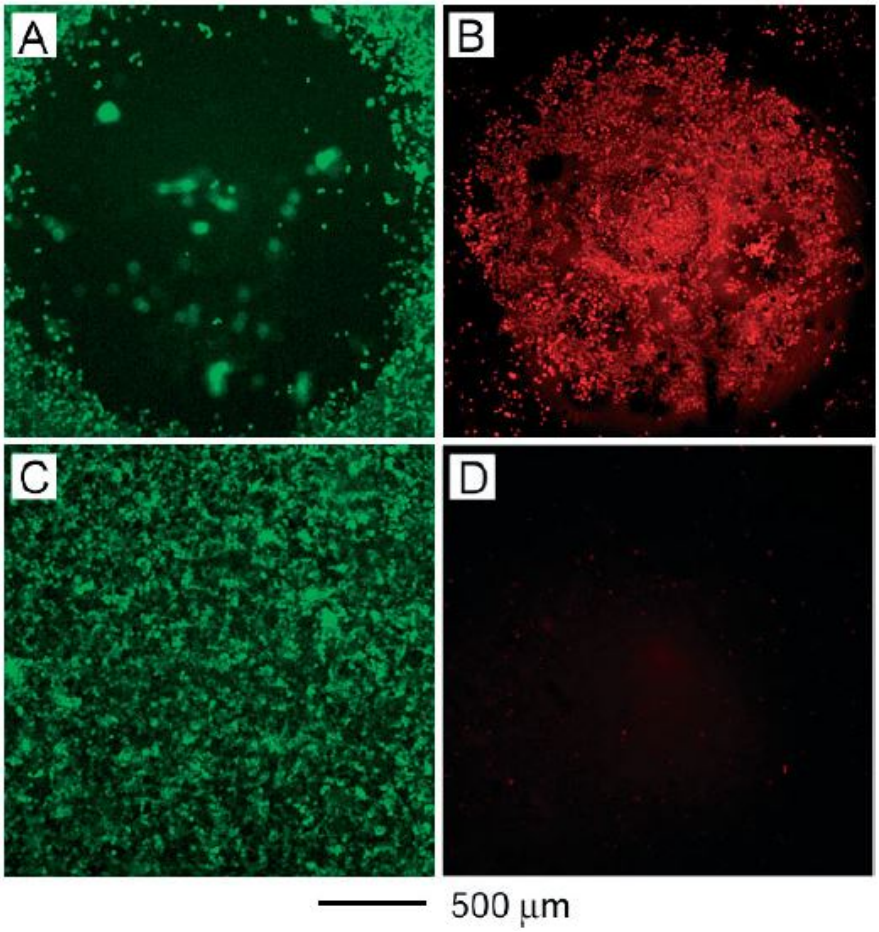

Figure 1.27: Photothermal effect of HER2-conjugated Au nanocages. SK–BR–3 breast cancer cells that were treated with immuno–Au nanocages and then irradiated by 810 nm laser at a power density of 1.5 W/cm^2 for 5 minutes. A well-defined circular zone of dead cells was revealed by: (A) calcein AM assay, where green fluorescence indicates live cells, and (B) Ethidium homodimer–1 (EthD–1) assay, where red fluorescence indicates dead cells. In a control experiment, cells irradiated under the same conditions but without incubating with immuno Au nanocages maintained viability, as indicated by (C) calcein fluorescence assay, and (D) the lack of intracellular EthD–1 uptake. Reprinted with permission from [134]. Copyright 2007 American Chemical Society.

For this study, 45 nm Au nanocages were prepared with their SPR peaks tuned to 810 nm to match the center wavelength of laser irradiation used for photothermal experiments. The nanocages were functionalized with the HER2-antibody to target the EGFR2/HER2 receptor, which is highly overexpressed on the surface of SK-BR-3 breast cancer cells. After incubation with the immuno Au nanocages, the SK-BR-3 breast cancer cells were irradiated with a femto-second Ti:Sapphire laser at varying power densities for 5 minutes. The immunotargeted Au nanocages were found to have a greater area of cell death on laser irradiation, with minimal cell death in absence of the laser or absence of the nanocages (Figure 1.27).

The approach of using gold nanostructures for selective targeting and photothermal therapy is general and versatile. Cancer is only one example. The use of plasmonic nanoparticles can be extended to other biological applications, for example, destruction of viruses or bacteria or controlled localized denaturation or cleavage of proteins and nucleic acids, potentially useful for diagnostic or therapeutic goals. Chemists have now established excellent control over the surface chemistry, biofunctionalization, and optical properties of metal nanoparticles aimed at targeting desired biological systems.

1.2.2 Engineered Organic Nanomaterials

Dendrimers

Dendrimers are synthetic polymers that are built from a series of branches around an inner core. They are tree-like or star-shaped polymers that adopt generally a quasi-spherical shape [135]. They have unique molecular weights and their dimensions are extremely small, having diameters (depending on the generation) in the range of 2-10 nm. Dendrimers have been finding increasing use in the field of drug and gene delivery because they are synthetic, highly branched, monodisperse polymers in the nanometer size range which offer the control that modern drug delivery and targeting demands, namely: control of chemical nature of carrier, control of molecular weight, control of surface and internal structure and character, vital in targeting and control of dimensions. In addition, genetic material (like siRNA and plasmid DNA) can be attached to the surfaces of dendrimers with relative ease due to the high concentration of positively charged functional groups. These functional groups can also be modified to attach targeting moieties like folic acid, transferrin and antibodies [136]. Amongst these, the earliest synthesized and commercialized dendrimers are polyamidoamine (PAMAM) dendrimers.

Gebhart et al. compared the performance of several dendrimeric systems and found that the transfection efficiency depends not only on the vector molecule but also the type of cells to be transfected [137]. Therefore, several investigations on developing more efficient and less toxic dendrimers are currently ongoing to control the cellular behavior. To this end, Santos et al. showed that PAMAM dendrimers, without any surface functionalization, were able to transfect the bone morphogenetic protein-2 (BMP-2) to MSCs, although at a low efficiency. The group also showed *in vitro* osteogenic differentiation of the MSCs by checking the expression levels of various osteogenic markers [135]. However, MSCs are very promising and clinically relevant due to their tumor homing properties. Thus, increasing the transfection efficiency of the PAMAM dendrimers was vital. The same group then functionalized the PAMAM dendrimers with arginine-glycine-aspartic acid (Arg-Gly-Asp, RGD) peptide sequence, which provided a major

recognition system for the integrin receptors expressed on the MSCs. RGD tripeptide sequence play a key role in cell adhesion and has been used in numerous studies as a cell-targeting agents in antitumor therapies, imaging and drug/gene delivery [138]. In this study, Pandita et al. increased the density of the surface charges on the PAMAM dendrimers and conjugated them to RGD peptides, thus forming nanoclusters of RGD on the dendrimers. These nanoclusters complexed with pDNA were able to enter the MSCs with high efficiency through a mechanism which resulted from a balance between electrostatic interactions between the positively charged complexes and the negatively charged cell surface and the specific interactions between the RGD peptides and the integrin receptors expressed on the surface of MSCs. They showed that the RGD motifs played a big role in improving the transfection efficiency, with the sixth generation of the PAMAM dendrimer (G6) having 8 arms of RGD being the most efficient (Figure 1.28). EGFP, luciferase and BMP-2 pDNA were delivered and the proteins were successfully expressed by the MSCs [138].

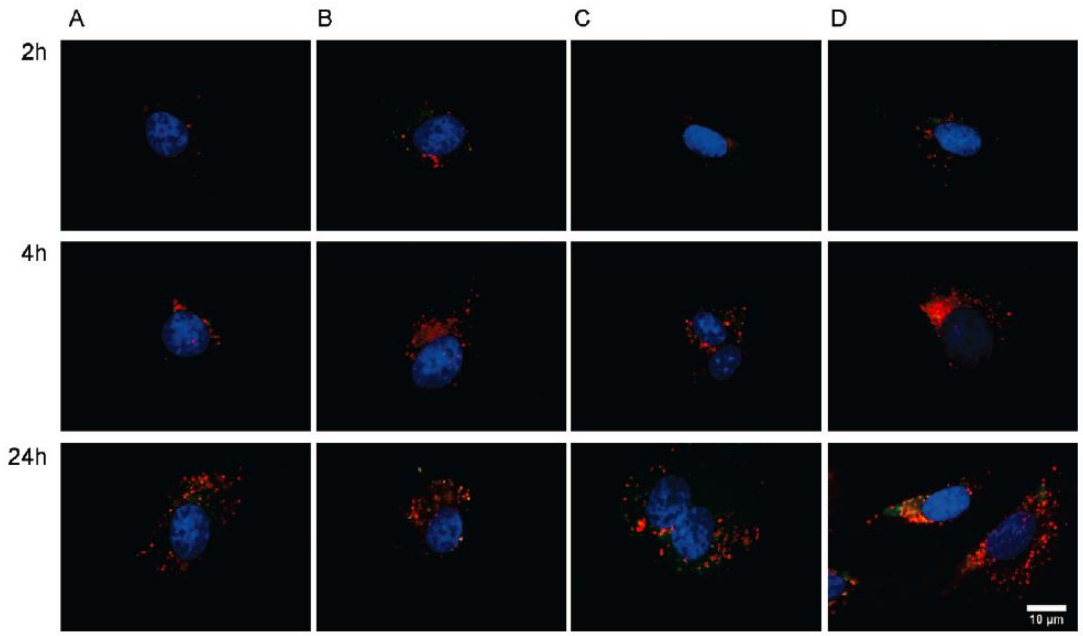

Figure 1.28: Dendrimer-based gene delivery into mesenchymal stem cells. Cellular distribution of dye-labeled pDNA (red) in MSCs at 2,4, and 24 h post-transfection. (A), (B), (C), and (D) represent confocal fluorescent images showing MSCs transfected with PAMAM–G5, RGD8-G5, G6, and RGD8-G6 respectively. The cell nuclei were stained with DAPI (blue), and the acidic endosomes and lysosomes were stained with LysoSensor Green DND-189 (green). Reprinted with permission from [138]. Copyright 2011 American Chemical Society.

Besides naked dendrimers and surface-functionalized dendrimers, dendrimer composites of iron oxide nanoparticles, also known as magnetodendrimers, represent a versatile new class of contrast agents for MRI. They were developed by Bulte at al. and were shown to efficiently label mammalian cells, including neural stem cells and mesenchymal stem cells [38]. They were shown to have an oligocrystalline structure of 7-8 nm. It was observed that labeling NSCs and MSCs with magnetodendrimers did not affect their growth rate and they exhibited a growth rate which was similar to that of unlabeled stem cells. The cellular uptake of these composites is through a non-specific adsorption process, thus offering a great opportunity to label a variety of mammalian cells without regard to their origin or animal species (Figure 1.29).

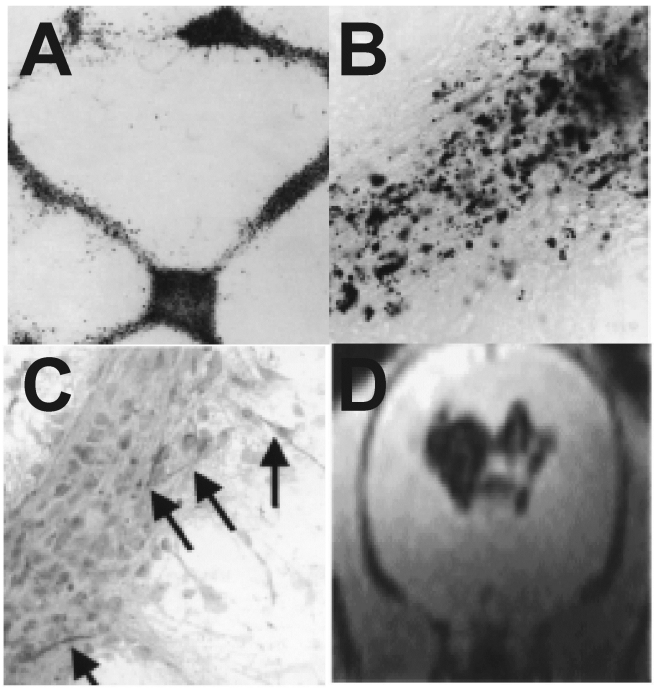

Figure 1.29: Tracking neural stem cells (NSCs) labeled with magnetodendrimers (MD-100). (A) NSCs labeled with MD-100 stained with Prussian Blue images after 24 h. (B) MD-100-labeled NSCs at higher magnification. (C) MD-100-labeled NSCs immunostained with anti-MAP2 (neuronal marker) confirming that labeleing NSCs with MD-100 does not affect the neuronal differentiation of NSCs. (D) *In vivo* MR image of MD-100-labeled NSCs 42 days after intraventricular transplantation. Reprinted with permission from [38].

Liposomes

First described in 1965 [139], the liposome is the most established drug-delivery vehicle, with many clinical products to date. Liposomes consist of amphiphilic lipid molecules that assemble into bilayered spherical vesicles. This assembly process usually requires externa energy from sonication, homogenization, shaking or heating [140]. Phosphatidylethanolamine and phosphatidylcholine are common building blocks of liposomes and cholesterol is frequently incorporated into liposomal membranes to enhance their stability and rigidity. The emergence of stealth liposomes, or polyethyleneglycol (PEG)-coated liposomes, took liposomal drug delivery to a whole new level as they increased the in vivo circulation half–life of liposomes from a few hours to approximately 45 h [141]. Currently, liposomal products used for cancer treatment include

Doxil [142,143] DaunoXome® [144,145], DepoCyt® [146,147] and ONCO-TCS, which are liposomal formulations of doxorubicin, daunorubicin, cytarabine and vincristine, respectively.

Drug encapsulation in liposomes can be achieved by two different methods. First, the drugs can be dissolved in an aqueous solution to hydrate lipid films. This process results in the formation of drug-loaded multilamellar liposomes that can then be extruded through filters with a predetermined pore size to form unilamellar liposomes. Second, unilamellar liposomes are first synthesized and subsequently incubated in an aqueous drug solution. The drug molecules can diffuse passively through the liposomal membranes until the aqueous cavity is saturated. The unloaded drugs will then be removed from the drug-loaded liposome solution through dialysis, column chromatography or centrifugation. Owing to their unique structure, liposomes can simultaneously load hydrophilic drugs in their aqueous core and hydrophobic drugs in their lipid bilayered membrane [148]. In addition, several other targeting and imaging modalities can be incorporated as part of the liposomal formulationa as shown in Figure 1.30. These properties makes liposomes a highly versatile platform for combination drug delivery.

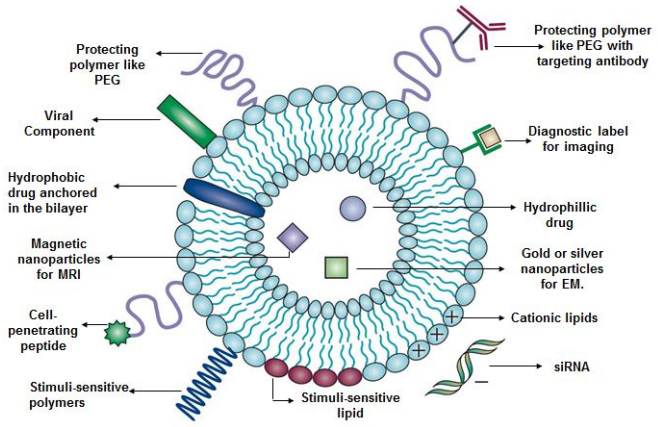

Figure 1.30: Synthesis and functionalization of liposomes to confer multifunctionality for drug delivery and imaging. Reprinted with permission from [110].

An early attempt to create dual drug-loaded liposomes was reported by Agrawal et al. [149]. In the study, the authors encapsulated two anti–leukemia drugs, 6-mercaptopurine and daunorubicin, into a single liposome and examined their loading efficiency as well

as their *in vitro* cytotoxicity. The two drugs have dissimilar working mechanisms as 6-mercaptopurine hinders purine biosynthesis and daunorubicin inhibits DNA topoisomerase II [150]. The dual drug-loaded liposomes exhibited higher cytotoxicity against Jurkat and Hut76 T-cell lymphoma as compared with monodrug-loaded liposomes containing either 6-mercaptopurine or daunorubicin, suggesting that the combination of these two mechanistically different drugs can generate higher therapeutic efficacy.

Another example of liposome-based combination therapy is the co-delivery of siRNA and chemodrugs. siRNA is an emerging class of cancer therapeutics that interferes with gene expression by targeting specific mRNA sequences. A recent study by Saad et al. developed a liposome system to deliver BCL2 (a protein responsible for anti-apoptotic cellular defense) and MRP1 (a multidrug resistance-associated protein) targeted siRNA in combination with doxorubicin against human H69AR lung cancer cells [151].

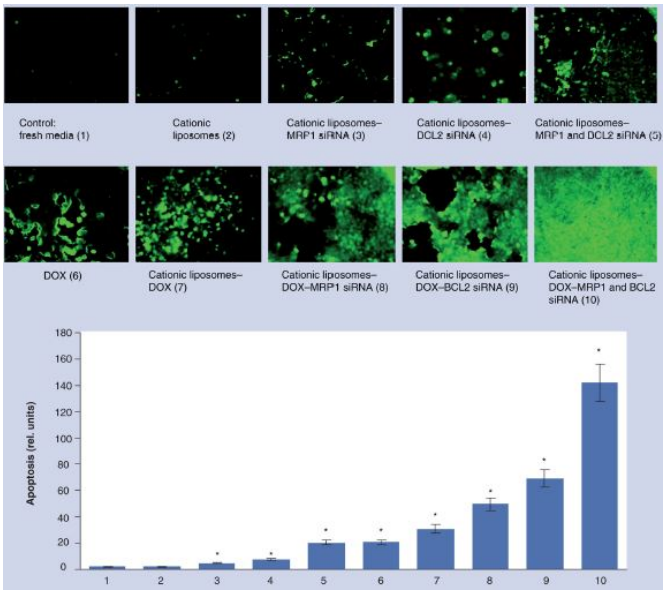

Figure 1.31: Liposomal codelivery of siRNA and Doxorubiciin for overcoming multidrug resistance in lung cancer cells. Apoptosis induction in multidrug-resistant H69AR human lung cancer cells. Typical fluorescent microscopy images of cancer cells incubated for 48 h with the indicated formulations and stained by TUNEL. Quantitative analysis of the intensity of fluorescence (apoptosis induction) is presented on the bottom panel. Means standard deviation are shown [151].

A positively charged 1,2-dioleoyl-3-trimethylammonium- propane is used to construct a cationic liposome, which was then loaded with doxorubicin through an incubation method and subsequently incubated with siRNA. The liposome-siRNA complex formed through electrostatic interaction as the negatively charged phosphate groups on siRNA molecules bind to the positively charged liposomal surface. An in vitro cytotoxicity study showed considerable reversal of cellular resistance in MDR lung cancer cells (Figure 1.31).

The above mentioned studies demonstrates the versatility of liposomes as a multidrug nanocarrier for synergistic cancer treatment and multimodal imaging.

1.2.3 Biodegradable Nanomaterials

PLGA Nanoparticles

Advances in biomaterials research have led to the emergence of biocompatible and biodegradable polymeric nanoparticles for drug-delivery applications. Several synthetic polymers approved by the US-FDA such as poly(lactic-co-glycolic acid) (PLGA) and polycaprolactone (PCL) and several natural polymers such as chitosan and polysaccharides have been investigated extensively for nanoparticle synthesis [152–155].

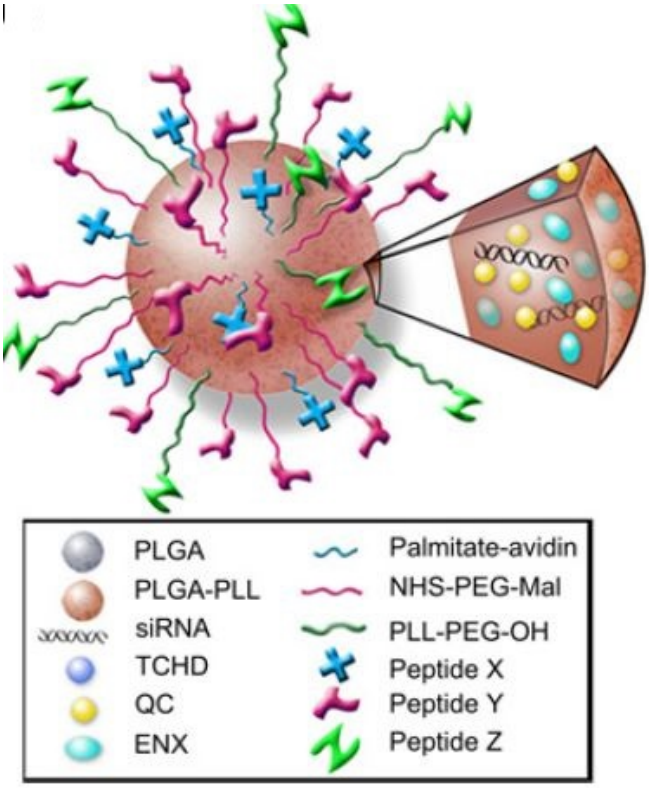

Figure 1.32: Schematic representation of multifunctional PLGA nanoparticles for targeted drug and siRNA delivery to tumors. TCHD: transcyclohexane–1,2–diol; QC: quinacrine, a chloroquine analogue; ENX: Enoxacin or (1–ethyl–6–fluoro–1,4–dihydro–4–oxo–7-(1–piperazinyl)–1,8–naphthyridine–3–carboxylic acid, a molecule known to enhance the effect of any siRNA. Reprinted with permission from [156].

Compared with liposomes, polymeric nanoparticles generally have higher stability, sharper size distribution, more tunable physicochemical properties, sustained and more controllable drug-release profiles, and higher loading capacity for poorly water soluble drugs. The polymer platform also offers higher synthetic freedom that allows particles

to be tailored for specific needs. Figure 1.32 shows the multifunctionality of PLGA nanoparticles for drug delivery applications. Owing to these unique characteristics, polymeric nanoparticles have attracted tremendous interests from academia, industry and clinic, although they are still in a relatively early stage of development.. Polymeric nanoparticles typically consist of amphiphilic diblock copolymers that self assemble into nanoparticles in aqueous solutions. For in vivo drug delivery, PLGA and PEG are popular choices for the hydrophobic and the hydrophilic block, respectively, as PLGA can hydrolyze into lactic acid and PEG can significantly reduce nonspecific cellular uptake by forming a stealth layer [157, 158]. PLGA-based nanoparticles have several important advantages. PLGA was approved by the Food and Drug Administration (FDA) in 1969 and, since that time, has been in continuous, safe clinical use. Drug-releasing particles of PLGA were first approved in 1989 (Lupron Depot), and are widely used, in large measure because of their reliability in controlling the release of agents over periods ranging from days to weeks, which is important for producing a persistent therapeutic effect. Furthermore, because nanoparticles of PLGA are solid (unlike lipid and polyplexes), they are stable and able to protect nucleic acids from degradation during circulation in blood stream, making them good carriers for oligonucleotides such as siRNA. Additionally, PLGA nanoparticles can be modified for the attachment of negatively charged oligonucleotides (plasmid DNA and siRNA) and targeted delivery [143, 156].

Drug encapsulation is typically achieved by mixing the drugs with the polymer solutions during particle preparation process. One example is the co-encapsulation of verapamil together with vincristine to increase the chemosensitivity in drug resistant cancer cells. The dual drug-loaded nanoparticles were prepared by mixing PLGA, verapamil and vincristine in acetonedichloromethane solution at predetermined concentrations before solvent displacement and particle precipitation [159]. Another example can be found in the co-encapsulation of doxorubicin and cyclosporin A using polyalkylcyanoacrylate nanoparticles, in which the hydrophobic cyclosporin A (a potent inhibitor of P–glycoprotein, the major contributor for drug efflux and drug resistance) was added

together with doxorubicin to the polymerization medium to achieve dual drug loading [160]. In both studies, the dual drug–loaded nanoparticles showed markedly higher *in vitro* cytotoxicity against resistant cancer cell lines, providing a viable solution to the MDR effect of cancer cells that has plagued many cancer treatments.

In another approach, Zhang et al. reported an aptamernanoparticle bioconjugate that could co-deliver hydrophobic and hydrophilic drugs. In their study, the PLGA nanoparticles loaded with a hydrophobic chemodrug, docetaxel, were surface modified with oligonucleotides that serve both as targeting ligands and as intercalation sites for a hydrophilic chemodrug, doxorubicin [152]. The conjugate not only demonstrated targeted co-delivery of docetaxel and doxorubicin but also exhibited differential drug release kinetics. A drug release study revealed that the intercalated doxorubicin was released faster than the physically entrapped docetaxel. At the 6 h mark, approximately 80% of the doxorubicin and only approximately 45% of docetaxel were released (Figure 1.33).

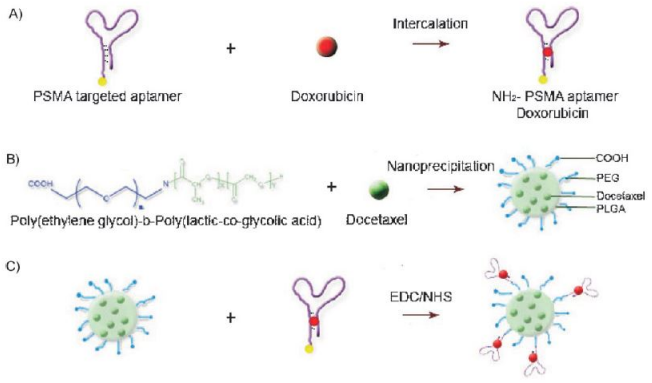

Figure 1.33: Schematic illustration of the PLGA nanoparticles for co-delivery of docetaxel and doxorubicin. A) the intercalation of a hydrophilic anthracycline drug, such as DOX within the A10 PSMA aptamer; B) the encapsulation of a hydrophobic drug, such as Dtxl, within the PLGA–b–PEG nanoparticles using the nanoprecipitation method; and C) nanoparticle–aptamer (NP–Apt) bioconjugates comprised of PLGA–b–PEG nanoparticles surface functionalized with the A10 PSMA aptamer for co–delivery of DTXL and DOX. Both drugs can be released from the bioconjugates over time. Reprinted with permission from [152].

This feature carries significant clinical implications as drug sequencing and scheduling are crucial parameters in combination chemotherapy [161,162]. The ability to modulate the release profile of different drugs independently enables more intricate designs that may further improve therapeutic efficacy of drug combinations.

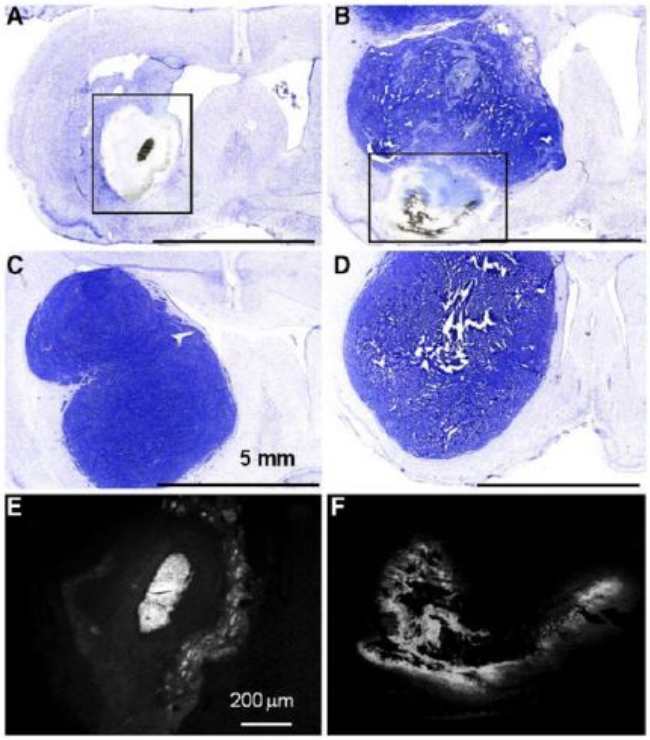

Figure 1.34: Convection-enhanced delivery of camptothecin-loaded polymer nanoparticles for treatment of intracranial tumors. Cresyl violet histopathology of rat brains. After tissue harvesting, cresyl violet was used to visualize the remaining tumor. Animals that survived until the end of the study (60 days) showed no remaining tumor (a). A cavity was formed at the site of the tumor location. Some animals that received a full dose of nanoparticles died prior to the end of the study (b); this animal died at day 20. In both sets of animals, residual nanoparticles delivered by CED were often visible (see boxes in a and b). Animals given CED of free drug (c) or CED of blank particles (d) had large tumors with evidence of a midline shift and altered ventricles due to the presence of the tumor. These animals died at days 17 (c) and 15 (d). Fluorescent imaging of sections shown in panels a and b reveal CPT (e, f). Bright fluorescence is due to CPT that remains in the brain. Reprinted with permission from [163].

Direct delivery of chemotherapy agents to the brain via degradable polymer delivery systems, such as Gliadel®, is a clinically proven method for treatment of glioblastoma multiforme, but there are important limitations with the current technology, including

the requirement for surgery, profound local tissue toxicity, and limitations in diffusional penetration of agents-that limit its application and effectiveness. Saltzman and coworkers recently demonstrated another technique for direct, controlled delivery of chemotherapy to the brain that provides therapeutic benefit with fewer limitations (Figure 1.34). In their approach, camptothecin (CPT)–loaded poly(lactic–co–glycolic acid) (PLGA) nanoparticles were infused via convection-enhanced delivery (CED) to a stereotactically defined location in the brain, allowing simultaneous control of location, spread, and duration of drug release. To test this approach, CPT–PLGA nanoparticles ($\sim$100 nm in diameter) were synthesized with 25% drug loading. When these nanoparticles were incubated in culture with 9L gliosarcoma cells, the IC_{50} of CPT–PLGA nanoparticles was 0.04 μM, compared to 0.3 μM for CPT alone. CPT–PLGA nanoparticles stereotactically delivered by CED improved survival in rats with intracranial 9L tumors: the median survival for rats treated with CPT–PLGA nanoparticles (22 days) was significantly longer than unloaded nanoparticles (15 days) and free CPT infusion (17 days). CPT–PLGA nanoparticle treatment also produced significantly more long-term survivors (30% of animals were free of disease at 60 days) than any other treatment. CPT was present in tissues harvested up to 53 days post-infusion, indicating prolonged residence at the local site of administration. These are the first results to demonstrate the effectiveness of combining biodegradable polymer–controlled release nanoparticles with CED in treating fatal intracranial tumors.

Polypeptides

Amino acids are joined together by peptide bonds to form polymers referred to as peptides or proteins. Peptides generally contain fewer than 40 amino acids, while proteins contain 50 or more. Between the two is a category called polypeptides. Molecular weight is also utilized for the definition, with peptides considered to have a molecular weight less than 5000 Da, and proteins a weight above this value. By this definition, insulin is the smallest protein available, having a molecular weight of 5800 Da. Peptides are considered the new generation of biologically active tools because they are key regulators in cellular and intercellular physiological responses, which possess enormous

potential for the delivery of several anticancer drugs and imaging agents. Originally, it was discovered that the full-length protein crossed the plasma membrane [164] and subsequently, small fragments were identified that could efficiently enter cells [165]. These discoveries, along with those identifying other peptides with membrane -crossing activities [166–170], served as the cornerstone for a new sub-field focused on the use of cell -penetrating peptides (CPPs) as molecular transporters. One that received a great deal of attention was the Tat peptide, derived from the HIV Tat transactivator protein [165].

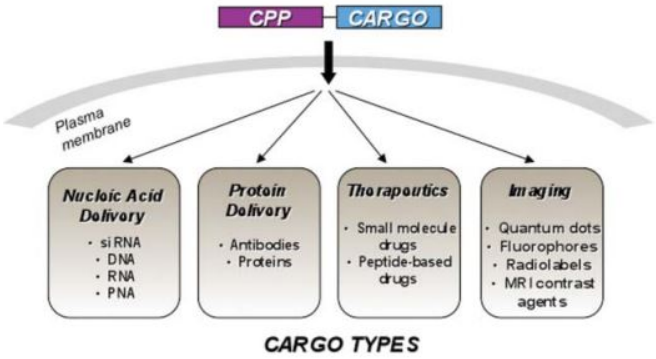

Figure 1.35: Applications of cell–penetrating peptides as molecular delivery vehicles.

Today, thousands of studies have been performed characterizing and optimizing CPPs as cellular delivery agents [167–171]. Chemists and biochemists have developed many variations of peptide structures that have elucidated important molecular features of CPPs that modulate activity [172–175]. Researchers in both the biological and medical sciences have developed numerous applications of these constructs , illustrating the utility of CPPs in these fields [167–171]. A variety of intracellular cargoes have been transported by Tat or other CPPs, including DNA [176], polymers [177], nanoparticles [4, 178], and liposomes (Figure 1.35) [179]. Clearly, CPPs are a powerful tool for transporting diverse materials across the cell membrane and have attracted the interest of an interdisciplinary scientific community.

For instance CPPs have been extensively used increasing the uptake and efficacy of several small-molecule drugs (Figure 1.36) [171, 180, 181]. Polyarginine conjugates of the hydrophobic drug Paclitaxel were shown to greatly improve the water solubility and

cellular uptake of this potent therapeutic [171, 182]. CPP conjugates of cyclosporine A were shown to exhibit qualities beneficial for treatment of psoriasis and other skin conditions [180]. When topically administered, the polyarginine aids penetration to cells in the underlying tissue, delivering a therapeutically useful amount of the anti-inflammatory molecule by facilitating passage through the stratum corneum.

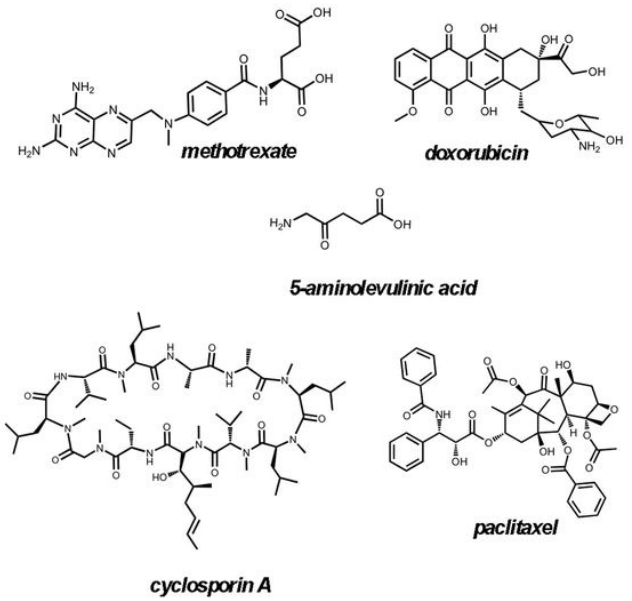

Figure 1.36: Small molecule therapeutics successfully delivered by CPPs.

CPPs have delivered photoactive drugs, e.g. the pro-drug 5-aminolevulinic acid, which is converted in the heme biosynthetic pathway to the photosensitizer, protoporphyrin IX; the delivery of this agent was made possible by coupling to penetratin [183]. CPPs can therefore be used to ameliorate properties of drugs–like extreme lipophilicity or poor trafficking–hat limit their usefulness. CPPs may also be useful for overcoming cancer-resistance in cells by diverting drugs away from efflux pathways. For example, doxorubicin conjugated to Tat [184] and transferrin [185,186] have been successful in exerting cytotoxic effects on doxorubicin-resistant cell lines. CPPs have enhanced uptake of methotrexate in cell lines resistant to this chemotherapeutic, further illustrating the therapeutic benefit of CPP-conjugated drugs [181]. While these drugs are inherently cell permeable, CPP-mediated delivery circumvents the effects of the efflux pumps and provides an effective means to override resistance.

The ability to visualize internal features and physiological structures of living organisms and observe cellular functions *in vivo* is vital for understanding, diagnosing, and treating disease. For example, directly visualizing diseased tissue during surgical procedures and identifying pre-disease states in patients will have profound implications in medicine. In biomedical research, assessing stem cell differentiation or following the dynamics of the immune cells in living animals will provide a fundamental understanding of these biological processes .

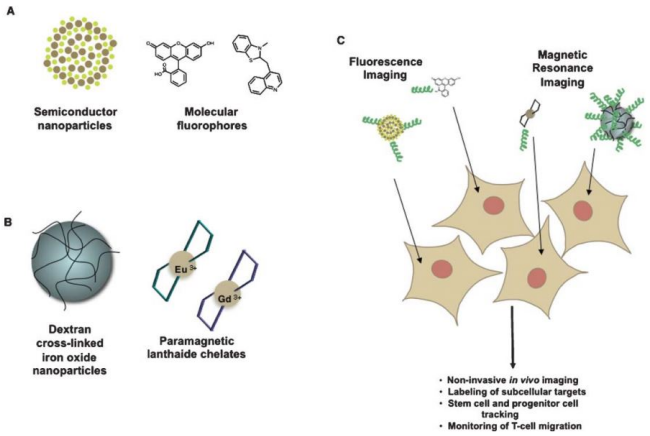

Figure 1.37: CPP–mediated delivery of imaging and diagnostic agents.

Non-invasive biomedical imaging techniques such as fluorescence imaging and magnetic resonance imaging (MRI) have been developed for these types of *in vivo* applications. As some useful imaging agents are not able to penetrate cells or tissues, CPPs have proven useful in this field as delivery vehicles (Figure 1.37). Fluorescence imaging relies on tracking molecular imaging agents and has been shown to be useful for visualizing tissues *in vivo*. However, poor cellular uptake, inadequate targeting, and the lack of photostability of fluorophores can be problematic. CPPs have been combined with imaging labels in an effort to optimize aspects of in vivo fluorescence imaging related to cellular targeting. Various fluorophore–CPP conjugates with improved stability and uptake have been developed as imaging agents [187, 188]. For example, fluorescein–doped monodisperse silica particles of approximately 70 nm in diameter were modified with Tat peptides for cellular delivery and shown to efficiently cross the blood–brain barrier, labeling the neuronal tissue of rats *in vivo* [187].

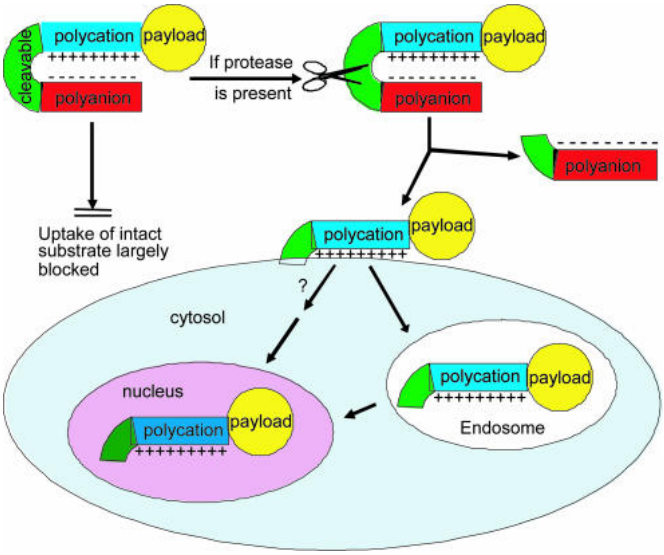

Figure 1.38: Schematic diagram of activatable CPPs. Cellular uptake induced by a cationic peptide is blocked by a short stretch of acidic residues attached by a cleavable linker. Once the linker is cleaved, the acidic inhibitory domain drifts away, and the cationic CPP is free to carry its cargo into cells. Reprinted from [188].

Another very elegant example of the application of CPPs for imaging was recently reported by Tsien and coworkers (Figure 1.38) [188]. A fluorescein-peptide hairpin was designed that took advantage of the increased number of extracellular proteases surrounding tumor tissues. The construct consisted of a polyarginine peptide covalently attached to a polyanionic segment, which would only be internalized upon proteolytic cleavage of the anionic domain and because the protease targeted is overexpressed on cancerous cells.

Considerable efforts have been made to design new drugs based on peptides and recent developments in technology and science have provided the means and opportunity to produce a stable as well as controlled-release form of peptidse and polypepeptide-conjugated drugs to combat aggressive diseases, including cancer and neurodegenerative disorders, and to increase patients quality of life. In the coming years, polypeptide-based drug delivery is surely poised to become the forerunner for clinical applications.

1.3 Conclusion

The emergence of nanotechnology has made a significant impact on clinical therapeutics in the last two decades, having highly attractive applications in cancer imaging and therapy. Nanotechnology-based platforms not only aid in delivering therapeutic cargoes in a controlled manner to various tumors but also help in tracking the delivered drugs after being uptaken by the target cells. Liposomes, polymeric nanoparticles, dendrimers and silica nanoparticles have been demonstrated to carry a variety of anticancer agents including cytotoxic drugs, chemomodulators, siRNA and antiangiogenic agents to tumor and stem cells. On the other hand, quantum dots, magnetic and metallic nnanoparticles have been excellent for multimodal imaging via non-invasive methods like fluorescence and MRI. However, there is a gradual loss of MRI signal due to cell division in magnetic nanoparticles and the inability to perform whole animal imaging restricts the clinical use of quantum dots *in vivo*.

For harnessing the true potential of of these nanoplatforms in a clinical setting, multimodal and multifunctional nanomaterials capable of incorporating the properties of several different nanomaterials into a single platform are required. Furthermore, precise control over the particle composition and preparation would be imperative for ensuring ratiometric drug loading and temporal drug release, both of which would carry significant clinical implications in cancer treatments. Although rapid advancements in developing such nanomaterials for tumor imaging and therapy have taken place in the past decade, novel biodegradable materials that can perform the above said functions while overcoming challenges associated with controlled release of cargo, nanoparticle toxicity and clearance from the body, need to be developed. These biodegradable platforms can incorporate nanomaterials to deliver therapeutics in a controlled manner depending upon an external stimulus, such as a magnetic field or light.

Overall, nanomaterials have played a significant role in advancing the fields of medical diagnostics and cancer therapy. Moreover, the advancement in nanotechnology-based approaches allows scientists in cell biology and physiology to investigate targeted

bio-interactions at the fundamental molecular level. What is now required is an inter-disciplinary approach from a high level of expertise in each field of science in order to help advance these technologies into the clinic.

1.4 Overview of Dissertation

All the above nanotechnology-based approaches provide remarkable inspiration for anyone aspiring to develop newer approaches for drug delivery and imaging in order to create better methods for the diagnosis and treatment of aggressive cancers. I took great inspiration from such techniques and started working on developing multimodal drug and siRNA delivery systems using novel nanomaterials. My aim was to develop newer materials with superior physical and chemical properties for use as cancer theragnostics. The approaches I developed over the course of my doctoral work could be used for applications involving cancer and stem cells alike, but I focused on their applications in glioblastoma (brain cancer) cells. Brain cancer is one of the most aggressive and difficult to treat cancers, with a median survival of 8-10 months. The development of novel theragnostics would eventually help in creating better treatment methods, that could be translated to the clinic in the near future.

We started with the development of non-toxic quantum dots (QDs) for the imaging and delivery of siRNA into brain cancer and mesenchymal stem cells, with the hope of using these QDs as multiplexed imaging and delivery vehicles. We were quite successful at overcoming the toxicity issues associated with the use of conventional quantum dots, which generally consist of Cadmium and Selenium. These non-toxic QDs not only enabled us to image brain cancer and stem cells with high efficiency, but also allowed us to deliver siRNA to knockdown the target gene in brain cancer cells. Overall the project provided inspiration to explore the use of these non-toxic QDs as imaging probes for brain tumors.

In another project we developed a biodegradable dendritic polypeptide-based nanocarrier, in order to co–deliver multiple anticancer drugs and siRNA to target brain tumor cells in a controlled manner, to elicit a combined therapeutic effect. The polypeptide-based system was not only capable at loading the anticancer drugs (Doxorubicin and Suberoylanilide hydroxamic acid (SAHA), a histone deacetylase inhibitor) in high amounts, but also efficiently complexed siRNA, against the EGFRvIII oncogene, which is a mutant form of the epidermal growh factor receptor (EGFR) and found to be expressed

only in brain cancer cells. The drugs were released using orthogonal physical/chemical stimuli (pH and reductive environment). Using our dendritic polypeptide-mediated co-delivery of drugs and siRNA, we could increase the potency of the drugs by 10 fold, thereby leading a synergistic inhibition of brain tumor cell proliferation.

This dissertation provides the details of my work on all projects related to the development of multifunctional nanomaterial-based drug delivery and imaging systems.

Chapter 2

Nanomaterial-based Molecular Imaging and Multimodal Diagnostic Agents

Nanotechnology is a rapidly emerging field which holds great promise for revolutionizing detection and diagnosis of several diseases. Early detection of dieases such as cancer at the cellular level, even before anatomic anomalies are visible, is critical to more efficacious and cost-effective diagnosis and therapeutic advances. A wide variety of nanomaterial-based bioimaging techniques (e.g., optical imaging, Raman imaging, ultrasound, computed X-ray tomography, magnetic resonance imaging (MRI), and positron emission tomography) are commonly employed for clinical diagnostics and scientific research. While all of these methods use a characteristic energy–matter interaction to provide specific details about biological processes, each modality differs from another in terms of spatial and temporal resolution, anatomical and molecular details, imaging depth, as well as the desirable material properties of the agents needed for imaging. On many occasions, it is advantageous to apply multiple complimentary imaging modalities for faster and more accurate prognosis. Since most imaging modalities employ exogenous agents to image and improve the signal-to-noise ratio, the development and use of multimodal imaging and contrast agents is considered to be highly advantageous for obtaining improved imagery from sought-after imaging modalities. Towards this end, we describe the synthesis, characterization and bioapplications of nanoparticulate-based agents for noninvasive bioimaging. Specifically, we developed non-toxic quantum dots (QDs), which are highly fluorescent nanoparticles, for simultaneous imaging and delivery of siRNA into tumor and stem cells.

2.1 Generation of a Library of Non-toxic Quantum Dots for Cellular Imaging and siRNA Delivery

2.1.1 Introduction

Dissecting the spatio-temporal interaction of biomolecules inside cells at the subcellular level is an important facet of molecular cell biology and chemical biology. Over the last few decades, a variety of fluorescent molecular probes have been developed to investigate these complex bio-interactions for both in vitro and in vivo cellular imaging and subcellular detection. In particular, semiconductor nanoparticles like quantum dots (QDs) have shown great potential as nanoparticle fluorescent probes due to their excellent physiochemical properties, which allow them to overcome the limitations of conventional fluorescent probes such as organic dyes and fluorescent proteins [2, 189]. These unique attributes of QDs have proven to be crucial in elucidating the intricate interactions through which small molecules and biomolecules (e.g. proteins, peptides and nucleic acids) bind to their targets in specific signaling cascades [190–193]. While QDs are excellent molecular probes, they also can be used as effective delivery vehicles for several therapeutic biomolecules. For example, the use of QDs for the simulataneous imaging and delivery of small interfering RNA (siRNA) for selectively knocking-down target oncogenes in tumor cells has been successfully demonstrated [93, 192, 194, 195]. However, the major limiting factor in harnessing the maximum potential of QDs as multifunctional imaging probes and delivery systems is their inherent cytotoxicity; most of the well-established QDs are composed of highly toxic elements, such as cadmium (Cd), selenium (Se) or tellurium (Te) [191, 196]. Owing to this obstacle, the wide applications of QDs are currently delayed and the main focus of QD imaging has been limited to the cell and small animal studies. In response to the above issues, the recent development of I-III-VI_2 type QDs [73–78] like $AgInS_2$ [75], $CuInS_2$ [74, 76] and ZnS-$AgInS_2$ [77] offers better control of band-gap energies and demonstrates the great potential of these QDs as non-toxic molecular probes. For instance, several research groups have successfully synthesized ZnS-$AgInS_2$ (ZAIS) QDs through the decomposition of single source

precursors using thermal [77], hydrothermal [197], photothermal [198] and microwave-assisted methods [199]. Yet, these conventional synthetic methodologies for preparing I-III-VI_2 type QDs have several shortcomings such as high reaction temperatures, poor control of growth rates, long reaction times, difficulty of high throughput synthesis, and the need for complicated synthetic procedures to prepare QDs with different emissions profiles, all of which would be critical in investigating the diversity and dynamic processes of multiple biomarkers in cancer and stem cells. Thus, in order to harness the full potential of QDs as biological imaging probes as well as drug delivery platforms for clinical and translational research, its is imperative to develop a simple and straightforward methodology that affords both the synthesis of non-toxic QDs and the versatility of generating a library of QDs with tunable properties favoring their use as imaging agents in biology.

Herein, we describe a novel sonochemical approach for the high throughput synthesis of a library of biocompatible Zn_xS-$Ag_yIn_{1-y}S_2$ (ZAIS) quantum dots with tunable physical (photoluminescence, PL) properties, thereby allowing them to be used as multifunctional nanoparticles for the simultaneous imaging and effective delivery of siRNA to brain tumor cells with negligible cytotoxicity. These ZAIS QDs also proved to be useful for imaging stem cells, which are otherwise quite sensitive towards nanomaterial-based molecular imaging probes .

2.1.2 Results and Discussion

A sonochemical synthetic method uses ultrasound irradiation to drive the main synthetic reaction process. With the rapid growth of its use for applications in material science, the sonochemical synthetic approach is particularly attractive for the preparation of novel nanomaterials. Its advantages include a high reaction rate (for e.g., its possible to generate a whole library of nanoparticles of several compositions in a span of few hours), controllable reaction conditions and the ability to form nanoparticles with uniform shapes, narrow size-distributions and high purity in relatively little time and at ambient conditions. We therefore attempted to use this methodology for the facile synthesis of a whole library of ZAIS QDs with tunable emission profiles for use as a

biological imaging probe in cancer and stem cels and as a siRNA delivery vehicle.

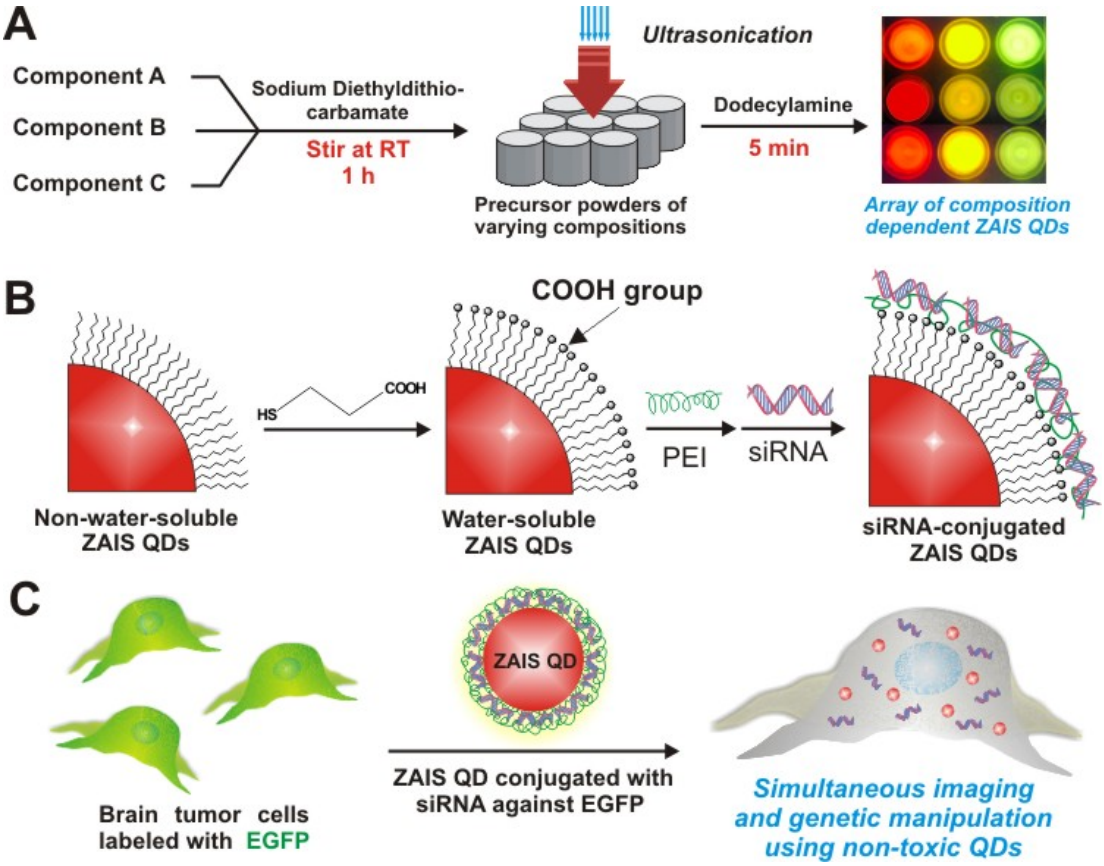

Figure 2.1: Synthesis of a library of ZnS-$AgInS_2$ QDs for simultaneous imaging and delivery of siRNA. (A) Synthetic procedure to obtain a library of dodecylamine-capped hydrophobic ZAIS QDs. (B) Conversion of the the hydrophobic ZAIS QDs into water-soluble ones via ligand exchange with 3-mercaptopropionic acid (MPA) followed by attachment of siRNA using a layer-by-layer approach. (C) Delivery of the siRNA against EGFP using ZAIS QD-siRNA conjugates into brain cancer cells overexpressing EGFP. Reprinted with permission from [107].

The photoluminescence of ZAIS QDs is composition-dependent and not size dependent

The library of ZAIS QDs was synthesized via the sonochemical decomposition of the organometallic precursor $(Ag_yIn_{1-y})Zn_x(S_2CN(C_2H_5)_2)_4$ at ambient conditions. Compared to the traditional synthetic methods for preparing QDs, this approach does not require high-temperature and high-pressure conditions. The resulting ZAIS QDs exhibited intense emission at room temperature, regardless of the size of the particles

(Figure 2.2).

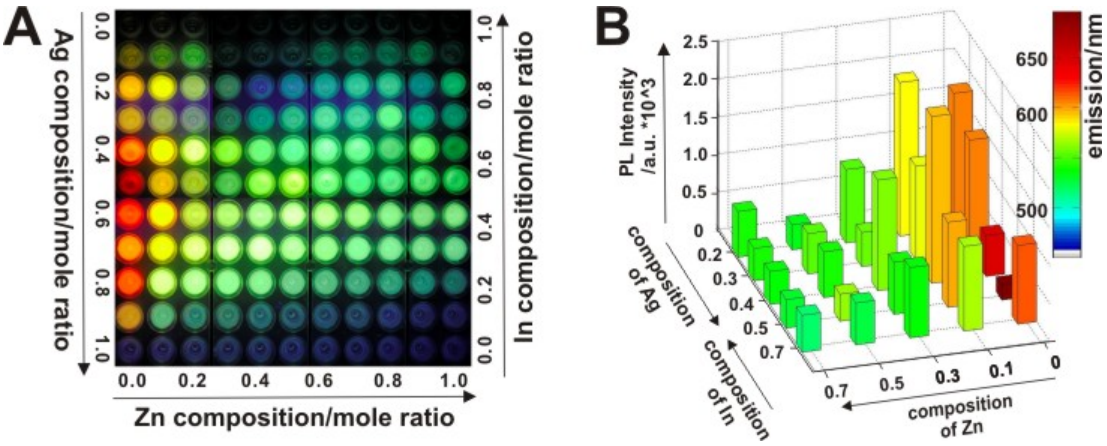

Figure 2.2: Photoluminescent properties of the ZAIS QD library. (A) Representative fluorescent image of the entire library of ZAIS QDs with varying compositions (Zn_xS-$Ag_yIn_{1-y}S_2$) synthesized via the sonochemical approach. (B) Heat map depicting the PL intensity (z axis) vs. Zn and Ag/In concentrations (x and y axis) for select compositions of the ZAIS nanoparticles library. Column color indicates the maximum emission wavelength. Reprinted with permission from [107].

More interestingly, the energy gap of the ZAIS QDs and their emission wavelength was controlled by varying the concentration of each precursor element. For instance, the emission of the ZAIS QDs could be tuned from 480 nm (Blue QD) to 700 nm (Red QD) by just varying the mole ratios of zinc (Zn), silver (Ag), and indium (In) in the precursor solutions (Figure 2.2A). It is worthwile to note that as compared to conventional CdSe or CdTe QDs, which show size-dependent fluorescence properties, our composition-dependent tunable fluorescence of the ZAIS QDs presents a unique advantage for obtaining QDs with emission in the near-UV range (blue or blue-green emission). This observation can be explained by the fact that a blue-colored CdSe QD needs to be less than 2.0 nm in size, which is practically impossible to obtain using traditional thermal decomposition techniques. After assessing the optimum conditions for obtaining the desired emission profiles, we observed that for a given concentration of precursor ions, ultrasonication for 5 minutes at 20 kHz and 200W output power, gave the highest emission intensity. Figure 2.2B depicts a 3D heat map which summarizes the physical and chemical properties of the partial ZAIS QD library. For the different combinations of the precursor elements (i.e. Zn, Ag, and In), the 3D heat map shows the

emission wavelength and the corresponding photoluminescence (PL) peak intensities of selected ZAIS QDs under UV irradiation (λ_{ex}=365 nm). This data analysis not only provides the key characteristic properties for the various compositions, but it can also facilitate the selection of ZAIS QDs with appropriate physicochemical properties for further studies and applications. For example, examining the 3D heat map, it is evident that ZAIS QDs without zinc (i.e. $Ag_yIn_{1-y}S_2$) had the longest emission wavelengths (Figure 2.2B). We also observed that the PL peak wavelength was blue-shifted on increasing the Zn concentration. Furthermore, QDs obtained with 0.5 mol Ag and 0.5 mol In, had the longest emission wavelength (λ_{em}=697nm), with an observed blue-shift on increasing or decreasing the Ag concentration. Thus, the emission profiles of the ZAIS QDs could be easily tuned by varying the Zn or Ag (In = 1-Ag) concentrations and hence the reported method used to synthesize our QD library can allow scientists to investigate the composition-dependent physicochemical properties of QDs of interest.

Physical characterization of the ZAIS QDs

In order to ensure the quality of the ZAIS QDs obtained via the sonochemical method, we performed comprehensive characterization of the ZAIS QDs using several different methods (Figure 2.3). The elemental composition of one representative ZAIS QD (Zn_0S-$Ag_{0.2}In_{0.8}S_2$) was analyzed using X-Ray fluorescence spectroscopy (XRF). It was observed that the relative atomic ratios of the constituent elements was consistent with the calculated mole ratios (Figure 2.3A), thus confirming the efficiency of the sonochemical synthetic methodology in obtaining QDs with desired chemical compositions.

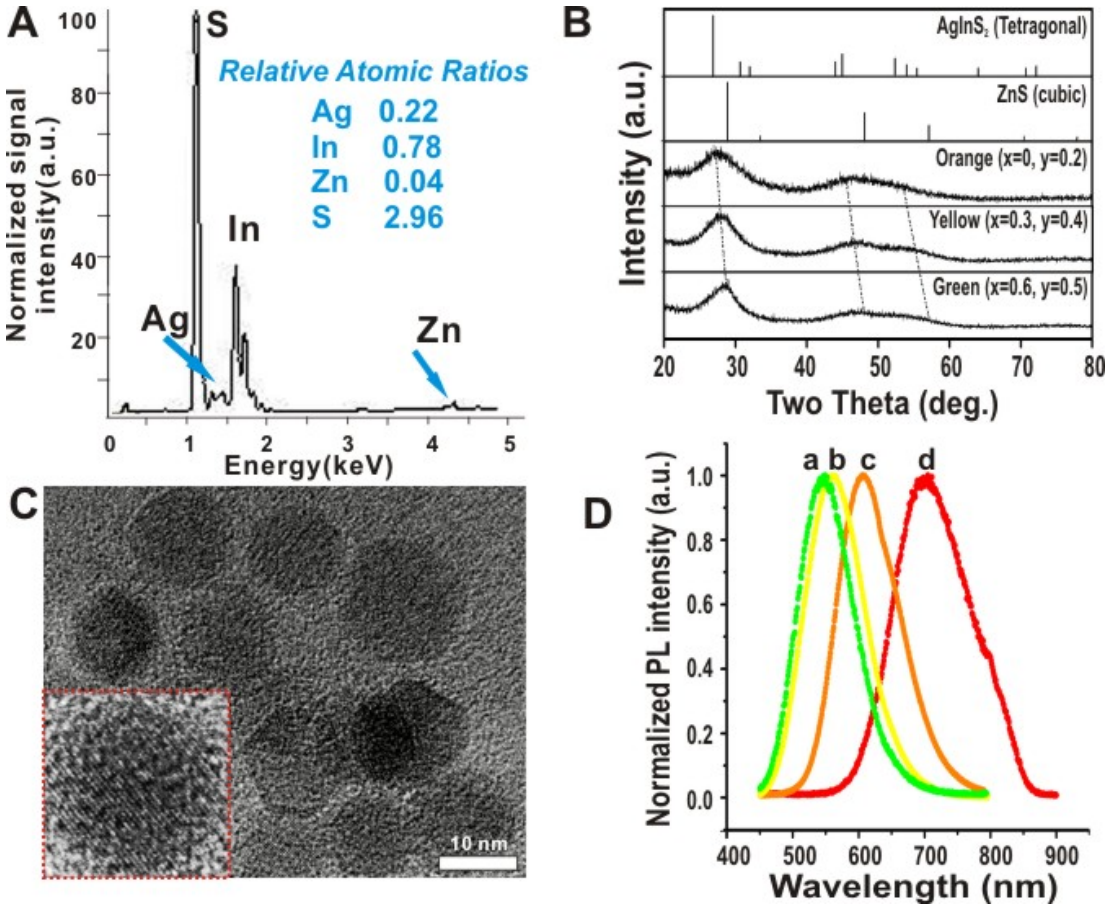

Figure 2.3: Physical characterization of the Zn_xS-$Ag_yIn_{1-y}S_2$ QDs. (A) X-ray Fluorescence analysis of one of the ZAIS QD (x=0, y=0.2) showing the elemental composition and relative atomic mole ratios of the constituent elements. The composition agrees to that calculated theoretically. (B) X-ray diffraction patterns of the ZAIS QDs prepared using sonochemistry. The values of x and y are indicated in the figure. Reference patterns of bulk ZnS and $AgInS_2$ are also shown. Broad peak width is attributed to the amorphous nature of the ZAIS QDs. (C) TEM images of one of the ZAIS QDs (x=0, y=0.2) clearly shows the monodispersity and narrow size distribution (n=100). Inset shows the high resolution image of a single nanoparticle (Scale bar = 10 nm). (D) Photoluminescence spectra of select water-soluble ZAIS QDs (a: x=0.6, y=0.5.; b: x=0.3, y=0.4; c: x=0, y=0.2; d: x=0, y=0.5). Reprinted with permission from [107]

We also analyzed the crystal structures of several compositions of the ZAIS QDs using powder X-ray diffraction (XRD). The particles prepared with varying mole ratios of Zn, Ag and In exhibited three broad peaks which lie in between the diffraction patterns of the tetragonal $AgInS_2$ and bulk cubic ZnS crystals (Figure 2.3B). Furthermore, there was a clear peak shift towards a higher angle with an increase in the amount of Zn_{2+}, thus indicating that the QDs obtained were not just a mixture of bulk ZnS

and $AgInS_2$ but a ZnS-$AgInS_2$ solid solution [77]. Transmission electron microscopy (TEM) analysis clearly revealed the spherical shape and monodispersity of our ZAIS QDs (Figure 2.3C). The average size of the QDs as determined by TEM was found to be 12±1.3 nm. This was further confirmed by measuring the hydrodynamic size and the polydispersity index (PDI) of the ZAIS QDs using dynamic light scattering (Figure 2.4). Additionally, the size of the QDs did not significantly change when their composition was altered.

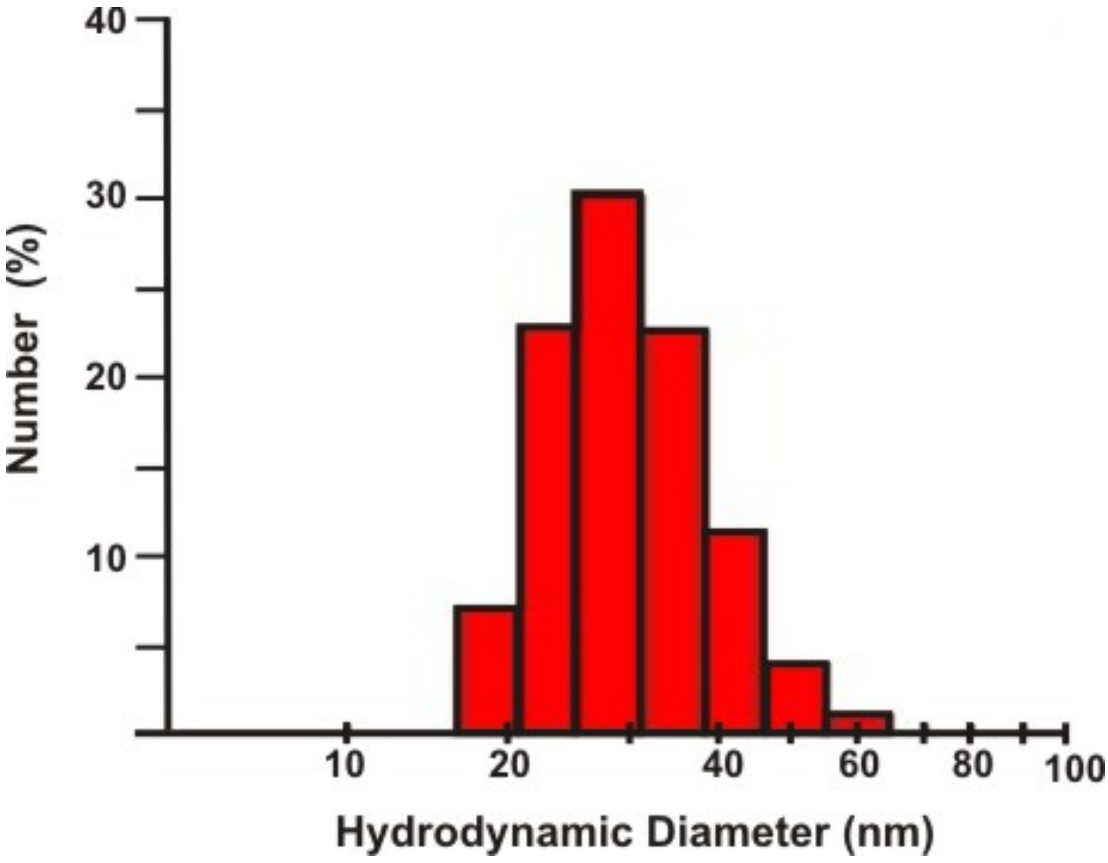

Figure 2.4: Size distribution of the ZAIS QD ($Zn_0SAg_{0.2}In_{0.8}S_2$) as determined by dynamic light scattering. The average size of the QDs in water was around 30nm with a polydispersity index (PDI) value of 0.302 suggesting that the ZAIS QDs were quite monodisperse. Reprinted with permission from [107].

Sample No.	ZAIS QD composition	Emission Wavelength (nm)	Quantum Yield relative to CdSe/ZnS QD (%)
1	Zn_0S-$Ag_{0.5}In_{0.5}S_2$	720	57.6
2	Zn_0S-$Ag_{0.2}In_{0.8}S_2$	606	336
3	Zn_0S-$Ag_{0.5}In_{0.5}S_2$	538	241

Figure 2.5: PL quantum yield (QY) measurements of the ZAIS QDs as compared CdSe/ZnS QDs. QYs of the ZAIS QD solutions were determined by comparing the integrated emission from the nanocrystals to Rhodamine B and Rhodamine-6G dye solutions of matched absorbances. Samples were diluted so that they were optically thin. The QY values are reported as percentge values relative to the CdSe/ZnS quantum yield which was found to have a value of 0.4. Reprinted with permission from [107].

We also determined the PL quantum yields of the ZAIS QDs and compared them to the quantum yield of the CdSe/ZnS QDs (∼0.4). It was found that the relative quantum yields of the ZAIS QDs depended on their composition and were comparable or in some cases higher than that of the CdSe/ZnS QDs (Figure 2.5). Finally, in terms of stability, the physical properties of the ZAIS QDs such as absorption and photoluminescence remained unchanged for two months when stored at ambient conditions (Figure 2.6). Hence, these ZAIS QDs could be potentially used for long term cellular labeling without any loss of photoluminescence.

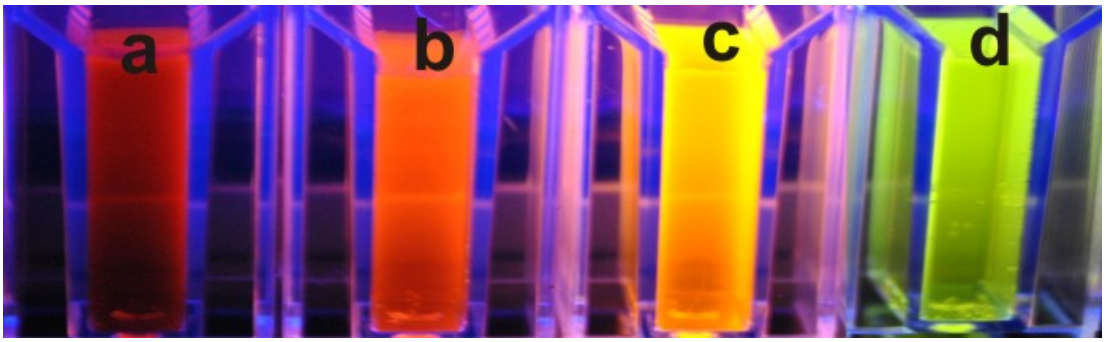

Figure 2.6: Fluorescence image of the ZAIS QDs depicting the PL stability of the QDs after 2 months of storage. (a) Zn_0S-$Ag_{0.5}In_{0.5}S_2$ (b) Zn_0S-$Ag_{0.2}In_{0.8}S_2$ (c) $Zn_{0.3}S$-$Ag_{0.4}In_{0.6}S_2$ and (d) $Zn_{0.6}S$-$Ag_{0.5}In_{0.5}S_2$. Reprinted with permission from [107].

ZAIS QDs as biocompatible and non-toxic molecular imaging probes

The solubility and stability of QDs in an aqueous solution is essential for their wide application as molecular probes in molecular cell biology. In order to be biocompatible, the ZAIS QDs need to be rendered soluble in aqueous physiological conditions, which would exclude the use of any kind of toxic solvents for future biological applications. The ZAIS QDs reported here were functionalized with 3-mercaptopropionic acid (MPA) to render them soluble in physiological conditions [200, 201]. These water-soluble ZAIS QDs were found to be extremely stable at physiological conditions without any signs of aggregation, even when stored for several months (Figure 2.7A). This was further confirmed by monitoring the PL intensity of one of the ZAIS QDs (x=0, y=0.2) in phosphate buffered saline (PBS, pH=7.4) at 37°C over a period of 6 days. The ZAIS QDs were found to be quite stable without any significant loss of photoluminescence over the test period (Figure 2.7B).

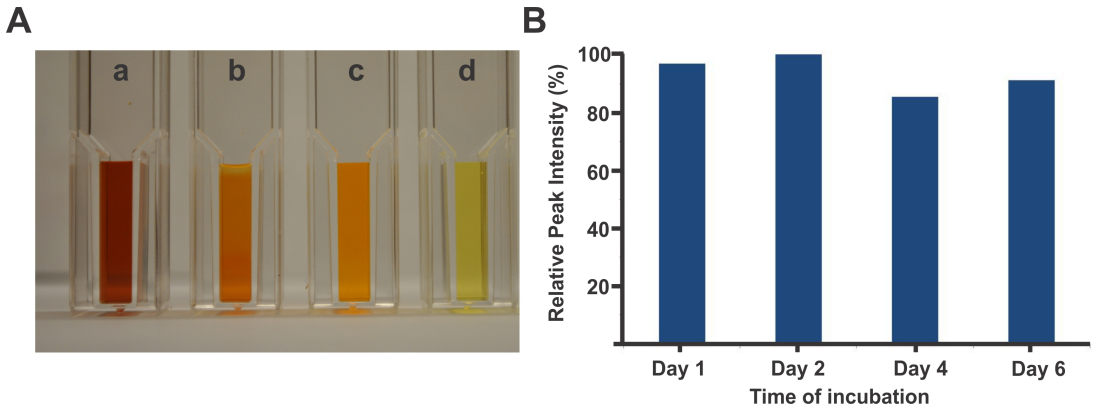

Figure 2.7: (A) Image depicting the colloidal stability of the MPA-coated ZAIS QDs at physiological conditions. (a) Zn_0S-$Ag_{0.5}In_{0.5}S_2$ (b) Zn_0S-$Ag_{0.2}In_{0.8}S_2$ (c) $Zn_{0.3}S$-$Ag_{0.4}In_{0.6}S_2$ and (d) $Zn_{0.6}S$-$Ag_{0.5}In_{0.5}S_2$. The image shows that the water-soluble ZAIS QDs were very stable at physiological conditions (in PBS buffer, pH=7.4), without any sign of aggregation even after several months of storage. (B) PL stability of ZAIS QD in PBS buffer at 37°C. The PL stability of the MPA-coated Zn_0S-$Ag_{0.2}In_{0.8}S_2$ QDs was tested in phosphate buffered saline (PBS, pH=7.4) at 37°C over period of 6 days. The PL peak intensities are reported as percentages relative to that on Day 0. Reprinted with permission from [107].

Another critical factor limiting the use of conventional QDs for various biological

applications is their inherent cellular toxicity [202–205]. This could be partially attributed to the lack of suitable methods to generate QDs with different compositions in a high throughput manner for subsequent toxicological screening. Hence, the generation of a QD library and assaying their cytotoxity in a simple and quick way can facilitate the selection of appropriate QDs eliciting minimum toxic effects and thus enabling the long term cellular imaging of cancer and stem cells *in vitro* and *in vivo*. To test the biocompatibility of our ZAIS QDs for use as imaging probes *in vitro*, a cytotoxicity assay was carried out in both cancer and stem cells (Figure 2.8A).

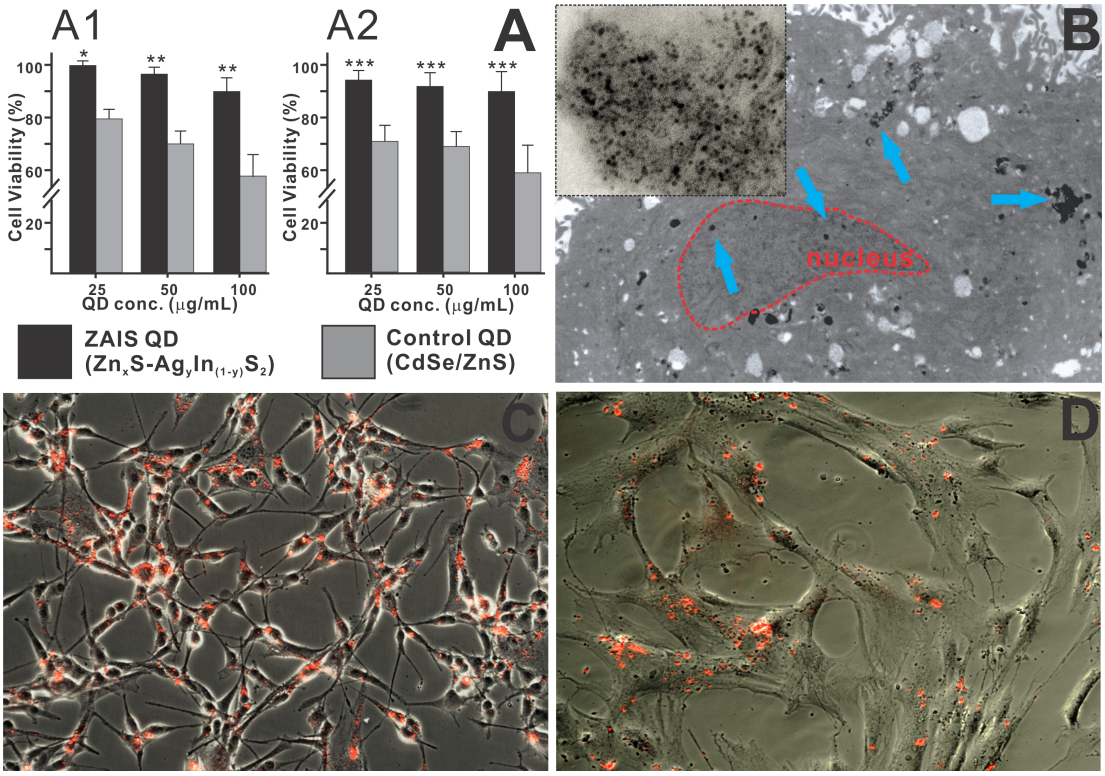

Figure 2.8: Biocompatibility and cellular imaging studies of ZAIS-QDs in mammalian cells. (A) Comparison of the cellular cytotoxicity of the water soluble ZAIS QD (Zn_0S-$Ag_{0.2}In_{0.8}S_2$) and CdSe/ZnS QDs at different concentrations in U87 cells (A1) and hMSCs (A2). The results are presented as means ±SD from three independent experiments. Students unpaired t-test was used for evaluating the statistical significance of the cytotoxicity of ZAIS QDs (*= P<0.001, ** = P<0.01, *** = P<0.05) as compared to the CdSe/ZnS QDs (B) Transmission electron microscopy of the ZAIS QD in hMSCs. The image clearly shows the presence of the QDs (marked by blue arrows) in the cytoplasm and the nucleus (marked in red). The inset depicting the magnified image of the QD cluster, confirms the monodisperse nature of the QDs inside the cell. (C) and (D) Fluorescence microscopy imaging demonstrating the uptake of the water soluble ZAIS-QD (λ_{em}=606 nm) in U87 cells (C) and hMSCs (D). Reprinted with permission from [107].

The concentration-dependent cytotoxicity of the water-soluble ZAIS QDs was assessed in human bone marrow-derived mesenchymal stem cells (hMSCs) and human brain tumor cells (U87 glioblastoma cell line) for two days using a cell proliferation assay (MTS). The toxicity of the ZAIS QDs was also compared to the water-soluble CdSe/ZnS QDs (control sample). The ZAIS QDs showed significantly improved biocompatibility (less cytotoxic, 95% cell viability) in both U87 cells and hMSCs even at high concentrations (upto 100 μg/mL) in comparison to the control sample (CdSe/ZnS

QDs), which were found to noticeably cytotoxic at even low concentrations. In addition, we carried out the cytotoxicity assay of the ZAIS QDs in normal healthy cells (NIH-3T3 mouse fibroblasts). The ZAIS QDs were found to be extremely biocompatible as compared to the CdSe/ZnS QDs (Figure 2.9).

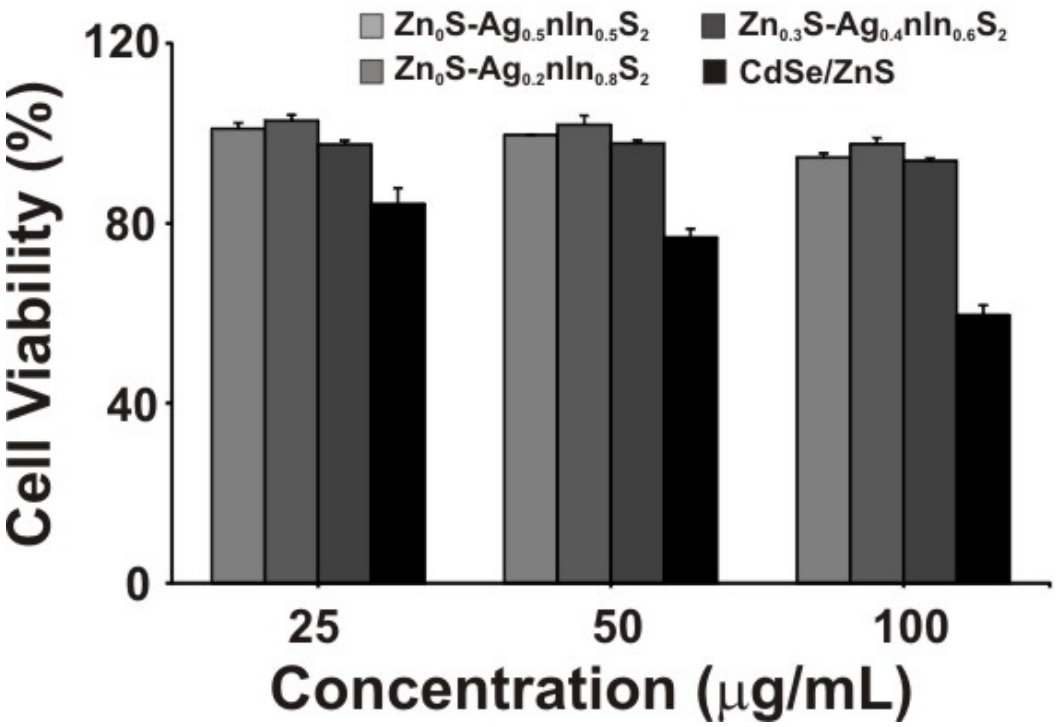

Figure 2.9: Cellular cytotoxicity of select ZAIS QD compositions in normal (NIH-3T3 mouse fibroblasts) cells. The QD composition is indicated in the figure. The results are presented as means±SD from three separate experiments. Reprinted with permission from [107].

The prolonged exposure of nanoparticles, especially QDs, to an oxidative environment (aerial oxidation or UV-induced oxidation) has been known to catalyse their decomposition, thereby leading to the leaching of the metal ions, which is known to induce cytotoxic effects in cells. In order to test the cytotoxicity of our ZAIS QDs under an oxidative environment, we subjected the ZAIS QDs to high-intensity UV light to catalyze the oxidation process. The water-soluble ZAIS QD solutions were exposed to a UV-light source (λ_{em}=365 nm, power density of 12 mW/cm^2) for 1 - 4 hours after which they were incubated with U87 cells. It was found that even after 4h of UV-induced photo-oxidation, the ZAIS QDs were not toxic to the cells (>85% viability, Figure 2.10)

which is in stark contrast to the photo-toxicity of CdSe/ZnS QDs reported previously.

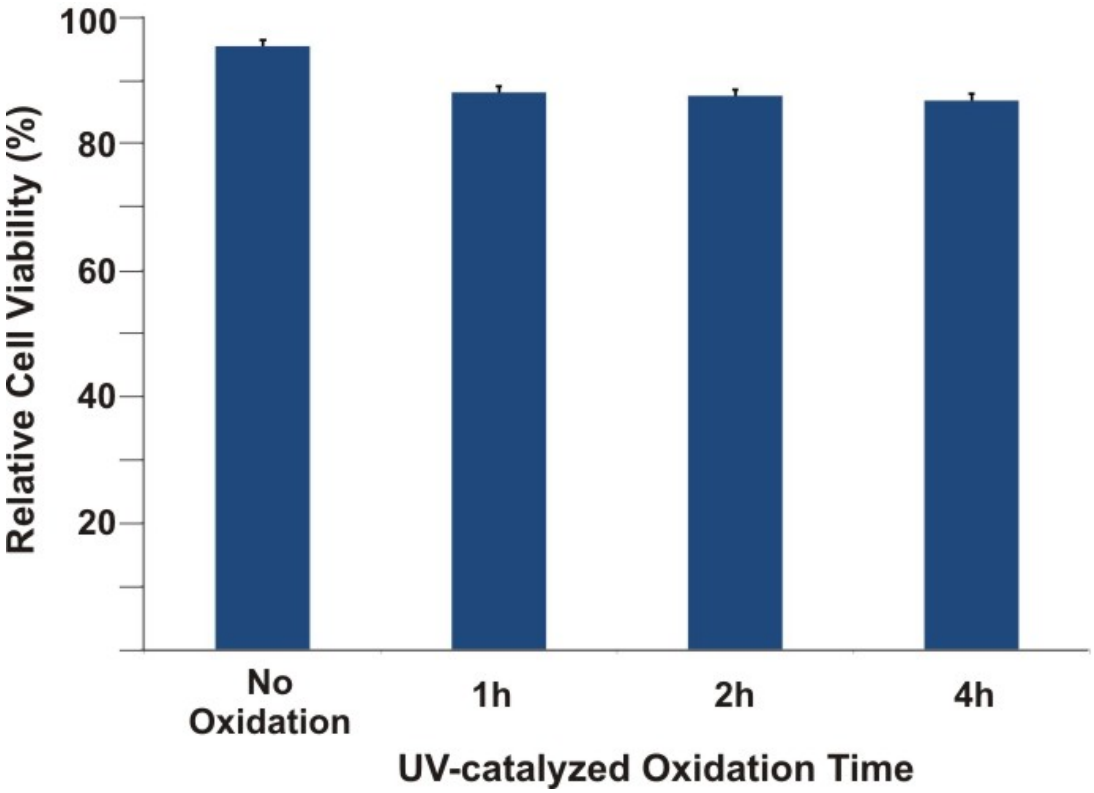

Figure 2.10: Cellular cytotoxicity of water-soluble ZAIS QD in an oxidative environment. The effect of oxidation, induced by high-energy UV irradiation, on the toxicity of select water soluble ZAIS QD (x=0, y=0.2) was tested in U87 glioblastoma cells. The ZAIS QD solutions (200 μg/mL) were found to be non-toxic even after 4 hours of UV-catalyzed surface oxidation. The viabilities were normalized to non-treated controls (No UV and no QDs). The results are presented as means±SD from three separate experiments. Reprinted with permission from [107].

For our cellular imaging experiment, Figure 2.8B shows the internalization of the water-soluble ZAIS QDs (with 606 nm emission) in human MSCs. The QDs were primarily found to be present in the cytoplasm of the hMSCs with a few QDs being found in the nucleus of the cells. Furthermore, fluorescent microscopy images of U87 cells (Figure 2.8C) and hMSCs (Figure 2.8D) incubated with the water soluble ZAIS-QDs proved that the QDs showed strong fluorescence even when inside the cells. Collectively, our ZAIS-QDs showed excellent biocompatibility (non-toxic) and these results can be extended to their wide use in cellular imaging and delivery applications, especially for stem cells, which are known to be extremely sensitive towards nanomaterials.

ZAIS QDs for simultaneous imaging and delivery of siRNA

Having demonstrated the potential of our ZAIS QDs as non-toxic fluorescent imaging probes, we evaluated their ability to be used as vehicles for the efficient delivery and tracking of siRNA in vitro. In the past decade, there has been a considerable interest in the development of nanomaterial-based siRNA and gene delivery methods for controlling cell fate and behavior [206–209]. RNA interference (RNAi) involves the use of small interfering RNAs (siRNAs) to selectively mediate the cleavage of complementary mRNA sequences and thus regulate target gene expression. In combination with other modalities like small molecules and peptides, RNAi could prove to be a powerful tool to manipulate the cellular microenvironments [207]. To harness the full potential of this approach, the prime requirements are to deliver the siRNA molecules with high selectivity and efficiency into tumor cells and to monitor both siRNA delivery and the resulting knock-down effects at the single cell level. Although several approaches such as polymer- and nanomaterial-based methods have been attempted [210–212], limited success has been achieved for delivering siRNA into the target tumor cells.

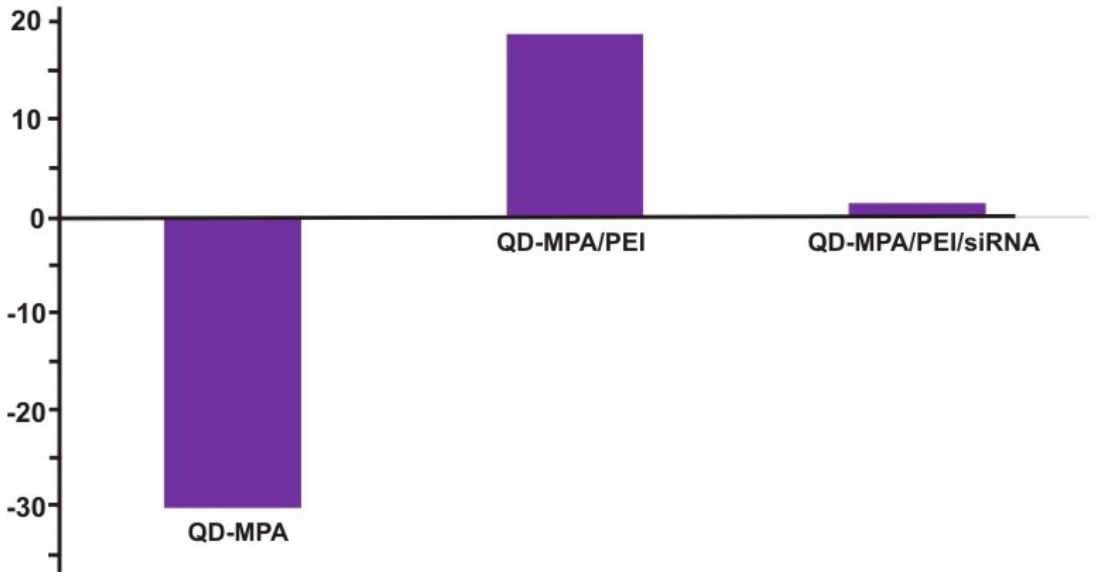

Figure 2.11: Zeta potential measurements of ZAIS QD-MPA-PEI-siRNA to ensure appropriate layer-by-layer coating. The zeta potential value increased from -30.1 mV to 18.9 mv after the coating of a single layer of PEI on the MPA-coated ZAIS QDs. Upon complexation of negatively charged siRNA molecules, the zeta potential value dropped to 1.4 mv. Since the zeta potential was still positive after complexation of siRNA, coating with a second layer of PEI was avoided. Reprinted with permission from [107].

In this context, the use of QDs as a multimodal delivery vehicle becomes a promising choice, thereby allowing for the efficient delivery of siRNA and real-time tracking of the siRNA-mediated gene knockdown [192]. As a proof-of-concept experiment, we used a brain tumor cell line (U87) which was genetically labeled to express the green fluorescent protein (GFP). In order to deliver the siRNA to target brain tumor cells expressing EGFP (U87-EGFP), the MPA-coated ZAIS QDs were conjugated to the siRNA (against the EGFP gene) using polyethyleneimine (PEI) as a cationic polymer via a layer-by-layer approach (Figure 2.1B) [213]. The efficiency of the PEI coating and siRNA conjugation was monitored using zeta potential (Figure 2.11). The decrease in the green fluorescence due to the siRNA-mediated knockdown of the EGFP gene using our ZAIS QD-siRNA constructs was then monitored (Figure 2.12) in order to to assess the transfection efficiency and RNAi activity. It was found that the ZAIS QD-siRNA constructs were efficiently taken up by cells as evident by the intracellular

red fluorescence of the QDs. In addition, the QD localization correlated well with the decrease of the green fluorescence (∼80 % after 3 days of transfection) resulting from the siRNA-mediated knockdown of the EGFP mRNA. These results show the ability of our ZAIS QDs to efficiently translocate siRNA into the cells and achieve gene knockdown in vitro.

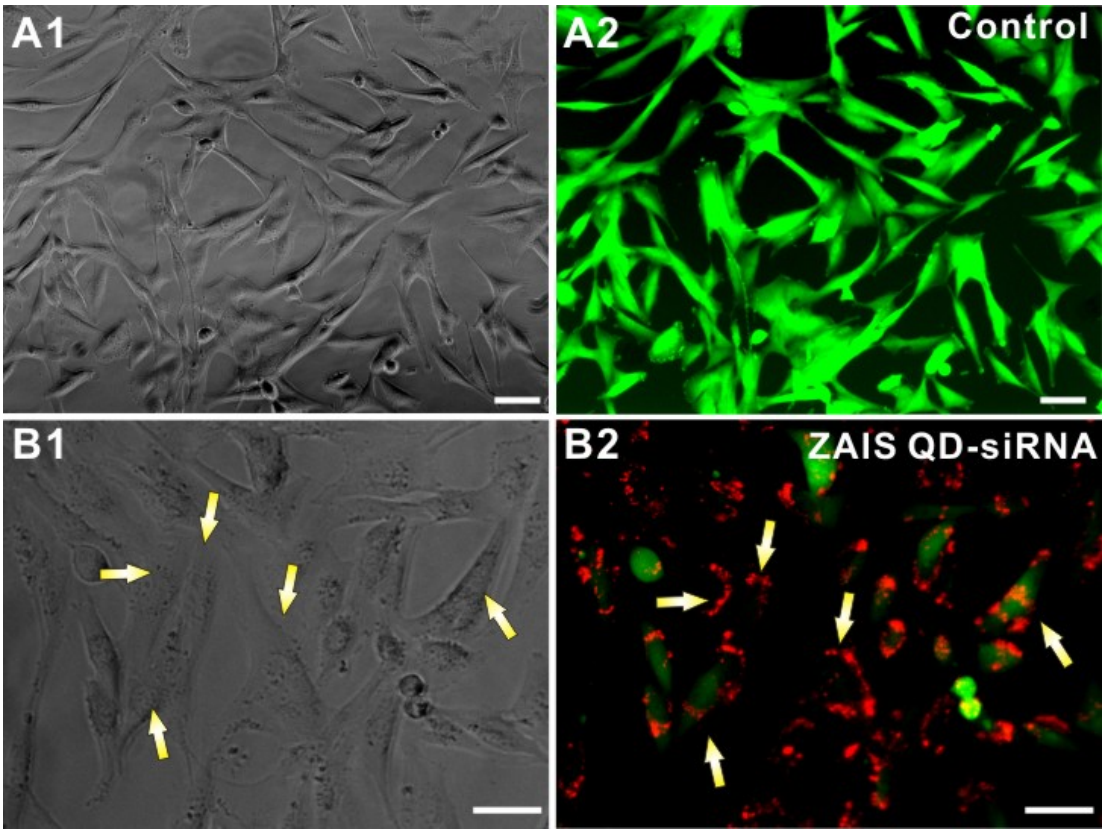

Figure 2.12: *In vitro* testing of the ZAIS-QD-siEGFP cell uptake and silencing efficiency in stably transfected U87-EGFP glioblastoma cells. (A) Control U87-EGFP cells with PEI-coated ZAIS-QD; (A1) represents the phase contrast image and (A2) is the corresponding fluorescence image. (B): EGFP knockdown using the ZAIS QD-siRNA constructs; (B1) Phase contrast image showing the the viability of U87-EGFP cells has not changed appreciably after the transfection of the ZAIS QD-siRNA constructs as compared to the control cells in (A). (B2) Fluorescence image clearly shows the knockdown of EGFP in cells which have internalized the siRNA-QDs (red) after 72 hrs. The red fluorescence from the ZAIS QDs correlates well with the loss of the green fluorescence in cells (indicated by yellow arrows). Scale bar is 50 μm. Reprinted with permission from [107].

With further surface modifications using targeting ligands (RGD, TAT peptides and antibodies) and bifunctional linkers (cleavable or covalent linkers), the ZAIS QDs

could be used for the targeted delivery of siRNA to cancer/stem cells and for the real-time monitoring of its delivery in an efficient manner. In addition, the presence of a library of multicolored QDs obtained via our sonochemical approach, would allow the for multiplexed imaging of transplanted cell populations *in vivo* (i.e., tracking different cell populations with different QDs at the same time).

2.1.3 Conclusions

In summary, this work is a demonstration of the preparation of Zn_xS-$Ag_yIn_{1-y}S_2$ (ZAIS) QDs using a facile sonochemical synthetic method and their application as multifunctional molecular imging probes. Our ZAIS QDs exhibit excellent biocompatibility for the efficient delivery of siRNA and simultaneous imaging/tracking of the same in cancer cells (and stem cells) with negligible QD-induced cytotoxicity. Hence, Our siRNA-QDs could be used for the development of novel chemotherapies and diagnostics relevant to brain cancer research. While the ZAIS QDs show great potential for the imaging and delivery of siRNA *in vitro*, a more thorough investigation of their long-term cytotoxicity is needed before they can be used *in vivo*. Efforts in this direction are underway. Overall, the ease of the synthesis of the ZAIS QDs, their excellent cyto-compatibility and their versatility as multiplexed imaging agents provides an attractive alternative over conventional QD-based molecular imaging probes and siRNA delivery vehicles, and therefore has significant potential for simultaneous prognosis, diagnosis, and therapy.

2.1.4 Materials and Methods

Silver Nitrate ($AgNO_3$, $\geq 99.0\%$), Indium (III) nitrate hydrate ($In(NO_3)_3.xH_2O$, 99.9%, Zinc nitrate hexahydrate ($Zn(NO_3)_2.6H_2O$, Reagent grade), Sodium diethyldithiocarbamate trihydrate ($((C_2H_5)_2NCS_2)Na.3H_2O$, Reagent grade) and Dodecylamine (98%) were purchased from Aldrich. 3-mercaptopropionic acid ($\geq 99.0\%$) was purchased from Fluka. All other solvents were obtained from Fisher and used as received unless otherwise noted.

Synthesis of precursor complexes

5.0 mL of an aqueous solution of sodium diethyldithiocarbamate (0.05 M) was mixed with an aqueous solution containing appropriate amounts of $AgNO_3$, $In(NO_3)_3.xH_2O$ and $Zn(NO_3)_2.6H_2O$ in order to get the required mole ratios (Total concentration of the metal ions was 0.025M). The solution was allowed to stir for 5 minutes after which it was filtered using a Buchner funnel, washed several times with distilled water and MeOH and finally dried in a convection oven at 60°C overnight to obtain the precursor as a dried powder. Several precursor powders were synthesized by varying the mole ratios of the metal salts.

Sonochemical synthesis of dodecylamine-capped ZnS-$AgInS_2$ quantum dots

The precursor complex (0.1 g) and 10.0 mL of dodecylamine were put into a 20 mL vial and sonicated using a tip probe-based high frequency sonicator (Branson Ultrasonics) for 5 minutes in an air-atmosphere. The resulting suspension was allowed to sit at room temperature for two minutes after which 5.0 mL of chloroform and 5.0 mL of MeOH were added to it and centrifuged at 4000 rpm. The supernatant containing the ZAIS QDs was collected and equal amount of MeOH was added to it in order to isolate the nanoparticles. The obtained ZAIS QDs were then resuspended in chloroform for absorbance and photoluminescence measurements.

Surface modification of ZAIS-QDs with 3-mercaptopropionic acid (MPA)

The dodecylamine-capped ZAIS QDs were subjected to a ligand exchange reaction using 3-mercaptopropionic acid (MPA) according to a previously reported protocol [200, 201]. Briefly, a 3.0 mL ethanolic solution of MPA (0.2 M) and KOH (0.3 M) was added dropwise to an equal amount of the dodecylamine-capped ZAIS QD solution in chloroform. The turbid solution was stirred for 3h at room temperature followed by centrifugation at 4000 rpm. The wet precipitate of the MPA-coated ZAIS QDs was washed with EtOH and redissolved in phosphate-buffered saline (PBS, pH=7.4). The water soluble MPA-coated ZAIS QDs were stable in buffer solution with no significant

change in absorption and photoluminescence for upto 2 months, when stored at ambient conditions.

Physical characterization of the ZAIS QDs

The morphology and size distribution of ZAIS QDs was determined using TEM analysis. The water-soluble ZAIS-QDs were drop cast on Holey-carbon grids (Electron Microscopy Sciences), allowed to dry overnight under vacuum and subsequently imaged using a JEOL JEM-2010F high-resolution transmission electron microscope operated at an accelerating voltage of 200 keV. Additionally, the polydispersity index (PDI) and hydrodynamic size of the ZAIS QDs was determined using DLS (Malvern Zetasizer Nano). Powder X-ray diffraction (XRD) analysis was carried out on a Bruker D8 X-ray diffractometer (GmbH, Karlsruhe, Germany) with CuK_{α} radiation to determine the crystallinity of the ZAIS QDs. The powder samples were prepared by drying a chloroform solution of the ZAIS QDs in vacuo. The composition and elemental analysis of the ZAIS QDs was determined using an EDAX Eagle II Micro-EDXRF Spectrometer (EDAX Inc., Mahwah, NJ, USA). UV-Visible absorption spectra were recorded by a Varian Cary 5000 UV-Visible Spectrophotometer. Photoluminescence (PL) spectra were measured using a LS 55 PerkinElmer Luminescence Spectrometer.

Determination of PL stability of ZAIS QDs

A solution of the ZAIS QD (composition of x=0, y=0.2) in PBS (pH=7.4) was incubated at 37°C and the fluorescence intensity was measured over a period of 6 days using a Cary Exclipse Fluorometer (Cary, Varian). The fluorescence intensities were normalized to a Rhodamine B solution in order to account for instrumental and external factors. The fluorescence intensity on Day 0 was taken to be 100%

Culture of human U87 glioblastoma cells, NIH-3T3 mouse fibroblasts and human mesenchymal stem cells

The EGFRvIII overexpressed U87 glioblastoma cells (U87) and human mesenchymal stem cells (hMSCs) were cultured using previously reported methods. For U87-EGFRvIII cells, DMEM (Dulbeccos modified Eagles medium) with high glucose (Invitrogen), 10 % Fetal Bovine Serum (FBS, Gemini Bioproducts), 1 % streptomycin-penicillin and 1% glutamax (Invitrogen, Carlsbad, CA) were used as basic components of growth media including Hygromycin B (30 μg/ml, Invitrogen) as a selection marker. Human bone marrow-derived MSCs (Lonza, Walkerville) were cultured in the conditioned media (Lonza, Walkerville) according to manufacturers recommendations. For the NIH-3T3 mouse fibroblasts, DMEM (with high glucose) supplemented with 10 % Fetal Bovine Serum (FBS, Gemini Bioproducts), 1 % streptomycin-penicillin and 1% glutamax (Invitrogen, Carlsbad, CA) was used as the growth medium. All cells were maintained at 37°C in humidified 5% CO2 atmosphere.

Cell viability assays

The cellular viability of the U87, 3T3 cells and hMSCs loaded with the ZAIS QDs was assessed using the standard 3-(4,5-dimethylthiazol-2-yl)-5-(3-carboxymethoxyphenyl)-2-(4-sulfophenyl)-2H-tetrazolium (MTS) assay. NIH-3T3 cells, U87-EGFRvIII and hMSCs were seeded in a 48-well plate and grown to 70-80 % confluency. Various compositions of the ZAIS QDs were mixed with 2.0 L each of XtremeGene transfection reagent (Roche, USA) to get final concentrations of 25, 50 and 75 μg/mL of the ZAIS QDs. The cells were incubated with these complexes at 37°C in a humidified and 5% CO2 atmosphere for 6 h, after which they were washed twice with PBS and the media replaced in the transfected wells. Cells treated with only XtemeGene reagent were used as a control. The transfected cells were allowed to grow for 48h, after which the cell viability was assessed using the CellTiter 96 AQueous One Solution Cell Proliferation Assay (Promega, Madison, USA) according to the manufacturers recommended protocol.

Cellular imaging using fluorescence microscopy

U87 and hMSCs were seeded in a 24-well plate, incubated at 37C in a humidified and 5% CO2 atmosphere. After 24 hours, water-soluble MPA-coated ZAIS QD (composition of x=0, y=0.2, Emission of 606 nm) complexed with 2 μL of XtremeGene transfection reagent (at a final concentration of 50 μg/mL QDs) was added to each of the wells. The cells were incubated with the QD complex for 6 hours after with the media was replaced. The cells were then allowed to grow for another 24 hours at the same conditions, after which the cells were fixed using 10% Formalin and images were taken using a Nikon Ti-Eclipsed Inverted Fluorescence microscope (Nikon Instruments, USA). Each image was captured with different channels and focus. Images were processed and overlapped using the NIS-Elements software (Nikon, USA).

Cellular transmission electron microscopy

U87-EGFRvIII cells and hMSCs were seeded in a 6 cm dish (BD Falcon, USA) and allowed to grow till 70% confluency. The cells were then treated with above mentioned MPA-coated ZAIS QD-XtremeGene complexes (at a final concentration of 50 μg/mL of QDs) for 6h after which they were washed and the media replaced in the dish. The cells were allowed to grow to 90% confluency after which they were trypsinized and subsequently fixed using Trumps Fixative (Electron Microscopy Sciences, Hatfield, PA, USA) for 2h. The cells were washed twice with sodium cacodylate buffer (pH=7.4, EM Sciences, PA, USA) and post-fixed with 1% aqueous Osmium Tetroxide (Acros Organics, USA) for 1 h. The cells were dehydrated using a graded ethanol washing (50%, 75%, 80%, 95% and 100%) and finally embedded in epoxy resin using the Low Viscosity Spurrs Kit (Electron Microscopy Sciences, Hatfield, PA) according to manufacturers recommended protocol. The cells were then imaged using a using a JEOL 100CX TEM instrument operating at 80 keV accelerating voltage.

Attachment of siRNA to the MPA-coated ZAIS QDs

For the siRNA to silence EGFP gene in U87-EGFP cells, we utilized the layer-by-layer (LbL) method with slight modifications to the reported procedure [213]. Polyethyleneimine (PEI, MW 10,000) in distilled water was added to MPA-coated ZAIS QDs (composition of x=0, y=0.2, Emission of 606 nm, 400 μl, 10 mg/mL) at a final concentration of 1.0 mg/mL. After sonication for 2-4 hours under neutral pH, the coated particles were purified using ultracentrifugation and subsequent washing with distilled water. After characterization of the surface charge using zeta potential measurement, 100 nmol siRNA solution (Integrated DNA Technologies Inc., IA, USA) in PBS was added to 300 μl of PEI coated ZAIS-QD solution (50 μg/ml). After mild stirring for 1-2 hours, the final product was purified by ultracentrifugation (14,000 rpm) and washed with 1.0 mM NaCl solution. Surface charge was characterized using zeta potential measurement (Zetasizer Nano ZS, Malvern Instruments, Westborough, MA) to perform the siRNA transfection experiment.

Culture of human U87-EGFP cells for siRNA knockdown experiments

The EGFP overexpressed U87 glioblastoma cells (U87-EGFP) were cultured using DMEM with high glucose, 10% fetal bovine serum (FBS, Gemini Bioproducts), 1% Streptomycin-penicillin and 1% Glutamax (Invitrogen, Carlsbad, CA). Geneticin G418 (100 μg/ml, Invitrogen) was used as a selection marker for the U87-EGFP cells. All cells were maintained at 37°C in humidified 5% CO2 atmosphere. For the knockdown experiments, 10^4 cells were grown to 50-60% confluency in a 48-well plate. The ZAIS QD-MPA-PEI-siRNA conjugates were dispersed in the transfection media (Opti-MEM) at a final concentration of 50 μg/ml. 100 μl of the nanoparticle solution was added to the U87-EGFP cells. U87-EGFP cells treated with only PEI-coated ZAIS QDs were used as a control. After 6 hours of incubation, the solution in each well was removed and exchanged with the growth medium. The cells were allowed to grow for 72 hours after which the GFP knockdown and QD localization was assessed using fluorescence microscopy (Nikon Ti-Eclipsed Inverted Fluorescence microscope, Nikon Instruments,

USA). Each image was captured with different channels and focus. Images were processed and overlapped using the NIS-Elements software (Nikon, USA).

Cytotoxicity assessment of ZAIS QDs in oxidative environment

200 μg/ml solutions of the ZAIS QD (composition of x=0, y=0.2, Emission of 606 nm) in PBS were placed under a longwave (365 nm) UV lamp for 1, 2 and 4 hours. The spherical irradiation was 12 mW/cm^2 as determined with a radiometer. The photo-oxidized ZAIS QDs were then incubated with U87-EGFRvIII cells (104 cells seeded in a 48-well plate and grown to 70% confluency) for 48 h, after which the cell viability was assessed using the CellTiter 96 AQueous One Solution Cell Proliferation Assay (Promega, Madison, USA) according to the manufacturers recommended protocol.

Chapter 3

Nanomaterials for Drug Delivery and Effective Cancer Therapy

In previous chapter, we developed novel nanomaterial-based advanced molecular imaging and diagnostic probes for imaging of cancer and stem cells. In this chapter we will see the application of nanotechnology for the purpose of drug delivery and in particular, for the delivery of multiple anticancer therapeutics and siRNA into brain cancer. Glioblastoma multiforme (GBM) or brain cancer is the most malignant, invasive, and difficult-to-treat primary brain tumor. Successful treatment of GBM is rare with a mean survival of only 10-12 months [214, 215]. In this section, we will then see the synergistic effects of different drugs on increasing tte apoptosis of brain cancer cells by the down regulation of key oncogenic signaling pathways. Finally, we will see the emerging impact of novel nanomaterials in cancer biology and how they can circumvent the current issues in brain cancer treatment from a clinical viewpoint.

3.1 Dendritic Polypeptide-based Nanocarrier for the Delivery of Multiple Anticancer Drugs and siRNA to Brain Tumor Cells

3.1.1 Introduction

Advances in the field of chemical genetics and molecular cell biology have triggered a surge in development of genetic manipulation based therapies for cancer [216,217]. Such genetic manipulation methods typically rely on either the traditional small molecule/ protein modalities [218] or the newly discovered RNA interference (RNAi) based modalities [219], each having their own advantages and disadvantages. For example, RNAi therapeutics can provide attractive solutions to the major shortcomings of the conventional therapeutics, including difficulty in lead identification and complex synthesis of small organic molecules and proteins, and potentially can be applicable to all molecular targets for cancer therapy [220]. However, RNAi-based therapeutics, such as small interfering RNA (siRNA) and micro RNA (miRNA), are inherently antagonistic and their downstream effects (i.e., genesilencing) are delayed, compared to those of conventional small molecule/ protein-based therapeutics [221]. Additionally, owing to their short serum half-life and poor cellular uptake, successful clinical application of siRNA requires appropriate chemical modifications and better delivery vehicles to overcome the numerous cellular barriers [219]. On the other hand, small organic molecules can act as both antagonists and agonists for molecular targets and their drug effects can be much faster than siRNA with minimal problems during their intracellular uptake. [220] Hence, from a biological perspective, it would be beneficial to combine the advantages of these therapeutic modalities to potentially enhance their individual efficacy. For example, it was recently demonstrated that simultaneous delivery of siRNA against multidrug resistance genes in cancer cells led to the enhanced efficacy of the codelivered anticancer drugs [222, 223]. These studies show that it would be desirable to target multiple oncogenic signaling elements using different therapeutic modalities for cooperative effect, especially considering the molecular heterogeneity of tumors. In recent years, significant effort has been devoted to develop nanotechnology for drug delivery since it offers a suitable means of delivering small molecular weight drugs, as well as macromolecules

such as proteins, peptides or genes by either localized or targeted delivery to the tissue of interest [224]. Several engineered nanomaterials such as dendrimers, liposomes, and metallic nanoparticles have been developed to deliver anticancer drugs to cancer cells. These systems in general can be used to provide targeted (cellular/tissue) delivery of drugs, to improve bioavailability, to sustain drug/gene effect in target tissue, to solubilize drugs, and to improve the stability of therapeutic agents against enzymatic degradation (nucleases and proteases), especially of protein, peptide, and nucleic acids drugs [224]. However, considering the molecular heterogeinity of cancers, the development of drug delivery systems capable of loading and delivering multiple anticancer therapeutics in order to achieve a synergistic therapeutic effect against aggressive tumors such as brain and breast cancers has been at the forefront [161, 222, 223].

In this regard, the use of polypeptides and dendrimer-based systems have been quite prominent as they are very amenable for the covalent conjugation of multiple small molecule anticancer drugs and also for the complexation of negatively charged therapeutic small interfering RNA (siRNA). For example, dendrimers have unique characteristics including monodispersity, modifiable surface functionality, highly defined size and structure with a very high positive surface charge These attributes allow for the efficient conjugation and delivery of therapeutics like drugs, siRNA, aptamers and plasmid DNA into cells [207, 225, 226]. In addition, the multivalency of dendritic structures further enhances their interaction with the cellular microenvironment, thereby making them prime candidates for drug delivery applications [227]. In the past, dendrimers have been utilized to carry a variety of small molecule pharmaceuticals and nucleic acids (DNA, siRNA and miRNA) to several tumor cells in order to obtain a synergistic response [207]. However, many of the dendrimer-based drug carriers are known to be extremely cytotoxic to cells. Many of the amine-terminated dendrimers bind to negatively charged membranes of cells in a non-specific manner and can cause toxicity *in vitro* and *in vivo*. In this regard, synthetic polypeptides, which are essentially poly-amino acids linked by amide bonds, are biodegradable and biocompatible synthetic polymers with the availability of many side-chain functional groups to conjugate therapeutic molecules. For example, several groups have reported the use of polypeptides for the conjugation

and translocation of therapeutics across the cell membrane. These systems include linear cell penetrating peptides (CPPs) [166–170], chimeric oligopeptides [228, 229] and self-assembling polypeptides [230]. However, most of these delivery vehicles suffer from several limitations such as complex synthetic methods, poor drug loading efficiencies and the inability to conjugate and deliver multiple therapeutic modalities in a controlled manner using a single platform. In addition, owing to the lack of multivalency, linear polypeptide-based drug carriers have met with limited success with the efficient complexation and delivery of siRNA to tumor cells. Thus, it would be highly desirable to combine the multivalency of dendrimers and the biocompatibility of polypeptides into a single platform in order to overcome their respective limitations [231]. Furthermore, since the majority of anticancer drugs used today in the area of polymeric therapeutics are not based on peptide sequences, efficient conjugation to the polymeric carrier is a major requirement when using polypeptides as the carrier. The few reports available of synthetic strategies to conjugate a drug such as doxorubicin to a polypeptide describe in general multi-step synthesis, with high excess of reagents, and moderate efficiency of drug conjugation [228–230]. Moreover, almost all studies have sought to synthesize 1:1 conjugates with one drug molecule bound to one polypeptide, resulting in low drug loading [232]. Therefore, there is a clear need to develop more versatile dendritic peptides that require fewer synthetic steps and offer the possibility of multiple drug conjugation and thus higher drug loading.

Herein we report the synthesis of a dendritic polypeptide-based carrier for the targeted delivery of multiple anticancer drugs and siRNA in order to elicit a synergistic inhibition of brain tumor cell proliferation (Figure 3.1). We hypothesize that a dendritic polypeptide-based drug delivery platform would not only enable the conjugation of multiple anticancer drugs and siRNA, but also allow for their efficient delivery to tumor cells in a controlled manner, thereby leading to a synergistic effect.

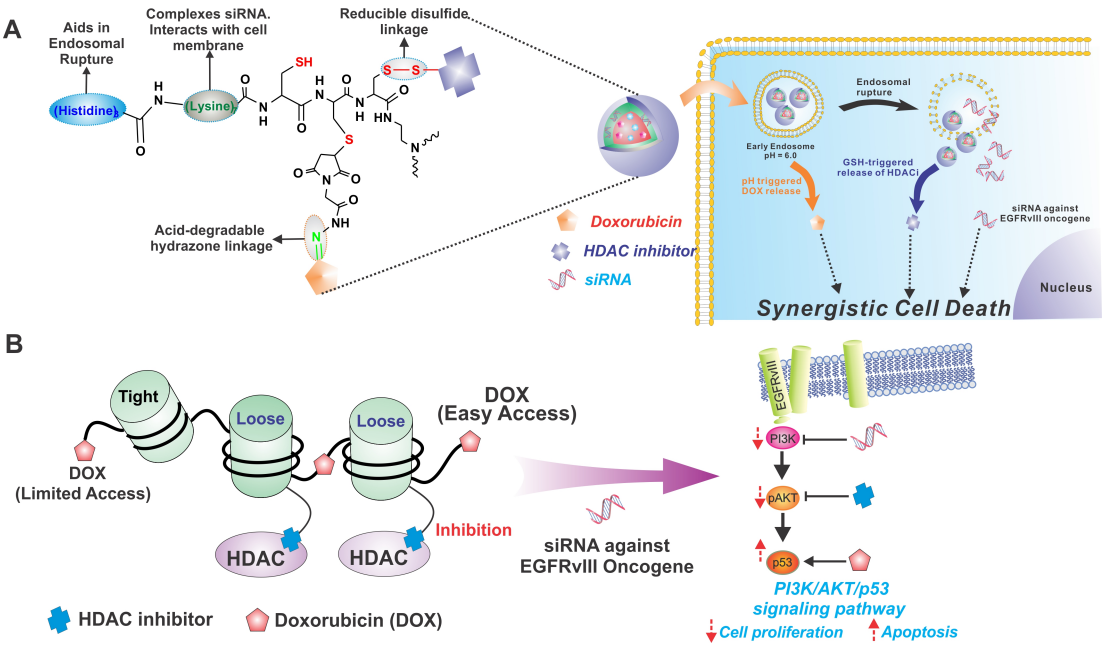

Figure 3.1: Schematic of the dendritic polypeptide for the delivery and stimuli responsive-controlled release of multiple anticancer therapeutics (DOX, HDACi and siRNA) in brain cancer cells for synergistic cell death. The polypeptide backbone contained multiple cysteine residues for the conjugation of DOX and HDACi using an acid-labile hydrazone linkage and disulfide linkage respectively. The lysine residues enabled the complexation of the negatively charged siRNA while terminal histidine residues aided in the endosomal escape of the therapeutics after cellular uptake B) Schematic depicting synergism between DOX and the HDACi, by the down regulation of the PI3K–AKT–p53 signaling pathway. HDACi increases the access of DNA to DOX by opening up the chromatin thereby leading to an increase in its efficacy, which could be further enhanced by the use of siRNA against the EGFRvIII oncogene

3.1.2 Results and Discussion

Synthesis of and characterization of the dendritic polypeptide

In our design, the synthesis of the dendritic polypeptide was accomplished by the ring opening polymerization of N-carboxy anhydrides (NCAs) using a three-armed amine initiator. The use of NCA chemistry for the ring opening process permits control over the structure of the polypeptide chain by the sequential growth of amino acid monomers from the core [233,234]. The structure of the three-armed polypeptide was carefully chosen, wherein i) the three cysteine residues per arm were used to conjugate hydrophobic anticancer drugs, thereby increasing their solubility and cellular uptake, ii) the presence of seven lysine residues on each arm allowed for complexing the negatively charged

small interfering RNA (siRNA) and also improve the transfection efficiency of the drug conjugates into tumor cells and, iii) the three terminal histidine moieties on each arm facilitated the endosomal escape of the polypeptide-drug conjugates once uptaken by the cancer cells. In addition, targeting moieties such as the cyclic-RGD peptide (cRGD) could be easily attached onto the polypeptide backbone, thereby demonstrating the potential for the targeted delivery of these conjugates (Figure 3.1). The NCAs of L-lysine, L-cysteine and L-histidine were synthesized according to previously reported methods, with slight modifications. The polypeptide backbone was synthesized by the ring opening polymerization (ROP) of the corresponding amino acid NCAs prepared previously using a tri-armed amine as the core initiator (Figure 3.2).

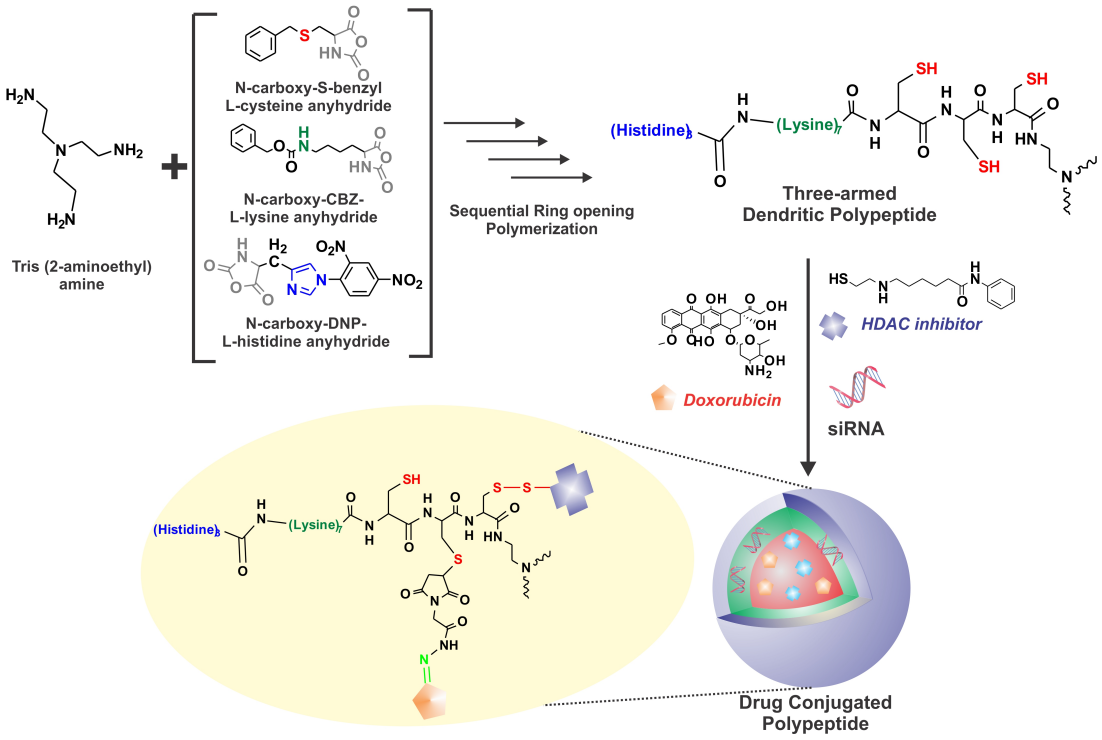

Figure 3.2: Schematic depicting the synthesis of the dendritic polypeptide and subsequent conjugation of DOX, HDACi and siRNA to it. The synthesis of the polypeptide backbone was carried out by the sequential ring opening polymerization using the corresponding amino-acid NCAs and Tris-(aminoethyl) amine as the initiator followed by the conjugation of DOX and HDACi to the cysteine-thiol residues using an acid-labile hydrazone linkage and disulfide linkage respectively. The siRNA was complexed to the lysine residues via electrostatic interaction.

The control of the molecular weight of polypeptides via NCA polymerization (in

a range less than 5 kD) was achieved by choosing a polar solvent and primary amine [Dimethylformamide (DMF) and Tris-(2-aminoethyl)amine respectively in our case]. The structure and purity of the polypeptide was confirmed using ^{1}H NMR spectroscopy. The molecular weight of the polypeptide backbone was further confirmed using MALDI-TOF analysis. The average molecular weight of the polypeptide was found to be 4931 daltons, which was very close to the calculated weight of 4922 daltons (Figure 3.3).

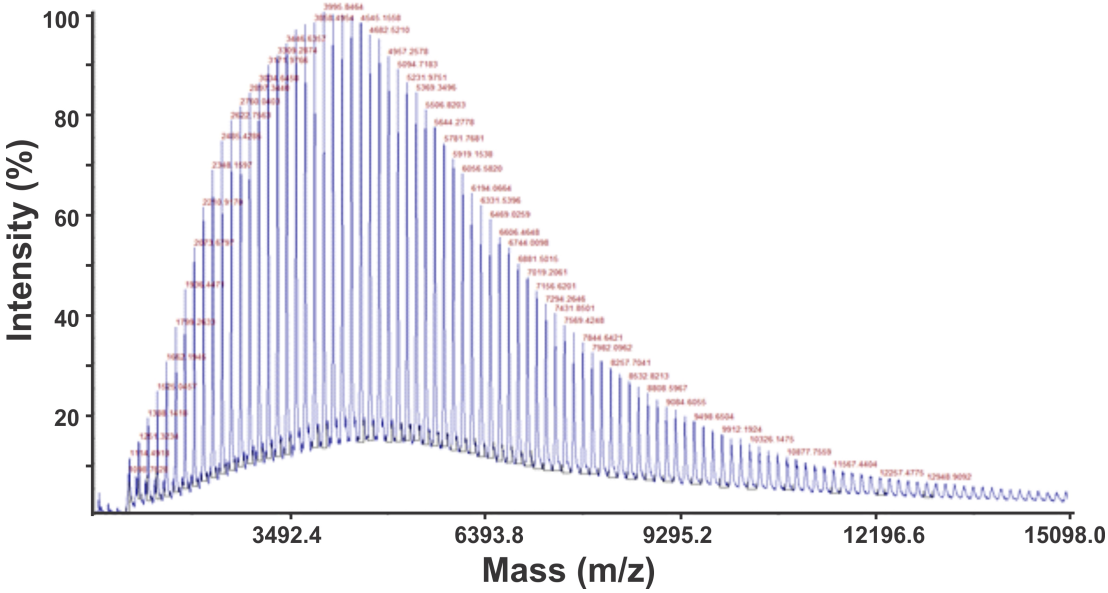

Figure 3.3: Measurement of the molecular weight of the polypeptide. The average molecular weight of the polypeptide was measured using MALDI-TOF analysis using α-Cyano-4-hydroxycinnamic acid (CHCA) as the matrix.The average molecular weight of the peptide was found to be 4931 daltons which agreed well with the calculated molecular weight of 4922 daltons.

The polypeptide was found to be extremely soluble in aqueous solvents at physiological conditions. Collectively, these results prove the efficiency of the NCA-based synthetic method for obtaining the polypeptide with the desired amino acid sequence

Loading multiple anticancer drugs onto the dendritic polypeptide

Having synthesized the dendritic polypeptide carrier with the desired structure (cysteine residues for drug conjugation, lysine residues for cellular translocation and histidine residues for endosomal escape) and aqueous solubility, the next step was to conjugate multiple anticancer drugs onto it in a facile manner. We chose Doxorubicin (DOX)

and a histone deacetylase inhibitor (HDACi) as model drugs for our study. DOX is a widely used chemotherapeutic for the treatment of several aggressive cancers such as head and neck carcinoma, melanoma, brain, breast, ovarian and liver cancer. DOX is known to induce cellular toxicity by the inhibition of topoisomerase II, an enzyme responsible for DNA replication. However, the toxic dose-limiting side effects of DOX, such as cardiotoxicity and nephrotoxicity, result in a narrow therapeutic index [235]. In addition, aggressive tumors such as brain and breast tumors display multiple modes of drug resistance to DOX and other chemotherapeutics, which further limit its therapeutic efficacy. In this regard, the use of HDAC inhibitors, agents which modulate the histone decondensation and hence enhance the unpacking of the chromatin, have emerged as promising candidates for the treatment of cancers [236]. Thus, HDAC inhibitors can act as sensitizing agents for DNA-damaging drugs such as DOX thereby increasing its potency [237–240]. For example, Kim and coworkers reported that the co-delivery of DOX and the FDA approved HDAC inhibitor, suberoylanilide hydroxamic acid (SAHA), potentiated the anticancer activity of DOX in glioblastoma and breast cancer cell lines. It was found that the increased efficacy was due to the increase in the expression level of *p53*, which is a key tumor suppressor gene, often found in lower levels in brain and breast cancers [237]. Even though these studies demonstrate the efficacy of the co-delivery of DOX and HDACi, there are several limitations, which need to be overcome in order to maximize their potential in a clinical setting. The low aqueous solubility of these traditional HDAC inhibitors require the use of solvents such as DMSO for their delivery, which severely limits their therapeutic efficacy in physiological conditions. Additionally, the delivery of these drugs would require their release in a controlled manner inside the cells in order to overcome dose limiting toxicities of the anticancer drugs.

Hence, we hypothesized that the use of our dendritic polypeptide as a delivery vehicle would help in solubilizing these hydrophobic drugs, thereby increasing their uptake and thus leading to a corresponding increase in their potency. In addition, it would also provide a suitable handle for controlling their release inside the cells by physical and/or chemical stimuli (HDACi using reducible disulfide bond and DOX via

acid-cleavable hydrazone linkage). The polypeptide would also aid in the complexation of siRNA against specific oncogenes, which could be used in conjunction with the drugs to further enhance their efficacy. Furthermore, the use of our polypeptide would help in achieving higher drug loading efficiencies as compared to traditional drug delivery systems such as liposomes and self-assembling chimeric polypeptides [228,241]. Towards this end, we synthesized a non-hydroxamate thiol-based SAHA analogue (henceforth referred to as HDACi) in order to attach it onto the polypeptide carrier using a disulfide linkage. The synthesis of the HDACi was achieved according to a previously reported procedure [242]. Doxorubicin was activated by reacting it with β-malemidopropionic hydrazide (BMPH). Activated DOX was immediately used in a second reaction with the polypeptide (2:1 mole ratio DOX:Polypeptide). Following this, the HDACi was attached to the cysteine SH of the DOX-conjugated polypeptide using a disulfide linkage (Figure 3.2).

The hydrodynamic sizes and polydispersity indices (PDI) of the polypeptide-backbone and the drug-conjugated polypeptide were analyzed using dynamic light scattering (DLS). It was found that the polypeptide backbone itself had an average size of $\sim$68 nm (PDI = 0.138), which increased to 95 nm (PDI = 0.3) after drug conjugation (Figure 3.4). The small increase in size can be attributed to the steric repulsions due to the conjugation of the drugs. However, this size is optimum for escaping renal clearance while having sufficient cell uptake via endocytosis. We also measured the zeta potential of the polypeptide before and after the conjugation of the drugs. The polypeptide backbone, owing to the large number of lysine residues, was found to have a high positive charge (as evidenced by the positive zeta potential of 26.0 mV). In addition, there was no appreciable change in the zeta potential after drug conjugation (23.1 mV), which would later facilitate the efficient complexation of siRNA for co-delivery to cancer cells (Figure 3.4).

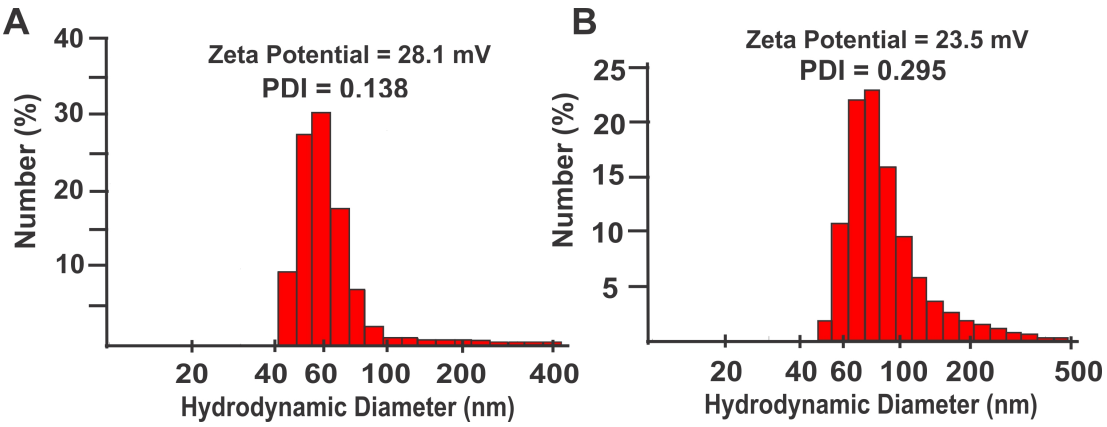

Figure 3.4: Hydrodynamic size and surface charge of the polypeptide-drug conjugates. The hydrodynamic size, zeta potential and polydipersity index (PDI) of the polypeptide only (A) and the polypeptide-DOX-HDACi (B) conjugates were measured using dynamic light scattering. The results are presented as an average of the values obtained from three independent measurements.

We also characterized the drug loading efficiencies of DOX and HDACi on the polypeptide using UV-visible spectroscopy and LC-MS respectively. We could achieve a drug loading efficiency of 94% for DOX and 80% for the HDACi, which is remarkably higher as compared to those reported in literature [228]. This could be attributed to the covalent conjugation of the drugs in our case as opposed to their hydrophobic encapsulation using the self-assembly process often used in the traditional liposomal and polymer-based formulations. Thus, we could load more drug amounts per unit weight of the polypeptide, which would be extremely beneficial for future *in vivo* applications..

Controlled release of DOX and HDACi from polypeptide

Controlled-release systems are designed to enhance drug therapy [243]. There are several motivations for developing controlled-release systems, which may depend on the drug of interest. Controlled release systems have been devised to enable superior control of drug exposure over time, to assist drug in crossing physiological barriers, to shield drug from premature elimination, and to shepherd drug to the desired site of action while minimizing drug exposure elsewhere in the body. A distinction of controlled release is that it not only prolongs action but it attempts to maintain drug levels within the therapeutic window to avoid potentially hazardous peaks in drug concentration

following ingestion or injection and to maximize therapeutic efficiency. Having characterized the physical properties of the polypeptide-drug conjugates, we tested their capability to release the conjugated drugs inside the cells in a controlled manner. The release of drug moeities from the polypeptide backbone requires the pH-dependent cleavage of the hydrazone bond (in case of DOX) and the redox-dependent cleavage of the disulfide bond (in case of HDACi).

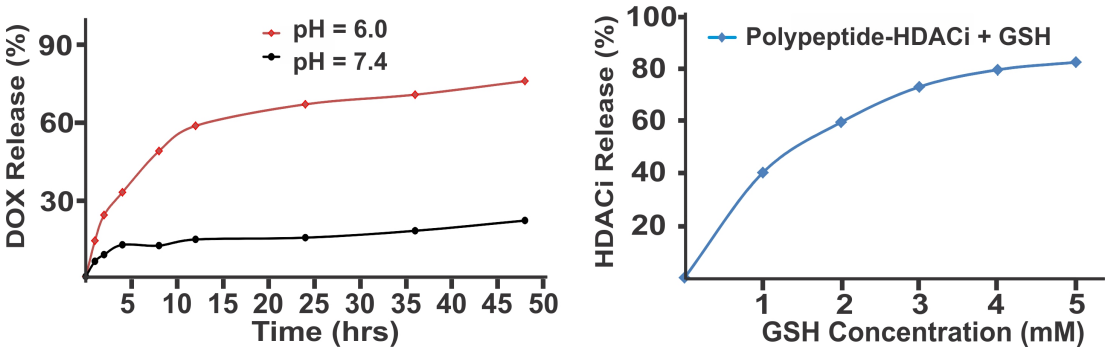

Figure 3.5: Stimuli-sensitive controlled release of the DOX and HDACi from the polypeptide. (A) Cumulative release profile of DOX from drug conjugated polypeptide at pH=7.4 and pH=6.0 using UV-Vis spectroscopy (B) Release profile of HDACi from the polypeptide as a function of GSH concentration using LC-MS.

To verify the kinetics of DOX release, the drug-conjugated polypeptide was incubated at pH=7.4 and pH=6.0 at 37°C for 48 h. The fraction of the DOX released over a period of 48 hours was determined by monitoring the absorbance peak at 495 nm using UV-Visible spectroscopy. At pH 7.4, the hydrazone bond was stable, with only minimal DOX release (22%) over a period of 48 hours. On the other hand, at pH 6.0, free DOX was gradually released and reached a maximum amount of 75.4% of the initial amount of DOX (Figure 3.5A), which was similar to the levels observed with other polymeric hydrazones [243]. In a similar fashion, the release of the HDACi was determined by incubating the drug-conjugated polypeptide with increasing concentrations of glutathione (GSH) and monitoring its release using LC-MS. GSH is an enzyme found inside cells which mediates the cleavage of disulfide bonds of cellular proteins. It was found that the release of the HDACi increased as the concentration of GSH was increased from 0 to 5 mM, with a maximum release of 40% within 30 minutes of incubation in 5 mM

GSH (Figure 3.5B). These observations confirm that the polypeptide-drug conjugates are extremely stable at physiological conditions, while are released inside cells in a controlled manner when in contact with stimuli (pH and GSH).

Polypeptide-mediated delivery increases the efficacy of DOX and HDACi

Once we established the controlled release behavior of our drug-polypeptide conjugates, we then went on test their efficacy in brain tumor cells *in vitro* (Figure 3.6). In our study we used U87-EGFRvIII brain cancer cells as a model. We firstly assessed the biocompatibility of the polypeptide carrier by treating the U87 cells with increasing concentrations of the polypeptide. The polypeptide was found to be highly biocompatible with greater than 95% cell viability even at higher concentrations.

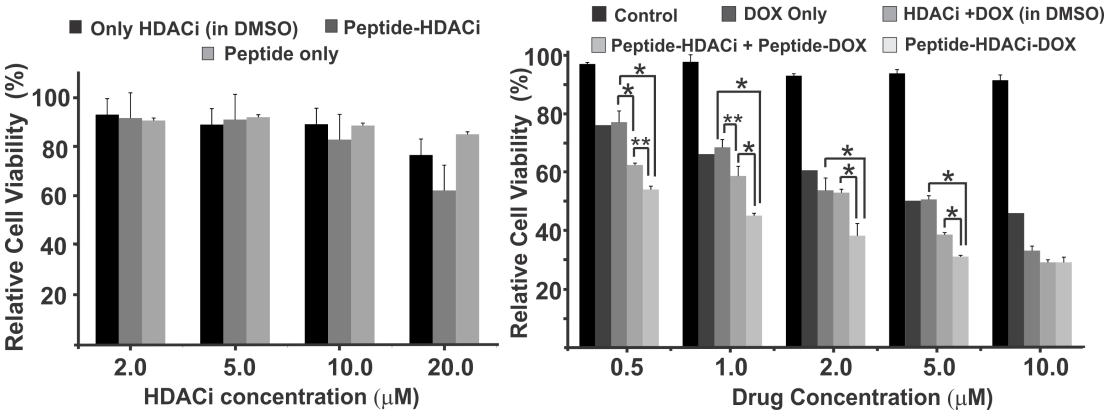

Figure 3.6: Comparison of cell viability of brain cancer cells by delivery of the HDACi in DMSO or conjugated to the polypeptide and (D) Synergistic inhibition of cell viability as determined using the MTS assay by co-delivery of DOX and HDACi conjugated to the same polypeptide as compared to delivery of DOX alone or combination of DOX and SAHA analogue in DMSO or on different peptide molecules. Cell viability of untreated cells was used as control. The results are presented as means ± SE from three independent experiments. Students unpaired t-test was used for evaluating the statistical significance of the cytotoxicities ($*= P<0.01$, $**=P<0.05$).

In order to assess the cooperative effects of the HDACi and DOX on the inhibition of brain tumor (GBM) cell proliferation, we firstly assessed the anti-proliferative capability of the drugs (HDACi and DOX) in U87-EGFRvIII cells using dimethyl sulfoxide (DMSO) as the solvent. DOX alone was found to have an IC_{50} of 5.0 μM which is consistent with previous reports. On the other hand, the synthesized HDACi was found to

have no effect on the extent of cell death even at a high concentration (20 μM, Figure 3.6A). However, when we tested the HDAC inhibition capability using an ELISA-based assay, we found that the HDACi was capable of inhibiting the enzyme by ~40% even at a very low concentration of 2 μM (Figure 3.7). Hence, our results prove that our HDACi would be capable of sensitizing the U87 cells to a DNA-damaging drug like DOX, thereby greatly enhancing its potency.

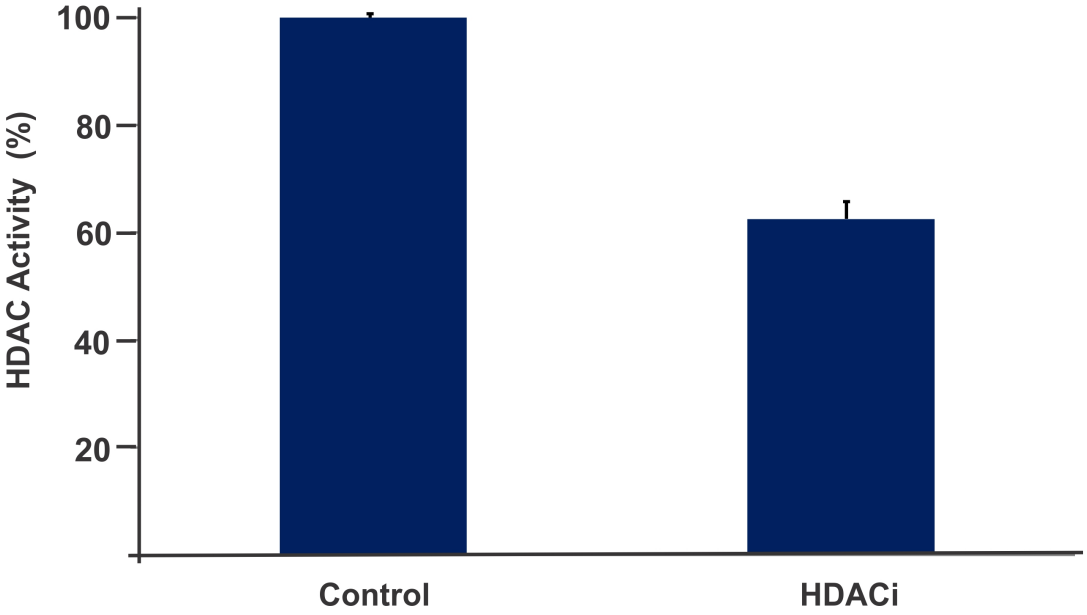

Figure 3.7: HDAC inhibition assay of novel SAHA analogue. The HDAC inhibition capability of the new HDACi was evaluated in U87-EGFRvIII cells using the fluorimetric HDAC assay kit. Cells were treated with the new HDACi at 2 μM concentration and the extent of HDAC inhibition was assessed after 48 h. The amount of deacetylated nuclear histone is reported as the percentage HDAC activity in comparison to untreated control cells from three independent experiments (n=3).

We then delivered the polypeptide-drug conjugates (polypeptide-HDACi, polypeptide-DOX and polypeptide-DOX-HDACi) at various drug concentrations to the U87-EGFRvIII cells and compared the extent of cell death using a cell viability assay (Figure 3.6B). It was found that the co-delivery of DOX and the SAHA analogue in equal concentrations using our polypeptide decreased the IC_{50} of DOX by 10 fold (0.5 μM), thereby leading to an increased chemotherapeutic effect as compared to individual or combined drug treatments in DMSO. This is in agreement to the fact that our polypeptide backbone increases the solubility of the hydrophobic drugs thereby increasing their uptake.

Interestingly, the co-delivery of the drugs on the same polypeptide molecule had a greater effect (as opposed to their delivery on different peptides). Collectively, these observations support the hypothesis the use of an HDACi allows for a more open chromatin structure which in turn enhances the efficiency of an anticancer drug targeting DNA or enzymes acting on DNA. Furthermore, it also shows that having both drugs on a single platform increases their efficacy many fold, possibly by localizing both the drugs at a single site as opposed to delivery using an admix [161].

Polypeptide-mediated siRNA delivery

Having demonstrated the potential of our polypeptide as a carrier for multiple anticancer drugs, we sought to evaluate its ability to be used as a vehicle for the efficient delivery of siRNAs. The field of RNA interference (RNAi) therapeutics, wherein siRNAs or micro RNA (miRNA) are used to selectively mediate the cleavage of complementary mRNA sequences and thus regulate target gene expression, has made significant progress since the first demonstration of gene knockdown in mammalian cells. RNAi-based formulations offer significant potential as therapeutic agents to induce potent, persistent and specific silencing of a broad range of genetic targets. In combination with other modalities like small molecules and peptides, RNAi could prove to be a powerful tool to manipulate the expression of key oncogenes in cancer [220, 221]. However, despite its potential, therapeutic application of siRNA has been greatly hindered by the lack of methods to efficiently co-deliver them with traditional anticancer drugs for enhanced chemotherapeutic efficacy. Several non-viral vectors such as cationic lipids and dendrimers have been shown to be effective for the co-delivery of siRNA and anticancer drugs in vitro, in order to elicit a synergistic response. However, most of these platforms either tend to be extremely cytotoxic or are not biodegradable, thereby leading to undesirable changes in the cellular functions. The use of our polypeptide as a siRNA delivery vehicle would not only aid in overcoming the above mentioned limitations of the traditional siRNA delivery vehicles, but would also aid in the co-delivery of drugs and siRNA in order to achieve a synergistic response towards the induction of cancer cell death.

We explored to utilize our polypeptide backbone to co-deliver DOX (as a model apoptosis-inducing anticancer drug), and a siRNA (against the EGFRvIII oncogene [244, 245]) into the highly invasive U87-EGFRvIII brain tumor cells for an enhanced apoptotic effect. Firstly, to investigate the cellular internalization and the intracellular release of siRNA, we complexed Cy3®-dye labeled scrambled siRNA to the polypeptide backbone and delivered it to U87-EGFRvIII cells. The uptake and extent of siRNA release was determined using fluorescence microscopy 24 hours post-transfection. We found that the polypeptide not only complexed the siRNA effectively and translocated it across the cell membrane, but also released it efficiently in the cytoplasm as evidenced by diffused red fluorescence in the cell (Figure 3.8A). It was also seen that polypeptide sequences lacking the histidine moieties (having only cysteine and lysine residues) complexed the siRNA but had a more punctate red fluorescence inside the cells (Figure 3.9), thereby indicating that the siRNA was not efficiently released from the endosome after uptake. These results prove that that the presence of multiple histidine residues in the polypeptide backbone is essential for ensuring the efficient endosomal rupture and release of cargo into the cellular cytoplasm.

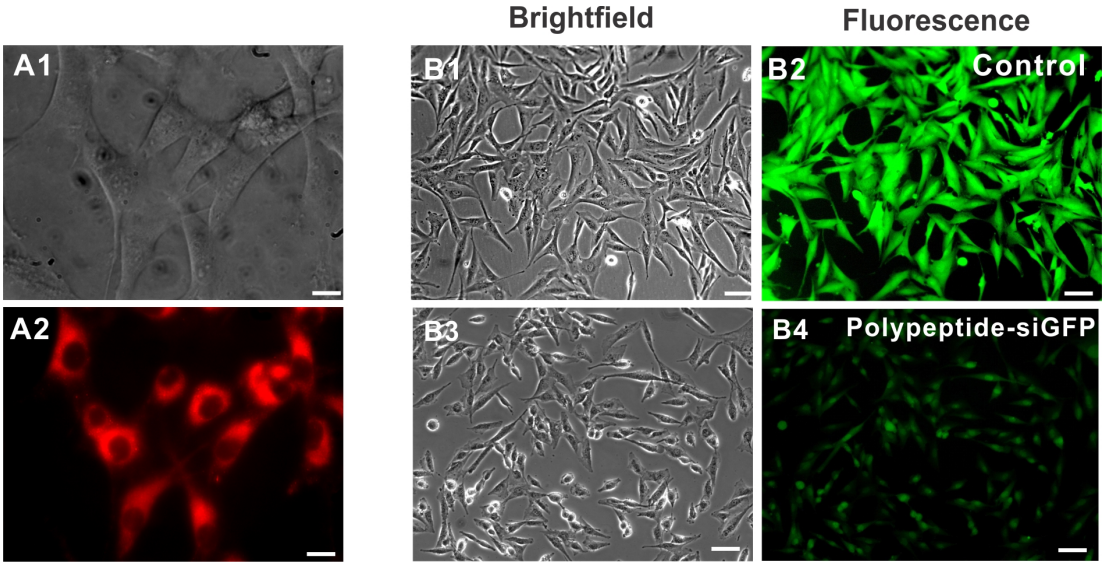

Figure 3.8: Polypeptide-mediated siRNA uptake, release and gene knockdown. (A) Cellular uptake and release of of the dye-labeled siRNA in U87-EGFRvIII cells as seen using fluorescence microscopy. (A1) represents the phase contrast image, and (A2) is the corresponding fluorescence image The siRNA is cleary seen in cellular cytoplasm (as evidenced by the diffused red fluorescence). (B) Silencing efficiency of the Polypetide-siGFP in stably transfected U87-EGFP glioblastoma cells (bottom) as compared to the control U87-EGFP cells (top) with polypeptide-scrambled siRNA; (B1) and (B3) represents the phase contrast image while (B2) and (B4) are the corresponding fluorescence images. Fluorescence images clearly show the knockdown of EGFP in the polypeptide-siEGFP transfected cells after 72 h. Scale bar is 50 μm.

We then optimized the siRNA knockdown efficiency of our polypeptide-siRNA complexes at different polypeptide concentrations in U87 glioblastoma cell-lines which were genetically modified to constitutively express the enhanced green fluorescent protein (U87-EGFP). The decrease of green fluorescence intensity due to siRNA-mediated EGFP silencing was monitored using fluorescence microscopy over a time-period of 72 h to quantify the knockdown efficiency of our polyplexes. We observed a 70% decrease in the GFP intensity after 72 h of siRNA treatment as compared to control cells, thus confirming the efficient siRNA-mediated gene knockdown using our polypeptide (Figure 3.8B).

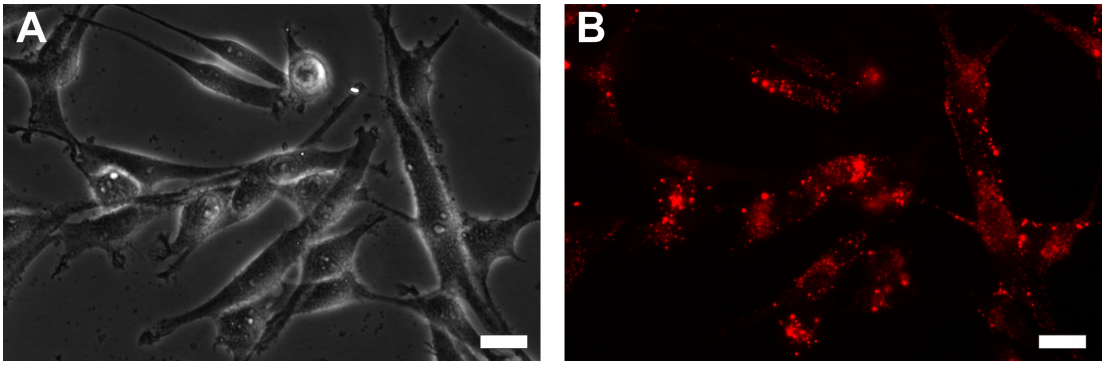

Figure 3.9: Uptake and release of Cy-3 labeled siRNA using polypeptide lacking the histidine residues. Cy-3 labeled-Silencer® siRNA was delivered to U87-EGFRvIII cells using our polypeptide at an N/P ratio of 10. The uptake and release of the siRNA was evaluated using fluorescence microscopy, where (A) shows the phase image and (B) is the corresponding fluorescence image of the siRNA inside the cells (Scale bar = 50 μm). The red fluorescence inside the cells shows the uptake of the siRNA. However, the punctate nature of the red fluorescence clearly demonstrates the inefficient release of the siRNA in the absence of an endosomal rupturing residue such as histidine.

Additionally, we also tested the ability of our polypeptide for the targeted delivery of dye-labeled siRNA to the U87 cells. In order to confer specificity, the targeting peptide Arginyl-glycyl-aspartic acid, having a terminal cysteine residue (RGDC), was conjugated to the cysteine side chain of our polypeptide backbone using a disulfide-linkage. The RGD motif is known to bind to the $\alpha_v\beta_3$ integrin receptors, which are found to be highly overexpressed on the surface of brain cancer cells and expressed in lower amounts on the HeLa cells, which in turn helps in the efficient uptake and internalization of RGD-labeled polypeptides. The polypeptide-RGD conjugate was complexed with a Cy3® dye-labeled siRNA in order to test the targeted delivery of the siRNA to brain tumor cells in comparison to HeLa cells, which are known to have low expression of the above integrin. It was found that the presence of RGD moiety on the polypeptide allowed for increasing the uptake of siRNA into U87-EGFRvIII cells as compared to HeLa cells, which is consistent with the expression levels of the integrin receptor on the respective cell lines (Figure 3.10).

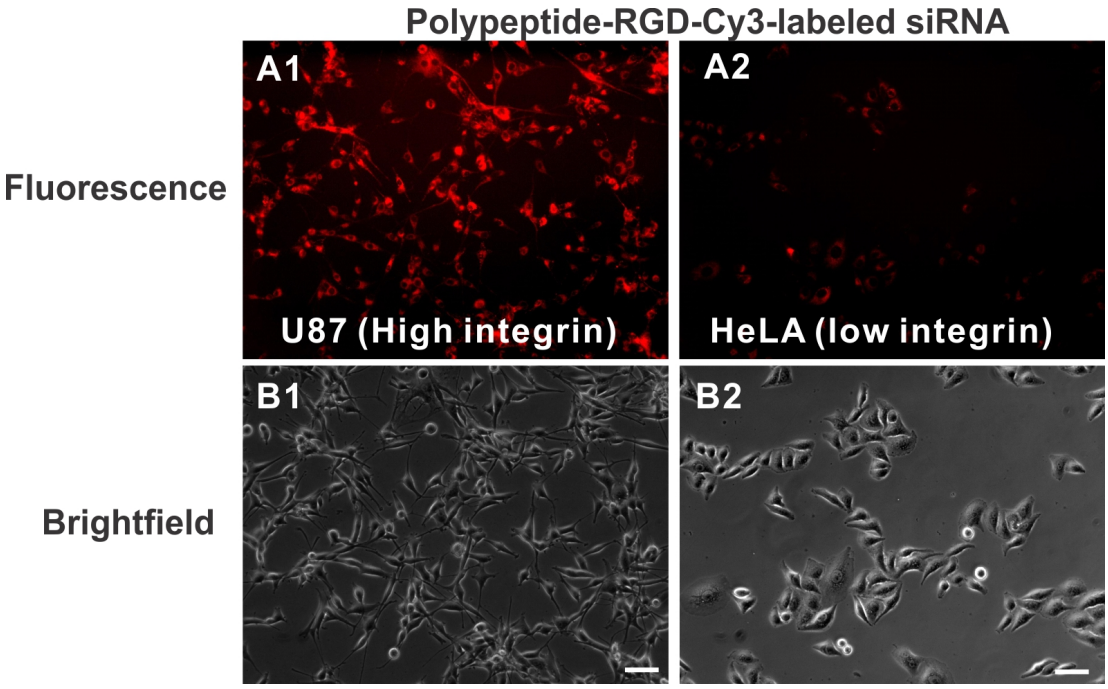

Figure 3.10: Targeted delivery of Cy3®-labeled siRNA using our polypeptide. The targeted delivery of siRNA into U87-EGFRvIII cells (having high $\alpha_v\beta_3$ intergrin expression) over HeLa cells (having low v3 integrin expression) was achieved using RGD-polypeptide conjugates. The RGD-polypeptide was complexed with the siRNA at an N/P = 10 and delivered to both U87 and HeLa cells. The higher uptake of the siRNA is evident by the higher red fluorescence (A1) in the U87 cells in comparsion to the HeLa cells (A2). Scale bar = 50 μm.

These results demonstrate the potential of our polypeptide nanocarrier for delivering the therapeutic molecules to only the target cancer cells.

Polypeptide-mediated codelivery of DOX and EGFRvIII siRNA to brain tumor cells

Having demonstrated the uptake and efficient gene silencing capability of the polypeptide-siRNA constructs, we then focused on our main goal of co-delivering siRNA and DOX for targeting the oncogenic EGFRvIII-phoshphatidylinositol-3-kinase (EGFR/PI3K) signaling pathways to achieve a cooperative chemotherapeutic effect. The PI3K pathway, implicated in the proliferation and apoptosis of brain tumor cells, is known to have significant crosstalk with other signaling pathways which are affected by DOX. In particular, DOX treatment and the siRNA-mediated inhibition of PI3K, are both

known to significantly enhance the p53 tumor suppressor gene levels, thereby leading to a synergistic effect [246]. To this end, we co-delivered DOX with siRNA against EGFRvIII oncogene to deactivate the target signaling pathway in a selective and efficient manner. It was found that the co-delivery of DOX and EGFRvIII siRNA led to a remarkable increase in cell death (80% cell death at 5 μM DOX and 100 nM siRNA) as compared to the delivery of DOX or siRNA alone at the same concentrations. Thus, these results show the cooperative effect on inducing the apoptosis of brain tumor cells using the right combination of siRNA and anti-cancer drugs (Figure 3.11).

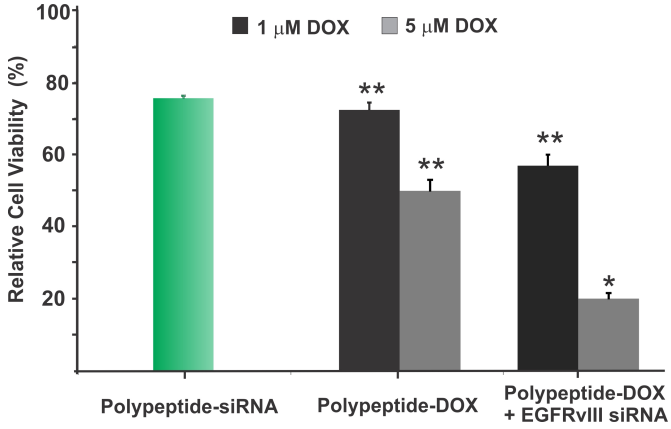

Figure 3.11: Synergistic inhibition of brain tumor cell proliferation by codelivery of siRNA and DOX using the polypeptide. Enhanced cell death by delivery of polypeptide-DOX-EGFRvIII siRNA conjugates as compared to delivery of polypeptide-DOX alone or polypeptide-EGFRvIII siRNA. The results are presented as means + SD (n=3). Students unpaired t-test was used for evaluating the statistical significance of the cytotoxicities of the polypeptide-DOX-siRNA codelivery as compared to Polypeptide-DOX or polypeptide-siRNA alone ($*$=P<0.01, $**$=P< 0.05)

3.1.3 Conclusions

We developed a biodegradable dendritic polypeptide-based drug delivery system capable of delivering multiple anticancer drugs and siRNA to brain tumor cells. The strategy of co-delivering anticancer drug with therapeutic siRNA is particularly advantageous for *in vivo* applications, so that both the moieties are delivered to the target cells using a single delivery platform, thereby precluding the necessity for multiple injections. In addition, our versatile delivery platform was demonstrated to release the drugs inside

the cancer cells in a controlled manner, which would be of immense importance in reducing the systemic toxicity of the drugs. The combined delivery of HDACi and DOX using the polypeptide-based system led to a remarkable increase in cell death as compared to the individual treatments. In particular, we could achieve a 10-fold decrease in the IC_{50} of DOX using this approach, thus demonstrating the utility of our polypeptide system for enhancing conventional therapies. Our results also proved that our co-delivery system can not only efficiently deliver the siRNA simultaneously with DOX into cytoplasm, the thus-delivered siRNA can also be efficiently released and effectively silence the targeted mRNAs to obtain a synergistic response. Collectively, our results would open new avenues for the treatment of malignant cancers like brain and breast tumors by reducing the systemic toxicity of the drugs and effectively circumventing drug resistance in tumors.

3.1.4 Materials and Methods

N(ϵ)-Boc-L-Lysine (98%), L-Histidine (98+%) and Suberic acid (98%) were obtained from Alfa Aesar. S-Benzyl-L-cysteine (97%) was obtained from Sigma Aldrich (St. Louis, MO). Tris(2-aminoethyl)amine (96%) was purchased from Acros Organics. Unless otherwise noticed, all solvents were obtained from Fisher Scientific and used as recieved. The siRNAs targeting the EGFP and EGFRvIII genes were custom designed by Integrated DNA Technologies (Coralville, IA). Silencer Cy3^{TM}–labeled Negative Control siRNA was purchased from Invitrogen (Carlsbad, CA). The polypeptides were characterized by NMR and the molecular weight was determined by MALDI-TOF analysis. ^{1}H and ^{13}C NMR spectra were recorded at 500 MHz Bruker instrument. NMR chemical shifts were reported as values in ppm relative to deuterated solvents. The size and zeta potential were measured using Zetasizer (NanoZS) dynamic light scattering instrument (Malvern Instruments, Malvern, UK). Cellular imaging studies were carried out using a Nikon Ti-Eclipsed 2000 Epifluorescence microscope (Nikon Inc.). HDAC inhibition and cell viability assays were carried out using a Tecan microplate Reader (Tecan Instruments).

Synthesis of the thiol-based HDAC inhibitor

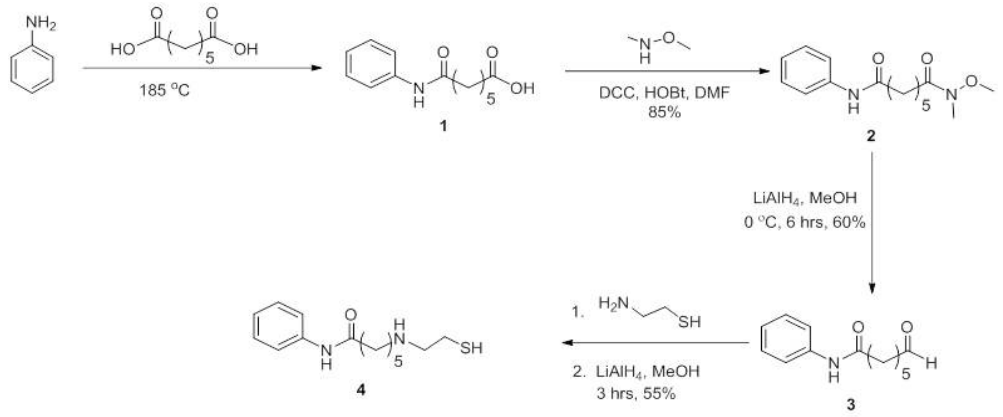

Figure 3.12: Synthetic scheme for the synthesis of the new HDAC inhibitor.

Compound 1: Commercially available aniline (2 g, 21.47 mM) as reacted with suberic acid (3.8 g, 21.47 mM) at 185°C for 7 hrs. The resulting solution was cooled to room temperature followed by acid work up to get Compound 1 (70 % yield).

Compound 2: Compound 1 was reacted with DCC and HOBt in dry DMF solution followed by the addition of N,O-dimethylhydroxyamidet at room temperature. After 6 hrs of stirring the precipitate was filtered and concentrated *in vacuo* to yield compound 2.

Compound 3: Compound 2 was reacted with $LiAlH_4$ at 0°C for 3 hrs until the solution became clear. After the completion of the reaction, MeOH was removed in vacuo and then purified using flash chromatography (70:30 Hexane/EtOAc) to yield the product (60% yield).

Compound 4: Compound 3 was treated with 2-aminoethane thiol in presence of catalytic amount of TsOH. The resulting product was reduced using $NaBH_4$. The final product was puried with flash chromatography in 70:30 EtOAc and hexane (v/v) to yield the final HDAC inhibitor 4. Yield: 55%. ^{1}H NMR (300 MHz, $CDCl_3$) δ 1.63-1.29 (m) 2.852.39 (m), 3.023.06 (t, J = 6.90 Hz,), 7.23-7.19 (m), 7.43 (d, J = 4.8 Hz). 7.61(d, J=5.8).

Synthesis of amino acid N-carboxy anhydrides (NCAs)

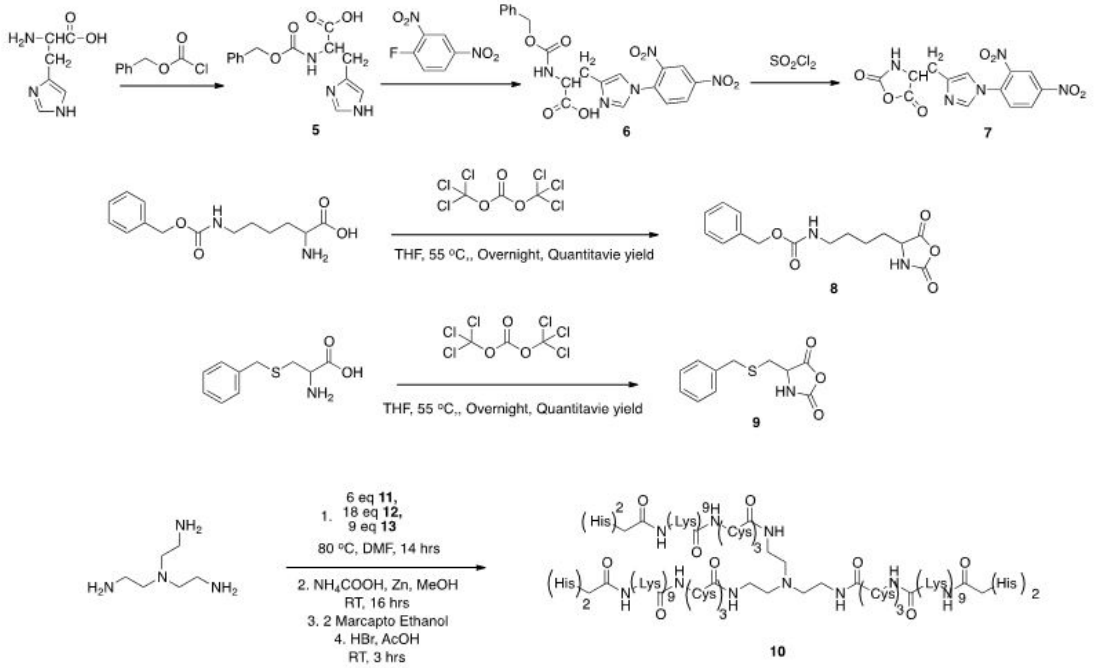

Figure 3.13: Synthetic scheme for the synthesis of the amino acid N-carboxy anhydrides (NCAs).

Synthesis of Histidine–NCA (7) N–CBZ–N–DNP–L–histidine (6, 5 g) was dissolved in anhydrous THF (35 ml) and thionyl chloride (0.8 ml) was added. The mixture turned opaque and highly viscous. The reaction was allowed to occur at room temperature, resulting in a clear solution in a few minutes. After another 40 min, an excess of anhydrous diethyl ether was added to precipitate the product and the precipitate was filtered and dried in vacuo to obtain the product 7.

Synthesis of Lysine–NCA (8) CBZ–protectected Lys (2.5 g, 8.91 mM) was treated with Triphosgene (1.4 g, 4.45 mM) in dry THF at 0°C. The solution was heated to 45°C for 12 hrs. Any visible precipitates were removed by filtration and the solvent was removed *in vacuo*. Recrystallyzation was carried out with Hexane/THF (1:1; v/v) to yield 8. ^{1}H NMR (300 MHz, $CDCl_3$) δ 7.37-7.29 (s, 5 H), 5.13 (s, 4H), 4.39-4.3 (d, 2H), 3.6 (s, 2H), 3.23 (s, 2H), 1.9-1.5 (m, 8 H)

Synthesis of Cysteine–NCA (9) S–Benzyl–L–cysteine (2 g, 9.47 mM) was treated with Triphosgene (1.4 g, 4.73 mM) in dry THF at 0°C. The solution was heated to

45°C for 12 hrs. Any visible precipitates were removed by filtration and the sovent evaporated *in vacuo*. Recrystallization was carried out with Hexane/THF (1:1; v/v) to yield the product 9. ^{1}H NMR (300 MHz, $CDCl_3$) δ 7.38-7.28 (m, 5 H), 5.85 (s, 1H), 4.28-4.26 (m, 1H), 3.79 (s, 2H), 3.0-2.79 (m, 2H)

Synthesis of the polypeptide (with and without histidine)

(10 and 11) The polypeptide was synthesized by the sequential ring opening polymerization (ROP) of the NCAs of L–cysteine, L–lysine, and L–histidine prepared above using Tris(2-aminoethyl)amine as the initiator. 20 μL of Tris(aminoethyl)amine was dissolved in dry DMF and Cysteine-NCA (283 mg, 9 eq) in dry DMF was added to it. The resulting mixture was stirred at 40°C for 5 hrs and then Lysine-NCA (855 mg, 18 eq) was added. After another 6 hrs, the Histidine-NCA was added to the solution to obtain the protected polypeptide. The de-protection of the protected cysteine was carried out using reduction in presence of AIBN (1eq) and tBu_3SnH (2 eq). The removal of the CBZ- group from the Lysine residues was carried out with HBr/AcOH (stirred for 2 hrs at room temperature) to yield the polypeptide 10. The final product further purified using dialysis (3000 MWCO) and characterized using NMR and MALDI-TOF analysis. ^{1}H NMR (300 MHz, $CDCl_3$) δ 8.06 (s, 1 H), 5.3 (s, 10 H), 4.89 (m, 6 H), 5.2-4.98 (m, 12H), 3.6-3.2(m, 6H), 2.7-2.56 (m, 12H), 1.58-1.2 (m, 38H) Another polypeptide without the histidine (*Compound 11*) was synthesized using the above method by just excluding the use of Histidine-NCA

Conjugation of DOX and HDACi to the polypeptide

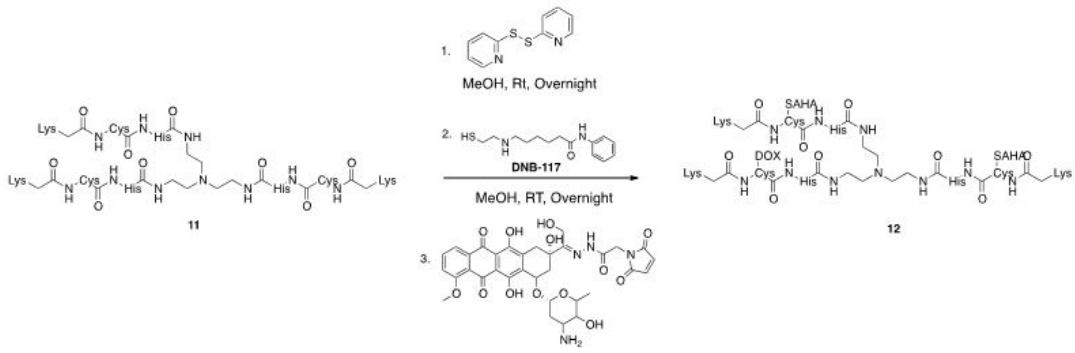

Figure 3.14: Synthetic scheme for the synthesis of the conjugation of DOX and HDACi to the polypeptide.

Activation of HDACi and conjugation to polypeptide

Disulfide linkage of compound 4 and compound 10 were done in room temperature and in MeOH. Compound 4 (2 eq) and 2,2'–Bipyridyl disulfide (2 eq) were dissolved in MeOH and stirred at room temperature for 24 hrs. The polypeptide was then added to this solution in order to conjugate the HDACi to the backbone via a disulfide linkage. After extraction with the EtOAc and water, the unreacted compound could be removed and the attached HDACi was confirmed by NMR.

Activation of DOX and subsequent conjugation to polypeptide

Commercially available Doxorubicin (DOX, LC Laboratories, Woburn, MA) was activated with and β–maleimidopropionic hydrazide (BMPH, Pierce, Rockford, IL). DOX (62 mg, 1 eq) and BMPH, (34 mg, 1eq) were dissolved in 5 mL anhydrous methanol in presence of 20 μL of TFA. The reactants were stirred for 16 hrs at 20°C in the dark and concentrated *in vacuo*. This activated-DOX (2 eq) was used in a second reaction with the Polypeptide–HDACi (1eq) in HEPES buffer (0.1 M NaH_2PO_4, 1 mM EDTA, pH=7.0). Excess DOX was removed from the solution by centrifugal filtration and subsequent dialysis (3000 MWCO) against PBS buffer. The attached DOX was confirmed using NMR and UV–Visible spectroscopy.

MALDI-TOF Analysis

The molecular weight of the synthesized polypeptide was determined using matrix-assisted laser desorption ionization-time of flight (MALDI-TOF) mass spectroscopy analysis. The polypeptide (1.0 mg/mL) was mixed with α–Cyano–4–hydroxycinnamic acid (CHCA, 2.5 mg/mL) as the matrix in 50% ACN/0.1 % TFA and spotted onto a MALDI plate. The spots were then analyzed using TOF ABI-4800 mid mass positive-reflector mode.

DLS and Zeta potential measurements

The size and zeta potential of the polypeptide and polypeptide-DOX-HDACi drug conjugates were measured at 633 nm using Zetasizer (NanoZS) dynamic light scattering instrument (Malvern Instruments, Malvern, UK) at 25°C with detection angle of 90°. The Polypeptide and Polypeptide-drug conjugates were diluted in phosphate buffered saline (PBS, pH=7.4) and then subjected to DLS and Zeta-potential measurements. At least three measurements were taken for each sample and the mean values were reported.

Loading efficiency of DOX and HDACi onto the polypeptide

Loading efficiency was defined as the ratio of the amount of DOX or HDACi conjugated to the polypeptide to the initial feed amount of the drug used for conjugation. Briefly, a solution of DOX-loaded polypeptide (30.0 μg/mL) in phosphate buffered saline (PBS, pH=7.4) was taken and the absorbance of solution was measured at 494 nm using a Cary Eclipse UV-visible spectrophotometer (Varian, USA). The amount of DOX conjugated to the polypeptide was then determined from a standard curve of DOXs absorbance at 494 nm versus the concentration. The concentration was then converted to mass of DOX on polypeptide and the loading efficiency of DOX was then calculated using the theroretical feed amount of DOX (14.68 μg of DOX) corresponding to the amount of polypeptide used. It was further confirmed using ^{1}H NMR integration. The amount of the HDACi conjugated on the polypeptide was determined using NMR integration

of a solution of the HDACi-polypeptide (2.0 mg/mL in $CDCl_3$), which showed that 1.5 molecules of HDACi were present on each polypeptide. The loading efficiency of the HDACi was then calculated using the theoretical feed amount of HDACi used in a reaction corresponding to the weight of polypeptide used.

pH-mediated DOX release from polypeptide

The DOX-loaded polypeptide (30 μg) was taken in microcentrifuge tubes and suspended in PBS buffer maintained at different pH (pH=7.4 and pH=6.0) over a period of 48 hours. At various time intervals, the solutions were centifuged using a membrane-based filter (3000 MWCO, Amicon, Millipore) in order to assay the amount of DOX released. The percentage of drug released at any given time was directly calculated from the measured absorbance of the free DOX at 494 nm and comparison to a DOX standard calibration curve.

Glutathione-mediated HDACi release from polypeptide

Solutions of HDACi-polypeptide (1.0 mM) in PBS (pH=7.4) were taken in microcentrifuge tubes. Glutathione (GSH, Sigma Aldrich) was then added to them to obtain final concentrations of 1, 2, 3, 4, and 5 mM of GSH and incubated for 30 minutes to allow for the reductive cleavage of the HDACi from the polypeptide. The solutions were than loaded onto a LC–MS instrument (LC–10, Shimadzu Scientific Instruments; Columbia, MD) having an Agilent ZORBAX C-18 column (SB-C18, 3.5 μm, 4.6 X 75 mm) and eluted with an isocratic flow of 1.0 mL min^{-1} of water:methanol:TFA [90:10:0.01]. The HPLC data was quantified by the integrated area under the peak at 4.2 mins (elution time of free HDACi as determined using calibration curve) and used to quantify the drug release. It should be noted that the peak at 4.2 mins corresponded to a molecular weight of 267.6, which in turn matched the molecular weight of free HDAC. The amount and the percentage of the HDACi released at various GSH concentrations was then calculated from a calibration curve of the HDACi obtained by running solutions of the HDACi only (in methanol) of various concentration (0, 2, 3, 4, 5 and 10 mM) on the LC–MS and the monitoring the peak area at 4.2 mins.

Culture of human U87 glioblastoma cells and HeLa cells

The EGFRvIII overexpressed U87 glioblastoma cells (U87–EGFRvIII) and human cervical cancer cells (HeLa) were cultured using previously reported methods. For U87-EGFP cells and U87-EGFRvIII cells, DMEM with high glucose, 10% fetal bovine serum (FBS, Gemini Bioproducts), 1% Streptomycin-penicillin and 1% Glutamax (Invitrogen, Carlsbad, CA) were used as basic components of growth media including Geneticin G418 (100 μg/mL, Life Technologies, Carlsbad, CA) and Hygromycin (30 μg/ml, Life Technologies, Carlsbad, CA) as selection markers for U87-EGFP and U87-EGFRvIII respectively. For the HeLa cells, DMEM (with high glucose) supplemented with 10% fetal calf serum (FCS, Gemini Bioproducts), 1% Streptomycin-penicillin and 1% Glutamax was used as the growth medium. All cells were maintained at 37°C in humidified 5% CO2 atmosphere.

Assessment of cytoxicity of HDACi and DOX in DMSO

U87-EGFRvIII cells were grown to 40-60% confluency in a 48–well plate. DOX and HDACi dissolved in DMSO were added to the cells at various concentrations using serial dilution so as to keep the total DMSO concentration at 0.1%. Cells treated with just DMSO were treated as control. The cells were washed with PBS (pH=7.4) after 6 hours and fresh growth media was added. The transfected cells were allowed to grow for 48 h, after which the cell viability was assessed using the CellTiter 96 AQueous One Solution Cell Proliferation Assay (MTS assay, Promega, Madison, USA) according to the manufacturers recommended protocol.

Assessment of HDAC inhibition capability of synthesized HDACi

U87-EGFRvIII cells were grown to 40-60% confluency in a 100 mm dish. The cells were then treated with 2.0 mM of HDACi in DMSO. Cells treated with only polypeptide and DMSO were used as controls. The final DMSO concentration was kept below 0.1% in order to avoid any cytotoxicity. The cells were washed with PBS (pH=7.4) after 6 hours of transfection and fresh growth media was added. The transfected cells were allowed

to grow for 48 h, after which the extent of HDAC inhibition was determined using an HDAC Fluorometric immunoassay kit (Cayman Chemical Company, MI, USA) using the manufacturers recommended protocol

Assessment of cytoxicity of polypeptide-drug conjugates

U87-EGFRvIII cells were grown to 40-60% confluency in a 48–well plate. The polypeptide -drug conjugates (Polypeptide-DOX, Polypeptide-HDACi, Polypeptide DOX + Polypep tide-HDACi and Polypeptide-DOX-HDACi) were susppended in PBS (pH=7.4) and diluted using Opti-MEM (Invitrogen, Carlsbad, CA) to the required concentrations. The conjugates were added to the cells. Cells treated with only polypeptide was used as the control. The cells were washed with PBS (pH=7.4) after 6 hours of transfection and fresh growth media was added. The transfected cells were allowed to grow for 48 h, after which the cell viability was assessed using the CellTiter 96 AQueous One Solution Cell Proliferation Assay (MTS assay, Promega, Madison, USA) according to the manufacturers recommended protocol.

Assesment of siRNA uptake and targeted delivery of Polypeptide-RGD-siRNA

Firstly, the uptake and efficient release of siRNA into U87-EGFRvIII cells was assessed by complexing the polypeptide (with or without histidine moeities) with Silencer Cy3^{TM}–labeled Negative Control siRNA at an N/P ratio of 10 using Opti-MEM media. U87-EGFRvIII cells were grown to 40-60% confluency in a 24-well plate and the polypeptide-siRNA conjugates were added to them. After 6 h of transfection, the cells were washed and media exchanged with fresh growth medium. The cells were then grown for 24 hours after which the cells were imaged using fluorescence microscopy (Nikon Ti-Eclipsed Inverted Fluorescence microscope, Nikon Instruments, USA). Each image was captured with different channels and focus. Images were processed and overlapped using the NIS-Elements software (Nikon, USA). For the targeted delivery of siRNA, cysteine-terminated RGD peptide (RGDC, 50 nmol, American Peptides, USA) was mixed with the histidine polypeptide (50 nmol) in PBS (pH=7.4) and allowed to stir

for 3 hours at room temperature. The unconjugated RGDC peptide was then removed using centrifugal filtration (3000 MWCO, Millipore). The RGD-conjugated polypeptide was then complexed with the Silencer Cy3^{TM}–labeled Negative Control siRNA at an N/P ratio =10. For the targeting experiments, U87-EGFRvIII and HeLa cells were grown to 40-60% confluency in a 24-well plate and the RGD–polypeptide–siRNA conjugates were added to them. Cells treated with only polypeptide–siRNA (without RGDC peptide) were used as controls. All transfection were performed in Opti-MEM media. After 4 h of transfection, the cells were washed and media exchanged with fresh growth medium. The cells were then grown for 24 hours after which the cells were imaged using fluorescence microscopy (Nikon Ti–Eclipsed Inverted Fluorescence microscope, Nikon Instruments, USA). Each image was captured with different channels and focus. Images were processed and overlapped using the NIS-Elements software (Nikon, USA).

Assessment of GFP knockdown using polypeptide-siEGFP

The EGFP overexpressed U87 glioblastoma cells (U87–EGFP) were cultured using DMEM with high glucose, 10% fetal bovine serum (FBS, Gemini Bioproducts), 1% Streptomycin-penicillin and 1% Glutamax (Invitrogen, Carlsbad, CA). Geneticin G418 (100 μg/ml, Invitrogen) was used as a selection marker for the U87–EGFP cells. All cells were maintained at 37°C in humidified 5% CO2 atmosphere. For the knockdown experiments, cells were grown to 40-60% confluency in a 24-well plate. The Polypeptide (0.2mg/mL) was complexed with 50 pmol siRNA against EGFP (siGFP) at an N/P (nitrogen to phosphate ratio) of 10. The siRNA for EGFP was designed as follows; Sense sequence was 5– GGCUACGUCCAGGAGCGC ACC and Antisense sequence was 5–phosphate–UGCGCUCCUGGACGUAGCCUU. The polypeptide-siGFP conjugates were dispersed in the transfection media (Opti-MEM) and added to the U87-EGFP cells. U87-EGFP cells treated with Polypeptide-scrambled siRNA were used as a control. After 6 hours of incubation, the solution in each well was removed and exchanged with the growth medium. The cells were allowed to grow for 72 hours after which the GFP knockdown was quantified using fluorescence microscopy (Nikon Ti-Eclipsed Inverted Fluorescence microscope, Nikon Instruments, USA). Each image

was captured with different channels and focus. Images were processed and overlapped using the NIS-Elements software (Nikon, USA).

Delivery of polypeptide-DOX-siEGFRvIII

Polypeptide–DOX–siEGFRvIII conjugates were dispersed in the transfection media (Opti–MEM) to get a siRNA concentration of 150 nM and DOX concentrations of 1 and 5 μM. The conjugates were added to the U87–EGFRvIII cells grown to 40-60% confluency in a 48–well plate. Cells treated with Polypeptide-scrambled siRNA were used as a control. After 6 hours of incubation, the solution in each well was removed and exchanged with the growth medium. The cells were allowed to grow for 48 hours after which the extent of cell proliferation was assessed using the CellTiter 96 Aqueous One Cell proliferation assay kit (Promega, Madison, WI). Experiments were carried out in triplicates and the cell viabilities reported as the means $\pm$SE.

Chapter 4

Conclusions and Perspectives

We have already seen the wide applications of several nanomaterials and nanotechnology-engineered products in the field of cancer therapy, molecular imaging and regenerative medicine. The application of nanotechnology to drug delivery is widely expected to change the landscape of pharmaceutical and biotechnology industries for the foreseeable future. The pipelines of pharmaceutical companies are believed to be drying up in many cases, and a number of blockbuster drugs will come off patent in the near-term. There has also been a concurrent increase in the utilization of the HatchWaxman Act by generic drug companies, which allows them to challenge the patents of branded drugs, further deteriorating the potential revenues of pharmaceutical companies. In this scenario, the development of nanotechnology products may play an important role in adding a new armory of therapeutics to the pipelines of pharmaceutical companies. Furthermore, considering the use of nanomaterials for stem cells applications and with the emergence of induced pluripotent stem cells (iPSCs), the field is now open wider than ever before as all the ethical concerns regarding embryonic stem cells have been bypassed for applications like tissue engineering and regenerative medicine. However, it still remains to be seen as to how many of these nanomaterials actually make it to the clinic. Issues pertaining to their toxicity and off-target effects will require careful monitoring in order to realize thier potential for drug delivery and cellular reprogramming. This thesis provided a few examples of, based on nanotechnology, towards the development of multifunctional and non-toxic drug delivery vehicles and multimodal imaging probes for i) the controlled delivery of drugs and siRNA to cancer and stem cells in order to enhance their therapeutic effects and, ii) to image or track the delivery of such cargo inside cells for diagnostic and medical relevance. Most of the methods can

also be used for the genetic reprogramming and imaging of stem cells for regenerative medicine.

In chapter 2, the applications of nanotechnology in the emerging field of diagnostics were discussed. In this chapter, we discussed the development of non-toxic quantums dots for the imaging and delivery of siRNA into brain cancer and mesenchymal stem cells, with the hope of using these quantum dots as multiplexed imaging and delivery vehicles. We were quite successful at overcoming the toxicity issues associated witht the use of conventional quantum dots, which generally consis of Cadmium and Selenium. These non-toxic QDs not only enabled us to image brain cancer and stem cells with high efficiency, but also allowed us to deliver siRNA to knockdown the target gene in brain cancer cells. Overall the project provided inspiration to explore the use of these non-toxic QDs as imaging probes for brain tumors.

Chapter 3 focused on the development of nanomaterial-based drug delivery platfoms for the codelivery of multiple anticancer therapeutics to brain tumor cells. In particular, this part of my work focused on the synthesis and use of a biodegradable dendritic polypeptide-based nanocarrier for the delivery of multiple anticancer drugs and siRNA to brain tumor cells. The codelivery of important anticancer agents using a single platform was shown to increase the efficacy of the drugs by manyfold. Further, the release of the drugs from the dendritic polypeptide was carefully controlled using orthogonal stimuli (such as low pH and reductive environment), thereby ensuring the cancer cell-specific delivery and minimizing dose limiting toxicities of the individual drugs. Furthermore, the dendritic polypeptide-based nanocarrier was successful at co-delivering small molecule drugs and siRNA in order to elicit a synergisitic inhibition of tumor cell proliferation. This would be of immense importance when used *in vivo*.

The work from this thesis has been remarkably novel. It is hoped that this work will be used for developing many more approaches for the delivery of anticancer therapeutics to brain cancer, which will eventually transpire to something relevant in the clinic. I also hope that some of this work in the development of highlyl imaging and diagnostic agents would one day be used in the clinic, thereby complementing or improving currently available medical imaging methods.

References

[1] K. Bogunia-Kubik and M. Sugisaka, "From molecular biology to nanotechnology and nanomedicine," *Biosystems*, vol. 65, no. 2-3, pp. 123–138, 2002.

[2] A. Solanki, J. Kim, and K.-B. Lee, "Nanotechnology for regenerative medicine: nanomaterials for stem cell imaging," *Nanotechnology*, vol. 3, pp. 567–578, 2008.

[3] S. Wang, N. Mamedova, N. Kotov, W. Chen, and J. Studer, "Antigen/antibody immunocomplex from cdte nanoparticle bioconjugates," *Nano Letters*, vol. 2, no. 8, pp. 817–822, 2002.

[4] M. Lewin, N. Carlesso, C. H. Tung, X. W. Tang, D. Cory, D. T. Scadden, and R. Weissleder, "Tat peptide-derivatized magnetic nanoparticles allow in vivo tracking and recovery of progenitor cells," *Nat Biotechnol*, vol. 18, no. 4, pp. 410–414, 2000.

[5] P. K. Jain, X. Huang, I. H. El-Sayed, and M. A. El-Sayed, "Noble metals on the nanoscale: Optical and photothermal properties and some applications in imaging, sensing, biology, and medicine," *Accounts of Chemical Research*, vol. 41, no. 12, pp. 1578–1586, 2008.

[6] S. Eustis and E.-S. M. A., "Why gold nanoparticles are more precious than pretty gold: Noble metal surface plasmon resonance and its enhancement of the radiative and nonradiative properties of nanocrystals of different shapes," *Chem. Soc. Rev.*, vol. 35, pp. 209–217, 2006.

[7] I. Nabiev, H. Morjani, and M. M., "Selective analysis of antitumor drug interaction with living cancer cells as probed by surface-enhanced raman spectroscopy," *Eur. Biophys. J.*, vol. 19, no. 6, pp. 311–316, 1991.

[8] K. Kneipp, A. S. Haka, H. Kneipp, K. Badizadegan, N. Yoshizawa, C. Boone, K. E. Shafer-Peltier, J. T. Motz, R. R. Dasari, and M. S. Feld, "Surface-enhanced raman spectroscopy in single living cells using gold nanoparticles," *Appl. Spectroscopy*, vol. 56, no. 2, pp. 150–154, 2002.

[9] S. Nie and S. Emory, "Probing single molecules and single nanoparticles by surface-enhanced raman scattering," *Science*, vol. 275, no. 5303, pp. 1102–1106, 1997.

[10] R. Elghanian, J. Storhoff, R. Mucic, R. Letsinger, and C. Mirkin, "Selective colorimetric detection of polynucleotides based on the distance-dependent optical properties of gold nanoparticles," *Science*, vol. 277, no. 5329, pp. 1078–1080, 1997.

[11] R. Yasuda, H. Noji, M. Yoshida, K. J. Kinosita, and H. Itoh, "Resolution of distinct rotational substeps by submillisecond kinetic analysis of f1-atpase," *Nature*, vol. 410, no. 6831, pp. 898–904, 2001.

[12] S. Schultz, D. Smith, J. Mock, and D. Schultz, "Single-target molecule detection with nonbleaching multicolor optical immunolabels," *Proc. Natl Acad. Sci. USA*, vol. 97, no. 3, pp. 996–1001, 2000.

[13] J. Yguerabide and E. Yguerabide, "Resonance light scattering particles as ultrasensitive labels for detection of analytes in a wide range of applications," *J. Cell. Biochem. Suppl.*, vol. 37, pp. 71–81, 2001.

[14] C. Sonnichsen, B. M. Reinhard, J. Liphardt, and A. Alivisatos, "A molecular ruler based on plasmon coupling of single gold and silver nanoparticles," *Nat. Biotechnol.*, vol. 23, no. 6, pp. 741–745, 2005.

[15] J. Yguerabide and E. Yguerabide, "Light scattering submicroscopic particles as highly fluorescent analogs and their use as tracer labels in clinical and biological applications," *Anal. Biochem.*, vol. 262, no. 2, pp. 137–156, 1998.

[16] N. Shaner, P. Steinbach, and R. Tsien, "A guide to choosing fluorescent proteins," *Nat. Methods*, vol. 2, no. 12, pp. 905–909, 2005.

[17] G. Patterson, S. Knobel, W. Sharif, S. Kain, and D. Piston, "Use of the green fluorescent protein and its mutants in quantitative fluorescence microscopy," *Biophys. J.*, vol. 73, pp. 2782–2790, 1997.

[18] M. Horisberger, J. Rosset, and H. Bauer, "Colloidal gold granules as markers for cell surface receptors in the scanning electron microscope," *Experientia*, vol. 31, no. 10, pp. 1147–1149, 1975.

[19] K. Sokolov, M. Follen, J. Aaron, I. Pavlova, A. Malpica, R. Lotan, and R. Richards-Kortum, "Real-time vital optical imaging of precancer using anti-epidermal growth factor receptor antibodies conjugated to gold nanoparticles," *Cancer Res.*, vol. 63, no. 9, pp. 1999–2004, 2003.

[20] S. Kumar, N. Harrison, R. Richards-Kortum, and K. Sokolov, "Plasmonic nanosensors for imaging intracellular biomarkers in live cells," *Nano Letters*, vol. 7, no. 5, p. 13381343, 2007.

[21] K. Chen, Y. Liu, G. Ameer, and V. Backman, "Optimal design of structured nanospheres for ultrasharp light-scattering resonances as molecular imaging multilabels," *J. Biomed. Opt.*, vol. 10, no. 2, p. 024005, 2005.

[22] r. D. Adle, S.-W. Huang, R. Huber, and J. Fujimoto, "Photothermal detection of gold nanoparticles using phase-sensitive optical coherence tomography," *Optics Express*, vol. 16, no. 7, pp. 4376–4393, 2008.

[23] L. R. Hirsch, R. J. Stafford, J. A. Bankson, S. R. Sershen, B. Rivera, R. E. Price, J. D. Hazle, N. J. Halas, and J. L. West, "Nanoshell-mediated near-infrared thermal therapy of tumors under magnetic resonance guidance," *Proc. Natl Acad. Sci. USA*, vol. 100, no. 23, pp. 13549–13554, 2003.

[24] C. Loo, A. Lowery, N. Halas, J. West, and R. Drezek, "Immunotargeted nanoshells for integrated cancer imaging and therapy," *Nano Letters*, vol. 5, no. 4, pp. 709–711, 2005.

[25] X. Huang, I. El-Sayed, W. Qian, and M. El-Sayed, "Cancer cell imaging and photothermal therapy in the near-infrared region by using gold nanorods," *J. Am. Chem. Soc.*, vol. 128, no. 6, pp. 2115–2120, 2006.

[26] D. Pissuwan, S. Valenzuela, M. Killingsworth, X. Xu, and C. M.B., "Targeted destruction of murine macrophage cells with bioconjugated gold nanorods," *J. Nanopart. Res.*, vol. 9, no. 6, pp. 1109–1124, 2007.

[27] S. Skrabalak, J. Chen, L. Au, X. Lu, X. Li, and Y. Xia, "Gold nanocages for biomedical applications," *Adv. Mater.*, vol. 19, no. 20, pp. 3177–3184, 2007.

[28] S. Jung, J. Nam, S. Hwang, J. Park, J. Hur, K. Im, N. Park, and S. Kim, "Theragnostic ph-sensitive gold nanoparticles for the selective surface enhanced raman scattering and photothermal cancer therapy," *Analytical Chemistry*, vol. 85, no. 16, pp. 7674–7681, 2013.

[29] J. Aaron, N. Nitin, K. Travis, S. Kumar, M. Jos-Yacamn, L. Coghlan, M. Follen, R. Richards-Kortum, K. Sokolov, T. Collier, and S. Y. Park, "Plasmon resonance coupling of metal nanoparticles for molecular imaging of carcinogenesis in vivo," *J. Biomed. Opt.*, vol. 12, no. 3, pp. 034007–034007–11, 2007.

[30] I. El-Sayed, X. Huang, and M. El-Sayed, "Surface plasmon resonance scattering and absorption of anti-egfr antibody conjugated gold nanoparticles in cancer diagnostics: applications in oral cancer," *Nano Letters*, vol. 5, no. 5, pp. 829–834, 2005.

[31] M. Skala, M. Crow, A. Wax, and J. Izatt, "Photothermal optical coherence tomography of epidermal growth factor receptor in live cells using immunotargeted gold nanospheres," *Nano Letters*, vol. 8, no. 10, pp. 3461–3467, 2008.

[32] X. Yang, S. Skrabalak, Z. Li, Y. Xia, and L. Wang, "Photoacoustic tomography of a rat cerebral cortex in vivo with au nanocages as an optical contrast agent," *Nano Letters*, vol. 7, no. 12, pp. 3798–3802, 2007.

[33] S. Mallidi, T. Larson, J. Aaron, K. Sokolov, and S. Emelianov, "Molecular specific optoacoustic imaging with plasmonic nanoparticles," *Optics Express*, vol. 15, no. 11, pp. 6583–6588, 2007.

[34] L. Christopher, H. Leon, L. Min-Ho, C. Emmanuel, W. Jennifer, H. Naomi, and D. Rebekah, "Gold nanoshell bioconjugates for molecular imaging in living cells," *Opt. Lett.*, vol. 30, no. 9, pp. 1012–1014, 2005.

[35] L. Bickford, G. Agollah, R. Drezek, and T. Yu, "Silica-gold nanoshells as potential intraoperative molecular probes for her2-overexpression in ex vivo breast tissue using near-infrared reflectance confocal microscopy," *Breast Cancer Res. Treat.*, vol. 120, no. 3, pp. 547–555, 2010.

[36] E. Day, L. Bickford, J. Slater, N. Riggall, R. Drezek, and J. West, "Antibody-conjugated goldgold sulfide nanoparticles as multifunctional agents for imaging and therapy of breast cancer," *Int. J. Nanomed.*, vol. 5, p. 445454, 2010.

[37] J. Li, L. Zheng, H. Cai, W. Sun, M. Shen, G. Zhang, and X. Shi, "Polyethyleneimine-mediated synthesis of folic acid-targeted iron oxide nanoparticles for in vivo tumor {MR} imaging," *Biomaterials*, vol. 34, no. 33, pp. 8382 – 8392, 2013.

[38] J. W. M. Bulte, T. Douglas, B. Witwer, S. C. Zhang, E. Strable, B. K. Lewis, H. Zywicke, B. Miller, P. van Gelderen, B. M. Moskowitz, I. D. Duncan, and J. A. Frank, "Magnetodendrimers allow endosomal magnetic labeling and in vivo tracking of stem cells," *Nature Biotechnology*, vol. 19, no. 12, pp. 1141–1147, 2001.

[39] E. R. Chemaly, R. Yoneyama, J. V. Frangioni, and R. J. Hajjar, "Tracking stem cells in the cardiovascular system," *Trends in Cardiovascular Medicine*, vol. 15, no. 8, pp. 297–302, 2005.

[40] O. Veiseh, J. W. Gunn, and M. Zhang, "Design and fabrication of magnetic nanoparticles for targeted drug delivery and imaging," *Advanced Drug Delivery Reviews*, vol. 2, no. 3, pp. 284 – 304, 2010.

[41] R. Hao, R. Xing, Z. Xu, Y. Hou, S. Gao, and S. Sun, "Synthesis, functionalization, and biomedical applications of multifunctional magnetic nanoparticles," *Advanced Materials*, vol. 22, no. 25, pp. 2729–2742, 2010.

[42] D. L. J. Thorek, A. Chen, J. Czupryna, and A. Tsourkas, "Superparamagnetic iron oxide nanoparticle probes for molecular imaging," *Annals of Biomedical Engineering*, vol. 34, no. 1, pp. 23–38, 2006.

[43] F. M. Kievit, Z. R. Stephen, O. Veiseh, H. Arami, T. Wang, V. P. Lai, J. O. Park, R. G. Ellenbogen, M. L. Disis, and M. Zhang, "Targeting of primary breast cancers and metastases in a transgenic mouse model using rationally designed multifunctional spions," *ACS Nano*, vol. 6, no. 3, pp. 2591–2601, 2012.

[44] D. Yoo, J.-H. Lee, T.-H. Shin, and J. Cheon, "Theranostic magnetic nanoparticles," *Accounts of Chemical Research*, vol. 44, no. 10, pp. 863–874, 2011.

[45] C. R. Thomas, D. P. Ferris, J. H. Lee, E. Choi, M. H. Cho, E. S. Kim, J. F. Stoddart, J. S. Shin, J. Cheon, and J. I. Zink, "Noninvasive remote-controlled release of drug molecules in vitro using magnetic actuation of mechanized nanoparticles," *J Am Chem Soc*, vol. 132, no. 31, pp. 10623–10625, 2010.

[46] S. Dutz, W. Andra, R. Hergt, R. Muller, C. Oestreich, C. Schmidt, J. Topfer, M. Zeisberger, and M. E. Bellemann, "Influence of dextran coating on the magnetic behaviour of iron oxide nanoparticles," *Journal of Magnetism and Magnetic Materials*, vol. 311, no. 1, pp. 51–54, 2007.

[47] R. Lawaczeck, M. Menzel, and H. Pietsch, "Superparamagnetic iron oxide particles: contrast media for magnetic resonance imaging," *Applied Organometallic Chemistry*, vol. 18, no. 10, pp. 506–513, 2004.

[48] M. Mahmoudi, H. Hosseinkhani, M. Hosseinkhani, S. Boutry, A. Simchi, W. S. Journeay, K. Subramani, and S. Laurent, "Magnetic resonance imaging tracking of stem cells in vivo using iron oxide nanoparticles as a tool for the advancement of clinical regenerative medicine," *Chemical Reviews*, vol. 111, no. 2, pp. 253–280, 2011.

[49] J. Xie, G. Liu, H. S. Eden, H. Ai, and X. Chen, "Surface-engineered magnetic nanoparticle platforms for cancer imaging and therapy," *Accounts of Chemical Research*, vol. 44, no. 10, pp. 883–892, 2011.

[50] J. Xie, K. Chen, J. Huang, S. Lee, J. Wang, J. Gao, X. Li, and X. Chen, "Pet/nirf/mri triple functional iron oxide nanoparticles," *Biomaterials*, vol. 31, no. 11, pp. 3016 – 3022, 2010.

[51] C. Xu and S. Sun, "New forms of superparamagnetic nanoparticles for biomedical applications," *Advanced Drug Delivery Reviews*, vol. 65, no. 5, pp. 732 – 743, 2013.

[52] S. Sherlock and H. Dai, "Multifunctional feco-graphitic carbon nanocrystals for combined imaging, drug delivery and tumor-specific photothermal therapy in mice," *Nano Research*, vol. 4, no. 12, pp. 1248–1260, 2011.

[53] H. Kosuge, S. P. Sherlock, T. Kitagawa, M. Terashima, J. K. Barral, D. G. Nishimura, H. Dai, and M. V. McConnell, "Feco/graphite nanocrystals for multimodality imaging of experimental vascular inflammation," *PLoS One*, vol. 6, no. 1, p. e14523, 2011.

[54] L. V. Nguyen, R. Vanner, P. Dirks, and C. J. Eaves, "Cancer stem cells: an evolving concept," *Nature Reviews Cancer*, vol. 12, no. 2, pp. 133–143, 2012.

[55] A. K. Gupta and A. S. G. Curtis, "Lactoferrin and ceruloplasmin derivatized superparamagnetic iron oxide nanoparticles for targeting cell surface receptors," *Biomaterials*, vol. 25, no. 15, pp. 3029–3040, 2004.

[56] W. J. Rogers, C. H. Meyer, and C. M. Kramer, "Technology insight: in vivo cell tracking by use of mri," *Nature Clinical Practice Cardiovascular Medicine*, vol. 3, no. 10, pp. 554–562, 2006.

[57] C. W. Lu, Y. Hung, J. K. Hsiao, M. Yao, T. H. Chung, Y. S. Lin, S. H. Wu, S. C. Hsu, H. M. Liu, C. Y. Mou, C. S. Yang, D. M. Huang, and Y. C. Chen, "Bifunctional magnetic silica nanoparticles for highly efficient human stem cell labeling," *Nano Letters*, vol. 7, no. 1, pp. 149–154, 2007.

[58] L.-Y. Chien, J.-K. Hsiao, S.-C. Hsu, M. Yao, C.-W. Lu, H.-M. Liu, Y.-C. Chen, C.-S. Yang, and D.-M. Huang, "In vivo magnetic resonance imaging of cell tropsim, trafficking mechanism, and therapeutic impact of human mesenchymal stem cells in a murine glioma model," *Biomaterials*, vol. 32, no. 12, pp. 3275–3284, 2011.

[59] T.-H. Chung, J.-K. Hsiao, S.-C. Hsu, M. Yao, Y.-C. Chen, S.-W. Wang, M. Y.-P. Kuo, C.-S. Yang, and D.-M. Huang, "Iron oxide nanoparticle-induced epidermal growth factor receptor expression in human stem cells for tumor therapy," *ACS Nano*, vol. 5, no. 12, pp. 9807–9816, 2011.

[60] D. L. Kraitchman, A. W. Heldman, E. Atalar, L. C. Amado, B. J. Martin, M. F. Pittenger, J. M. Hare, and J. W. Bulte, "In vivo magnetic resonance imaging of mesenchymal stem cells in myocardial infarction," *Circulation*, vol. 107, pp. 2290–2293, 2003.

[61] J. Emerit, C. Beaumont, and F. Trivin, "Iron metabolism, free radicals, and oxidative injury," *Biomedecine and Pharmacotherapy*, vol. 55, no. 6, pp. 333–339, 2001.

[62] F. H. Wang, I. H. Lee, N. Holmstrom, T. Yoshitake, D. K. Kim, M. Muhammed, J. Frisen, L. Olson, C. Spenger, and J. Kehr, "Magnetic resonance tracking of nanoparticle labelled neural stem cells in a rat's spinal cord," *Nanotechnology*, vol. 17, no. 8, pp. 1911–1915, 2006.

[63] C. M. Niemeyer and B. Ceyhan, "Dna-directed functionalization of colloidal gold with proteins," *Angewandte Chemie-International Edition*, vol. 40, pp. 3685–3688, 2001.

[64] X. H. Gao, L. L. Yang, J. A. Petros, F. F. Marshal, J. W. Simons, and S. M. Nie, "In vivo molecular and cellular imaging with quantum dots," *Current Opinion in Biotechnology*, vol. 16, no. 1, pp. 63–72, 2005.

[65] X. Michalet, F. F. Pinaud, L. A. Bentolila, J. M. Tsay, S. Doose, J. J. Li, G. Sundaresan, A. M. Wu, S. S. Gambhir, and S. Weiss, "Quantum dots for live cells, in vivo imaging, and diagnostics," *Science*, vol. 307, no. 5709, pp. 538–544, 2005.

[66] M. N. Rhyner, A. M. Smith, X. H. Gao, H. Mao, L. L. Yang, and S. M. Nie, "Quantum dots and multifunctional nanoparticles: new contrast agents for tumor imaging," *Nanomedicine*, vol. 1, no. 2, pp. 209–217, 2006.

[67] S. M. Nie, Y. Xing, G. J. Kim, and J. W. Simons, "Nanotechnology applications in cancer," *Annual Review of Biomedical Engineering*, vol. 9, pp. 257–288, 2007.

[68] S. Lin, X. Y. Xie, M. R. Patel, Y. H. Yang, Z. J. Li, F. Cao, O. Gheysens, Y. Zhang, S. S. Gambhir, J. H. Rao, and J. C. Wu, "Quantum dot imaging for embryonic stem cells," *Bmc Biotechnology*, vol. 7, 2007.

[69] I. L. Medintz, H. T. Uyeda, E. R. Goldman, and H. Mattoussi, "Quantum dot bioconjugates for imaging labelling and sensing," *Nature Materials*, vol. 4, pp. 435–446, 2005.

[70] X. H. Gao, W. C. W. Chan, and S. M. Nie, "Quantum-dot nanocrystals for ultrasensitive biological labeling and multicolor optical encoding," *Journal of Biomedical Optics*, vol. 7, no. 4, pp. 532–537, 2002.

[71] S. M. Nie, "Luminescent quantum dots for multiplexed optical tagging of genes, proteins, and cells," *Cytometry*, pp. 25–25, 2002.

[72] X. H. Gao and S. M. Nie, "Molecular profiling of single cells and tissue specimens with quantum dots," *Trends in Biotechnology*, vol. 21, no. 9, pp. 371–373, 2003.

[73] P. Allen and M. Bawendi, "Ternary iiiivi quantum dots luminescent in the red to near-infrared," *J. Am. Chem. Soc.*, vol. 130, pp. 9240–9241, 2008.

[74] E. Cassette, T. Pons, C. Bouet, M. Helle, L. Bezdetnaya, F. Marchal, and B. Dubertret, "Synthesis and characterization of near-infrared cuinse/zns core/shell quantum dots for in vivo imaging," *Chem. Mat.*, vol. 22, pp. 6117–6124, 2010.

[75] Y. Hamanaka, T. Ogawa, M. Tsuzuki, and T. Kuzuya, "Photoluminescence properties and its origin of agins2 quantum dots with chalcopyrite structure," *J. Phys. Chem. C*, vol. 115, pp. 1786–1792, 2011.

[76] X. Tang, W. Cheng, E. Choo, and J. Xue, "Synthesis of $cuins_2$–zns alloyed nanocubes with high luminescence," *Chem. Comm.*, vol. 47, no. 18, pp. 5217–5219, 2011.

[77] T. Torimoto, T. Adachi, K.-I. Okazaki, M. Sakuraoka, T. Shibayama, B. Ohtani, A. Kudo, and S. Kuwabata, "Facile synthesis of zns-$agins_2$ solid solution nanoparticles for a color-adjustable luminophore," *J. Am. Chem. Soc.*, vol. 129, no. 41, pp. 12388–12389, 2007.

[78] R. Xie, M. Rutherford, and X. Peng, "Formation of high-quality i-iii-vi semiconductor nanocrystals by tuning relative reactivity of cationic precursors," *J. Am. Chem. Soc.*, vol. 131, pp. 5691–5697, 2009.

[79] W. C. W. Chan and S. Nie, "Quantum dot bioconjugates for ultrasensitive nonisotopic detection," *Science*, vol. 281, no. 5385, pp. 2016–2018, 1998.

[80] M. Bruchez, M. Moronne, P. Gin, S. Weiss, and A. P. Alivisatos, "Semiconductor nanocrystals as fluorescent biological labels," *Science*, vol. 281, no. 5385, pp. 2013–2016, 1998.

[81] X. Wu, H. Liu, J. Liu, K. Haley, J. Treadway, J. Larson, N. Ge, F. Peale, and M. Bruchez, "Immunofluorescent labeling of cancer marker her2 and other cellular targets with semiconductor quantum dots," *Nat. Biotech.*, vol. 21, pp. 41–46, 2003.

[82] X. Gao, Y. Cui, R. M. Levenson, L. W. K. Chung, and S. Nie, "In vivo cancer targeting and imaging with semiconductor quantum dots," *Nat Biotech*, vol. 22, no. 8, pp. 969–976, 2004.

[83] H. Tada, H. Higuchi, T. M. Wanatabe, and N. Ohuchi, "In vivo real-time tracking of single quantum dots conjugated with monoclonal anti–her2 antibody in tumors of mice," *Cancer Research*.

[84] H. Zhang, D. Sachdev, C. Wang, A. Hubel, M. Gaillard-Kelly, and D. Yee, "Detection and downregulation of type i igf receptor expression by antibody-conjugated quantum dots in breast cancer cells," *Breast Cancer Research and Treatment*, vol. 114, no. 2, pp. 277–285, 2009.

[85] E. Voura, J. Jaiswal, H. Mattoussi, and S. Simon, "Tracking metastatic tumor cell extravasation with quantum dot nanocrystals and fluorescence emission-scanning microscopy," *Nature Med.*, 2004.

[86] M. Stroh, J. Zimmer, D. Duda, T. Levchenko, K. Cohen, E. Brown, D. Scadden, V. Torchilin, M. Bawendi, D. Fukumura, and R. Jain, "Quantum dots spectrally distinguish multiple species within the tumor milieu in vivo," *Nat Med.*, vol. 11, no. 6, pp. 678–682, 2005.

[87] Z. Li, K. Wang, W. Tan, J. Li, Z. Fu, C. Ma, H. Li, X. He, and J. Liu, "Immunofluorescent labeling of cancer cells with quantum dots synthesized in aqueous solution," *Analytical Biochemistry*, vol. 354, no. 2, pp. 169 – 174, 2006.

[88] W. Cai, D.-W. Shin, K. Chen, O. Gheysens, Q. Cao, S. X. Wang, S. S. Gambhir, and X. Chen, "Peptide-labeled near-infrared quantum dots for imaging tumor vasculature in living subjects," *Nano Letters*, vol. 6, no. 4, pp. 669–676, 2006.

[89] Y. Xing, Q. Chaudry, C. Shen, K. Y. Kong, H. E. Zhau, L. WChung, J. A. Petros, R. M. O'Regan, M. V. Yezhelyev, J. W. Simons, M. D. Wang, and S. Nie, "Bioconjugated quantum dots for multiplexed and quantitative immunohistochemistry," *Nature Protocols*, vol. 2, no. 5, pp. 1152–1165, 2007.

[90] C. Chen, J. Peng, H.-S. Xia, G.-F. Yang, Q.-S. Wu, L.-D. Chen, L.-B. Zeng, Z.-L. Zhang, D.-W. Pang, and Y. Li, "Quantum dots-based immunofluorescence technology for the quantitative determination of her2 expression in breast cancer," *Biomaterials*, vol. 30, no. 15, pp. 2912–2918, 2009.

[91] X.-L. Liu, C.-W. Peng, C. Chen, X.-Q. Yang, M.-B. Hu, H.-S. Xia, S.-P. Liu, D.-W. Pang, and Y. Li, "Quantum dots-based double-color imaging of her2 positive breast cancer invasion," *Biochemical and Biophysical Research Communications*, vol. 409, no. 3, pp. 577–582, 2011.

[92] H. Zhang, D. Yee, and C. Wang, "Quantum dots for cancer diagnosis and therapy: biological and clinical perspectives," *Nanomedicine*, vol. 3, no. 1, pp. 83–91, 2008.

[93] A. Smith, H. Duan, A. Mohs, and S. Nie, "Bioconjugated quantum dots for in vivo molecular and cellular imaging," *Adv. Drug Del. Rev.*, vol. 60, no. 11, pp. 1226–1240, 2008.

[94] A. S. Arbab, V. Frenkel, S. D. Pandit, S. A. Anderson, G. T. Yocum, M. Bur, H. M. Khuu, E. J. Read, and J. A. Frank, "Magnetic resonance imaging and confocal microscopy studies of magnetically labeled endothelial progenitor cells trafficking to sites of tumor angiogenesis," *Stem Cells*, vol. 24, no. 3, pp. 671–678, 2006.

[95] A. B. Rosen, D. J. Kelly, A. J. T. Schuldt, J. Lu, I. A. Potapova, S. V. Doronin, K. J. Robichaud, R. B. Robinson, M. R. Rosen, P. R. Brink, G. R. Gaudette, and I. S. Cohen, "Finding fluorescent needles in the cardiac haystack: Tracking human mesenchymal stem cells labeled with quantum dots for quantitative in vivo three-dimensional fluorescence analysis," *Stem Cells*, vol. 25, no. 8, pp. 2128–2138, 2007.

[96] J. R. Slotkin, L. Chakrabarti, H. N. Dai, R. S. E. Carney, T. Hirata, B. S. Bregman, G. I. Gallicano, J. G. Corbin, and T. F. Haydar, "In vivo quantum dot labeling of mammalian stem and progenitor cells," *Developmental Dynamics*, vol. 236, pp. 3393–3401, 2007.

[97] J. C. Wu, "Comparison of imaging techniques for tracking cardiac stem cell therapy," *Journal of Nuclear Medicine*, vol. 48, pp. 1916–1919, 2007.

[98] H. Chen, I. Titushkin, M. Stroscio, and M. Cho, "Altered membrane dynamics of quantum dot-conjugated integrins during osteogenic differentiation of human bone marrow derived progenitor cells," *Biophysical Journal*, vol. 92, no. 1399-1408, p. 1399, 2007.

[99] K. C. Weng, C. O. Noble, B. Papahadjopoulos-Sternberg, F. F. Chen, D. C. Drummond, D. B. Kirpotin, D. Wang, Y. K. Hom, B. Hann, and J. W. Park, "Targeted tumor cell internalization and imaging of multifunctional quantum dot-conjugated immunoliposomes in vitro and in vivo," *Nano Letters*, vol. 8, no. 9, pp. 2851–2857, 2008.

[100] P. Jianhong Zhu, M.D., M. Liangfu Zhou, P. Jianhong Zhu, M.D., and M. Liangfu Zhou, "Tracking neural stem cells in patients with brain trauma," *The new england journal of medicine*, vol. 355, no. 22, pp. 2376–2378, 2006.

[101] B. J. Muller-Borer, M. C. Collins, P. R. Gunst, W. E. Cascio, Kypson, and A. P, "Quantum dot labeling of mesenchymal stem cells," *Journal of Nanobiotechnology*, vol. 5, no. 9, 2007.

[102] L. S. Shah, P. A. Clark, E. K. Moioli, M. A. Stroscio, and J. J. Mao, "Labeling of mesenchymal stem cells by bioconjugated quantum dots," *Nano Letters*, vol. 7, pp. 3071–3079, 2007.

[103] T. Jamieson, R. Bakhshi, D. Petrova, R. Pocock, M. Imani, and A. M. Seifalian, "Biological applications of quantum dots," *Biomaterials*, vol. 28, pp. 4717–4732, 2007.

[104] B. I. Ipe, M. Lehnig, and C. M. Niemeyer, "On the generation of free radical species from quantum dots," *Small*, vol. 1, no. 7, pp. 706–709, 2005.

[105] C. Kirchner, T. Liedl, S. Kudera, T. Pellegrino, A. M. Javier, H. E. Gaub, S. Stolzle, N. Fertig, and W. J. Parak, "Cytotoxicity of colloidal cdse and cdse/zns nanoparticles," *Nano Letters*, vol. 5, no. 2, pp. 331–338, 2005.

[106] A. P. Alivisatos, W. W. Gu, and C. Larabell, "Quantum dots as cellular probes," *Annual Review of Biomedical Engineering*, vol. 7, pp. 55–76, 2005.

[107] P. Subramaniam, S. J. Lee, S. Shah, S. Patel, V. Starovoytov, and K. B. Lee, "Generation of a library of non-toxic quantum dots for cellular imaging and sirna delivery," *Adv Mater*, vol. 24, no. 29, pp. 4014–9, 2012.

[108] E. M. Pridgen, R. Langer, and O. C. Farokhzad, "Biodegradable, polymeric nanoparticle delivery systems for cancer therapy," *Nanomedicine*, vol. 2, no. 5, pp. 669–680, 2007.

[109] K. Y, "Virosomes: evolution of the liposome as a targeted drug delivery system," *Adv. Drug Deliv. Rev.*, vol. 43, no. 2.

[110] V. P. Torchilin, "Recent advances with liposomes as pharmaceutical carriers," *Nat Rev Drug Discov*, vol. 4, no. 2, pp. 145–60, 2005.

[111] A. T. Florence and N. Hussain, "Transcytosis of nanoparticle and dendrimer delivery systems: evolving vistas," *Adv Drug Deliv Rev*, vol. 50 Suppl 1, pp. S69–89, 2001.

[112] C. C. Lee, J. A. MacKay, J. M. Frechet, and F. C. Szoka, "Designing dendrimers for biological applications," *Nat Biotechnol*, vol. 23, no. 12, pp. 1517–26, 2005.

[113] T. Murakami and K. Tsuchida, "Recent advances in inorganic nanoparticle-based drug delivery systems," *Mini Rev Med Chem*, vol. 8, no. 2, pp. 175–83, 2008.

[114] Y. Ding, S. Li, and G. Nie, "Nanotechnological strategies for therapeutic targeting of tumor vasculature," *Nanomedicine*, vol. 8, no. 7, pp. 1209–1222, 2013.

[115] F. Sonvico, S. Mornet, S. Vasseur, C. Dubernet, D. Jaillard, J. Degrouard, J. Hoebeke, E. Duguet, P. Colombo, and P. Couvreur, "Folate-conjugated iron oxide nanoparticles for solid tumor targeting as potential specific magnetic hyperthermia mediators: Synthesis, physicochemical characterization, and in vitro experiments," *Bioconjugate Chemistry*, vol. 16, no. 5, pp. 1181–1188, 2005.

[116] J. D. Duran, J. L. Arias, V. Gallardo, and A. V. Delgado, "Magnetic colloids as drug vehicles," *J Pharm Sci*, vol. 97, no. 8, pp. 2948–83, 2008.

[117] M. E. Davis, Z. G. Chen, and D. M. Shin, "Nanoparticle therapeutics: an emerging treatment modality for cancer," *Nat Rev Drug Discov*, vol. 7, no. 9, pp. 771–82, 2008.

[118] M. Namdeo, S. Saxena, R. Tankhiwale, M. Bajpai, Y. M. Mohan, and S. K. Bajpai, "Magnetic nanoparticles for drug delivery applications," *J Nanosci Nanotechnol*, vol. 8, no. 7, pp. 3247–71, 2008.

[119] N. Kohler, C. Sun, A. Fichtenholtz, J. Gunn, C. Fang, and M. Zhang, "Methotrexate-immobilized poly(ethylene glycol) magnetic nanoparticles for mr imaging and drug delivery," *Small*, vol. 2, no. 6, pp. 785–792, 2006.

[120] M. Liong, J. Lu, M. Kovochich, T. Xia, S. G. Ruehm, A. E. Nel, F. Tamanoi, and J. I. Zink, "Multifunctional inorganic nanoparticles for imaging, targeting, and drug delivery," *ACS Nano*, vol. 2, no. 5, pp. 889–896, 2008.

[121] S.-H. Hu, C.-H. Tsai, C.-F. Liao, D.-M. Liu, and S.-Y. Chen, "Controlled rupture of magnetic polyelectrolyte microcapsules for drug delivery," *Langmuir*, vol. 24, no. 20, pp. 11811–11818, 2008.

[122] T. K. Jain, J. Richey, M. Strand, D. L. Leslie-Pelecky, C. A. Flask, and V. Labhasetwar, "Magnetic nanoparticles with dual functional properties: drug delivery and magnetic resonance imaging," *Biomaterials*, vol. 29, no. 29, pp. 4012–21, 2008.

[123] M. Yu, Y. Jeong, J. Park, S. Park, J. Kim, J. Min, K. Kim, and S. Jon, "Drug-loaded superparamagnetic iron oxide nanoparticles for combined cancer imaging and therapy in vivo," *Angewandte Chemie International Edition*, vol. 47, no. 29, pp. 5362–5365, 2008.

[124] J. Zhang and R. D. Misra, "Magnetic drug-targeting carrier encapsulated with thermosensitive smart polymer: core-shell nanoparticle carrier and drug release response," *Acta Biomater*, vol. 3, no. 6, pp. 838–50, 2007.

[125] C. Sun, O. Veiseh, J. Gunn, C. Fang, S. Hansen, D. Lee, R. Sze, R. G. Ellenbogen, J. Olson, and M. Zhang, "In vivo mri detection of gliomas by chlorotoxin-conjugated superparamagnetic nanoprobes," *Small*, vol. 4, no. 3, 2008.

[126] N. Kohler, C. Sun, J. Wang, and M. Zhang, "Methotrexate-modified superparamagnetic nanoparticles and their intracellular uptake into human cancer cells," *Langmuir*, vol. 21, no. 19, pp. 8858–8864, 2005.

[127] J. Yang, C.-H. Lee, H.-J. Ko, J.-S. Suh, H.-G. Yoon, K. Lee, Y.-M. Huh, and S. Haam, "Multifunctional magneto-polymeric nanohybrids for targeted detection and synergistic therapeutic effects on breast cancer," *Angewandte Chemie International Edition*, vol. 46, no. 46, pp. 8836–8839, 2007.

[128] T. R. Brummelkamp, R. Bernards, and R. Agami, "Stable suppression of tumorigenicity by virus-mediated rna interference," *Cancer Cell*, vol. 2, no. 3, pp. 243–7, 2002.

[129] J.-H. Lee, K. Lee, S. Moon, Y. Lee, T. Park, and J. Cheon, "All-in-one target-cell-specific magnetic nanoparticles for simultaneous molecular imaging and sirna delivery," *Angewandte Chemie International Edition*, vol. 48, no. 23, pp. 4174–4179, 2009.

[130] Z. Medarova, W. Pham, C. Farrar, V. Petkova, and A. Moore, "In vivo imaging of sirna delivery and silencing in tumors," *Nat Med*, vol. 13, no. 3, pp. 372–7, 2007.

[131] C. S. Kumar and F. Mohammad, "Magnetic nanomaterials for hyperthermia-based therapy and controlled drug delivery," *Advanced Drug Delivery Reviews*, vol. 63, no. 9, pp. 789 – 808, 2011.

[132] I. H. El-Sayed, X. Huang, and M. A. El-Sayed, "Selective laser photo-thermal therapy of epithelial carcinoma using anti-egfr antibody conjugated gold nanoparticles," *Cancer Lett*, vol. 239, no. 1, pp. 129–35, 2006.

[133] X. Huang, P. K. Jain, I. H. El-Sayed, and M. A. El-Sayed, "Determination of the minimum temperature required for selective photothermal destruction of cancer cells with the use of immunotargeted gold nanoparticles," *Photochem Photobiol*, vol. 82, no. 2, pp. 412–7, 2006.

[134] J. Chen, D. Wang, J. Xi, L. Au, A. Siekkinen, A. Warsen, Z.-Y. Li, H. Zhang, Y. Xia, and X. Li, "Immuno gold nanocages with tailored optical properties for targeted photothermal destruction of cancer cells," *Nano Letters*, vol. 7, no. 5, pp. 1318–1322, 2007.

[135] J. L. Santos, D. Pandita, J. Rodrigues, A. P. Pego, P. L. Granja, G. Balian, and H. Tomas, "Receptor-mediated gene delivery using pamam dendrimers conjugated with peptides recognized by mesenchymal stem cells," *Mol Pharm*, vol. 7, no. 3, pp. 763–74, 2010.

[136] M. Goldberg, R. Langer, and X. Jia, "Nanostructured materials for applications in drug delivery and tissue engineering," *J Biomater Sci Polym Ed*, vol. 18, no. 3, pp. 241–68, 2007.

[137] C. L. Gebhart and A. V. Kabanov, "Evaluation of polyplexes as gene transfer agents," *J Control Release*, vol. 73, no. 2-3, pp. 401–16, 2001.

[138] D. Pandita, J. L. Santos, J. Rodrigues, A. P. Pego, P. L. Granja, and H. Tomas, "Gene delivery into mesenchymal stem cells: a biomimetic approach using rgd nanoclusters based on poly(amidoamine) dendrimers," *Biomacromolecules*, vol. 12, no. 2, pp. 472–81, 2011.

[139] A. D. Bangham, M. M. Standish, and J. C. Watkins, "Diffusion of univalent ions across the lamellae of swollen phospholipids," *J Mol Biol*, vol. 13, no. 1, pp. 238–52, 1965.

[140] F. Olson, C. A. Hunt, F. C. Szoka, W. J. Vail, and D. Papahadjopoulos, "Preparation of liposomes of defined size distribution by extrusion through polycarbonate membranes," *Biochim Biophys Acta*, vol. 557, no. 1, pp. 9–23, 1979.

[141] P. Couvreur and C. Vauthier, "Nanotechnology: intelligent design to treat complex disease," *Pharm Res*, vol. 23, no. 7, pp. 1417–50, 2006.

[142] A. Hubert, O. Lyass, D. Pode, and A. Gabizon, "Doxil (caelyx): an exploratory study with pharmacokinetics in patients with hormone-refractory prostate cancer," *Anticancer Drugs*, vol. 11, no. 2, pp. 123–7, 2000.

[143] I. Judson, J. A. Radford, M. Harris, J. Y. Blay, Q. van Hoesel, A. le Cesne, A. T. van Oosterom, M. J. Clemons, C. Kamby, C. Hermans, J. Whittaker, E. Donato di Paola, J. Verweij, and S. Nielsen, "Randomised phase ii trial of pegylated liposomal doxorubicin (doxil/caelyx) versus doxorubicin in the treatment of advanced or metastatic soft tissue sarcoma: a study by the eortc soft tissue and bone sarcoma group," *Eur J Cancer*, vol. 37, no. 7, pp. 870–7, 2001.

[144] P. Guaglianone, K. Chan, E. DelaFlor-Weiss, R. Hanisch, S. Jeffers, D. Sharma, and F. Muggia, "Phase i and pharmacologic study of liposomal daunorubicin (daunoxome)," *Invest New Drugs*, vol. 12, no. 2, pp. 103–10, 1994.

[145] E. A. Forssen, R. Male-Brune, J. P. Adler-Moore, M. J. Lee, P. G. Schmidt, T. B. Krasieva, S. Shimizu, and B. J. Tromberg, "Fluorescence imaging studies for the disposition of daunorubicin liposomes (daunoxome) within tumor tissue," *Cancer Res*, vol. 56, no. 9, pp. 2066–75, 1996.

[146] K. A. Jaeckle, T. Batchelor, S. J. O'Day, S. Phuphanich, P. New, G. Lesser, A. Cohn, M. Gilbert, R. Aiken, D. Heros, L. Rogers, E. Wong, D. Fulton, J. C. Gutheil, S. Baidas, J. M. Kennedy, W. Mason, P. Moots, C. Russell, L. J. Swinnen, and S. B. Howell, "An open label trial of sustained-release cytarabine (depocyt) for the intrathecal treatment of solid tumor neoplastic meningitis," *J Neurooncol*, vol. 57, no. 3, pp. 231–9, 1971.

[147] M. J. Glantz, K. A. Jaeckle, M. C. Chamberlain, S. Phuphanich, L. Recht, L. J. Swinnen, B. Maria, S. LaFollette, G. B. Schumann, B. F. Cole, and S. B. Howell,

"A randomized controlled trial comparing intrathecal sustained-release cytarabine (depocyt) to intrathecal methotrexate in patients with neoplastic meningitis from solid tumors," *Clin Cancer Res*, vol. 5, no. 11, pp. 3394–402, 1999.

[148] L. Zhang, D. Pornpattananangku, C. M. Hu, and C. M. Huang, "Development of nanoparticles for antimicrobial drug delivery," *Curr Med Chem*, vol. 17, no. 6, pp. 585–94, 2010.

[149] V. Agrawal, M. K. Paul, and A. K. Mukhopadhyay, "6-mercaptopurine and daunorubicin double drug liposomes-preparation, drug-drug interaction and characterization," *J Liposome Res*, vol. 15, no. 3-4, pp. 141–55, 2005.

[150] J. A. Nelson, J. W. Carpenter, L. M. Rose, and D. J. Adamson, "Mechanisms of action of 6-thioguanine, 6-mercaptopurine, and 8-azaguanine," *Cancer Res*, vol. 35, no. 10, pp. 2872–8, 1975.

[151] M. Saad, O. B. Garbuzenko, and T. Minko, "Co-delivery of sirna and an anticancer drug for treatment of multidrug-resistant cancer," *Nanomedicine (Lond)*, vol. 3, no. 6, pp. 761–76, 2008.

[152] L. Zhang, A. F. Radovic-Moreno, F. Alexis, F. X. Gu, P. A. Basto, V. Bagalkot, S. Jon, R. S. Langer, and O. C. Farokhzad, "Co-delivery of hydrophobic and hydrophilic drugs from nanoparticle-aptamer bioconjugates," *ChemMedChem*, vol. 2, no. 9, pp. 1268–71, 2007.

[153] S. Aryal, C. M. Hu, and L. Zhang, "Polymer–cisplatin conjugate nanoparticles for acid-responsive drug delivery," *ACS Nano*, vol. 4, no. 1, pp. 251–8, 2010.

[154] Y. Takakura and M. Hashida, "Macromolecular drug carrier systems in cancer chemotherapy: macromolecular prodrugs," *Crit Rev Oncol Hematol*, vol. 18, no. 3, pp. 207–31, 1995.

[155] F. Kratz, U. Beyer, and M. T. Schutte, "Drug-polymer conjugates containing acid-cleavable bonds," *Crit Rev Ther Drug Carrier Syst*, vol. 16, no. 3, pp. 245–88, 1999.

[156] J. Zhou, T. R. Patel, M. Fu, J. P. Bertram, and W. M. Saltzman, "Octa-functional plga nanoparticles for targeted and efficient sirna delivery to tumors," *Biomaterials*, vol. 33, no. 2, pp. 583–91, 2012.

[157] D. Bazile, C. Prud'homme, M. T. Bassoullet, M. Marlard, G. Spenlehauer, and M. Veillard, "Stealth me.peg-pla nanoparticles avoid uptake by the mononuclear phagocytes system," *J Pharm Sci*, vol. 84, no. 4, pp. 493–8, 1995.

[158] E. Allemann, N. Brasseur, O. Benrezzak, J. Rousseau, S. V. Kudrevich, R. W. Boyle, J. C. Leroux, R. Gurny, and J. E. Van Lier, "Peg-coated poly(lactic acid) nanoparticles for the delivery of hexadecafluoro zinc phthalocyanine to emt-6 mouse mammary tumours," *J Pharm Pharmacol*, vol. 47, no. 5, pp. 382–7, 1995.

[159] X. R. Song, Z. Cai, Y. Zheng, G. He, F. Y. Cui, D. Q. Gong, S. X. Hou, S. J. Xiong, X. J. Lei, and Y. Q. Wei, "Reversion of multidrug resistance by co-encapsulation of vincristine and verapamil in plga nanoparticles," *Eur J Pharm Sci*, vol. 37, no. 3-4, pp. 300–5, 2009.

[160] C. E. Soma, C. Dubernet, D. Bentolila, S. Benita, and P. Couvreur, "Reversion of multidrug resistance by co-encapsulation of doxorubicin and cyclosporin a in polyalkylcyanoacrylate nanoparticles," *Biomaterials*, vol. 21, no. 1, pp. 1–7, 2000.

[161] J. Lehar, A. S. Krueger, W. Avery, A. M. Heilbut, L. M. Johansen, E. R. Price, R. J. Rickles, r. Short, G. F., J. E. Staunton, X. Jin, M. S. Lee, G. R. Zimmermann, and A. A. Borisy, "Synergistic drug combinations tend to improve therapeutically relevant selectivity," *Nat Biotechnol*, vol. 27, no. 7, pp. 659–66, 2009.

[162] S. Cao and Y. M. Rustum, "Synergistic antitumor activity of irinotecan in combination with 5-fluorouracil in rats bearing advanced colorectal cancer: role of drug sequence and dose," *Cancer Res*, vol. 60, no. 14, pp. 3717–21, 2000.

[163] A. J. Sawyer, J. K. Saucier-Sawyer, C. J. Booth, J. Liu, T. Patel, J. M. Piepmeier, and W. M. Saltzman, "Convection-enhanced delivery of camptothecin-loaded polymer nanoparticles for treatment of intracranial tumors," *Drug Deliv Transl Res*, vol. 1, no. 1, pp. 34–42, 2011.

[164] A. D. Frankel and C. O. Pabo, "Cellular uptake of the tat protein from human immunodeficiency virus," *Cell*, vol. 55, no. 6, pp. 1189–1193, 1988.

[165] K. Green, M. D. Brand, and M. P. Murphy, "Prevention of mitochondrial oxidative damage as a therapeutic strategy in diabetes," *Diabetes*, vol. 53 Suppl 1, pp. S110–S118, 2004.

[166] S. Deshayes, M. C. Morris, G. Divita, and F. Heitz, "Cell-penetrating peptides: tools for intracellular delivery of therapeutics," *Cell Mol Life Sci*, vol. 62, no. 16, pp. 1839–1849, 2005.

[167] B. Gupta, T. S. Levchenko, and V. P. Torchilin, "Intracellular delivery of large molecules and small particles by cell-penetrating proteins and peptides," *Adv Drug Deliv Rev*, vol. 57, no. 4, pp. 637–651, 2005.

[168] A. Joliot and A. Prochiantz, "Transduction peptides: from technology to physiology," *Nat Cell Biol*, vol. 6, no. 3, pp. 189–196, 2004.

[169] E. L. Snyder and S. F. Dowdy, "Cell penetrating peptides in drug delivery," *Pharm Res*, vol. 21, no. 3, pp. 389–93, 2004.

[170] M. Zhao and R. Weissleder, "Intracellular cargo delivery using tat peptide and derivatives," *Med Res Rev*, vol. 24, no. 1, pp. 1–12, 2004.

[171] E. A. Goun, T. H. Pillow, L. R. Jones, J. B. Rothbard, and P. A. Wender, "Molecular transporters: synthesis of oligoguanidinium transporters and their application to drug delivery and real-time imaging," *Chembiochem*, vol. 7, no. 10, pp. 1497–1515, 2006.

[172] B. Geueke, K. Namoto, I. Agarkova, J. C. Perriard, H. P. Kohler, and D. Seebach, "Bacterial cell penetration by beta3-oligohomoarginines: indications for passive transfer through the lipid bilayer," *Chembiochem*, vol. 6, no. 6, pp. 982–985, 2005.

[173] J. Farrera-Sinfreu, E. Giralt, S. Castel, F. Albericio, and M. Royo, "Cell-penetrating cis-gamma-amino-l-proline-derived peptides," *J Am Chem Soc*, vol. 127, no. 26, pp. 9459–9468, 2005.

[174] S. E. Eldred, M. R. Pancost, K. M. Otte, D. Rozema, S. S. Stahl, and S. H. Gellman, "Effects of side chain configuration and backbone spacing on the gene delivery properties of lysine-derived cationic polymers," *Bioconjug Chem*, vol. 16, no. 3, pp. 694–699, 2005.

[175] T. B. Potocky, J. Silvius, A. K. Menon, and S. H. Gellman, "Hela cell entry by guanidinium-rich beta-peptides: importance of specific cation-cell surface interactions," *Chembiochem*, vol. 8, no. 8, pp. 917–926, 2007.

[176] A. Astriab-Fisher, D. Sergueev, M. Fisher, B. R. Shaw, and R. L. Juliano, "Conjugates of antisense oligonucleotides with the tat and antennapedia cell-penetrating peptides: effects on cellular uptake, binding to target sequences, and biologic actions," *Pharm Res*, vol. 19, no. 6, pp. 744–754, 2002.

[177] A. Nori, K. D. Jensen, M. Tijerina, P. Kopeckova, and J. Kopecek, "Tat-conjugated synthetic macromolecules facilitate cytoplasmic drug delivery to human ovarian carcinoma cells," *Bioconjug Chem*, vol. 14, no. 1, pp. 44–50, 2003.

[178] M. Zhao, M. F. Kircher, L. Josephson, and R. Weissleder, "Differential conjugation of tat peptide to superparamagnetic nanoparticles and its effect on cellular uptake," *Bioconjug Chem*, vol. 13, no. 4, pp. 840–4, 2002.

[179] V. P. Torchilin, R. Rammohan, V. Weissig, and T. S. Levchenko, "Tat peptide on the surface of liposomes affords their efficient intracellular delivery even at low temperature and in the presence of metabolic inhibitors," *Proc Natl Acad Sci U S A*, vol. 98, no. 15, pp. 8786–91, 2001.

[180] J. B. Rothbard, S. Garlington, Q. Lin, T. Kirschberg, E. Kreider, P. L. McGrane, P. A. Wender, and P. A. Khavari, "Conjugation of arginine oligomers to cyclosporin a facilitates topical delivery and inhibition of inflammation," *Nat Med*, vol. 6, no. 11, pp. 1253–1257, 2000.

[181] M. Lindgren, K. Rosenthal-Aizman, K. Saar, E. Eiriksdottir, Y. Jiang, M. Sassian, P. Ostlund, M. Hallbrink, and U. Langel, "Overcoming methotrexate resistance in breast cancer tumour cells by the use of a new cell-penetrating peptide," *Biochem Pharmacol*, vol. 71, no. 4, pp. 416–425, 2006.

[182] T. A. Kirschberg, C. L. VanDeusen, J. B. Rothbard, M. Yang, and P. A. Wender, "Arginine-based molecular transporters: the synthesis and chemical evaluation of releasable taxol-transporter conjugates," *Org Lett*, vol. 5, no. 19, pp. 3459–3462, 2003.

[183] M. J. Dixon, L. Bourre, A. J. MacRobert, and I. M. Eggleston, "Novel prodrug approach to photodynamic therapy: Fmoc solid-phase synthesis of a cell permeable peptide incorporating 5-aminolaevulinic acid," *Bioorg Med Chem Lett*, vol. 17, no. 16, pp. 4518–4522, 2007.

[184] J. F. Liang and V. C. Yang, "Synthesis of doxorubicin-peptide conjugate with multidrug resistant tumor cell killing activity," *Bioorg Med Chem Lett*, vol. 15, no. 22, pp. 5071–5075, 2005.

[185] M. Mazel, P. Clair, C. Rousselle, P. Vidal, J. M. Scherrmann, D. Mathieu, and J. Temsamani, "Doxorubicin-peptide conjugates overcome multidrug resistance," *Anticancer Drugs*, vol. 12, no. 2, pp. 107–116, 2001.

[186] M. Fritzer, T. Szekeres, V. Szuts, H. N. Jarayam, and H. Goldenberg, "Cytotoxic effects of a doxorubicin-transferrin conjugate in multidrug-resistant kb cells," *Biochem Pharmacol*, vol. 51, no. 4, pp. 489–493, 1996.

[187] S. Santra, H. Yang, D. Dutta, J. T. Stanley, P. H. Holloway, W. Tan, B. M. Moudgil, and R. A. Mericle, "Tat conjugated, fitc doped silica nanoparticles for bioimaging applications," *Chem Commun (Camb)*, no. 24, pp. 2810–2811, 2004.

[188] T. Jiang, E. S. Olson, Q. T. Nguyen, M. Roy, P. A. Jennings, and R. Y. Tsien, "Tumor imaging by means of proteolytic activation of cell-penetrating peptides," *Proc Natl Acad Sci U S A*, vol. 101, no. 51, pp. 17867–17872, 2004.

[189] T. Pons and H. Mattoussi, "Investigating biological processes at the single molecule level using luminescent quantum dots," *Annals of Biomed. Eng.*, vol. 37, pp. 1934–1959, 2009.

[190] J. B. Delehanty, H. Mattoussi, and I. L. Medintz, "Delivering quantum dots into cells: strategies, progress and remaining issues," *Analytical and Bioanalytical Chemistry*, vol. 393, pp. 1091–1105, 2009.

[191] A. Derfus, W. Chan, and S. Bhatia, "Probing the cytotoxicity of semiconductor quantum dots," *Nano Lett.*, vol. 4, pp. 11–18, 2003.

[192] J. Jung, A. Solanki, K. A. Memoli, K.-i. Kamei, H. Kim, M. A. Drahl, L. J. Williams, H.-R. Tseng, and K. Lee, "Selective inhibition of human brain tumor cells through multifunctional quantum-dot-based sirna delivery," *Angewandte Chemie-International Edition*, vol. 49, no. 1, pp. 103–107, 2010.

[193] D. Larson, W. Zipfel, R. Williams, S. Clark, M. Bruchez, F. Wise, and W. Webb, "Water-soluble quantum dots for multiphoton fluorescence imaging in vivo," *Science*, vol. 300, pp. 1434–1436, 2003.

[194] A. Derfus, A. Chen, D.-H. Min, E. Ruoslahti, and S. Bhatia, "Targeted quantum dot conjugates for sirna delivery," *Bioconj. Chem.*, vol. 18, pp. 1391–1396, 2007.

[195] M. Yezhelyev, L. Qi, R. ORegan, S. Nie, and X. Gao, "Proton-sponge coated quantum dots for sirna delivery and intracellular imaging," *J. Am. Chem. Soc.*, vol. 130, pp. 9006–9012, 2008.

[196] Y. Su, Y. He, H. Lu, L. Sai, Q. Li, W. Li, L. Wang, P. Shen, Q. Huang, and C. Fan, "The cytotoxicity of cadmium based, aqueous phase - synthesized, quantum dots and its modulation by surface coating," *Biomat.*, vol. 30, no. 1, pp. 19–25, 2009.

[197] H. Zhong, Y. Zhou, M. Ye, Y. He, J. Ye, C. He, C. Yang, and Y. Li, "Controlled synthesis and optical properties of colloidal ternary chalcogenide cuins2 nanocrystals," *Chem. Mat.*, vol. 20, pp. 6434–6443, 2008.

[198] J. Nairn, P. Shapiro, B. Twamley, T. Pounds, R. von Wandruszka, T. Fletcher, M. Williams, C. Wang, and M. Norton, "Preparation of ultrafine chalcopyrite nanoparticles via the photochemical decomposition of molecular single-source precursors," *Nano Lett.*, vol. 6, pp. 1218–1223, 2006.

[199] J. Gardner, E. Shrudha, L. Lau, C. Wang, R. Rodriguez, and J. Pak, "Rapid and size controlled synthesis of cuins2 nanopartilces via microwave irradiation," *J. Nanopart. Res.*, vol. 10, pp. 633–641, 2008.

[200] C.-C. Chen, C.-P. Yet, H.-N. Wang, and C.-Y. Chao, "Self-assembly of monolayers of cadmium selenide nanocrystals with dual color emission," *Langmuir*, vol. 15, pp. 6845–6850, 1999.

[201] G. Mitchell, C. Mirkin, and R. Letsinger, "Programmed assembly of dna functionalized quantum dots," *J. Am. Chem. Soc.*, vol. 121, no. 35, pp. 8122–8123, 1999.

[202] P. Mitchell, "Turning the spotlight on cellular imaging," *Nat. Biotech.*, vol. 19, no. 11, pp. 1013–1017, 2001.

[203] X. Gao, L. Yang, J. Petros, F. Marshall, J. Simons, and S. Nie, "In vivo molecular and cellular imaging with quantum dots," *Current Opinion in Biotechnology*, vol. 16, no. 1, pp. 63–72, 2005.

[204] W. Liu, M. Howarth, A. Greytak, Y. Zheng, D. Nocera, A. Ting, and M. Bawendi, "Compact biocompatible quantum dots functionalized for cellular imaging," *J. Am. Chem. Soc.*, vol. 130, no. 4, pp. 1274–1284, 2008.

[205] B. Shah, P. Clark, E. Moioli, M. Stroscio, and J. Mao, "Labeling of mesenchymal stem cells by bioconjugated quantum dots," *Nano Lett.*, vol. 7, pp. 3071–3079, 2007.

[206] J. Park, J. Jung, P. Subramaniam, B. Shah, C. Kim, J. Lee, J.-H. Cho, C. Lee, and K.-B. Lee, "Graphite-coated magnetic nanoparticles as multimodal imaging probes and cooperative therapeutic agents for tumor cells," *Small*, vol. 7, pp. 1647–1652, 2011.

[207] B. Shah, C. Kim, P. Subramaniam, and K.-B. Lee, "Synergistic induction of apoptosis in brain cancer cells by targeted codelivery of sirna and anticancer drugs," *Mol. Pharmaceutics*, vol. 8, pp. 1955–1961, 2011.

[208] H. Wang, K.-J. Chen, S. Wang, M. Ohashi, K.-I. Kamei, J. Sun, J. Ha, K. Liu, and T. H.-R., "A small library of dna-encapsulated supramolecular nanoparticles for targeted gene delivery," *Chem. Comm.*, vol. 46, pp. 1851–1853, 2010.

[209] X. Xue, F. Wang, and X. Liu, "Emerging functional nanomaterials for therapeutics," *J. Mater. Chem.*, vol. 21, pp. 13107–13127, 2011.

[210] J. H. Jeong, H. Mok, Y.-K. Oh, and T. G. Park, "sirna conjugate delivery systems," *Bioconjugate Chemistry*, vol. 20, no. 1, pp. 5–14, 2009.

[211] M. L. Patil, M. Zhang, S. Betigeri, O. Taratula, H. He, and T. Minko, "Surface-modified and internally cationic polyamidoamine dendrimers for efficient sirna delivery," *Bioconjugate Chemistry*, vol. 19, no. 7, pp. 1396–1403, 2008.

[212] A. Zintchenko, A. Philipp, A. Dehshahri, and E. Wagner, "Simple modifications of branched pei lead to highly efficient sirna carriers with low toxicity," *Bioconjugate Chemistry*, vol. 19, no. 7, pp. 1448–1455, 2008.

[213] A. Elbakry, A. Zaky, R. Liebl, R. Rachel, A. Goepferich, and M. Breunig, "Layer-by-layer assembled gold nanoparticles for sirna delivery," *Nano Lett.*, vol. 9, pp. 2059–2064, 2009.

[214] A. Veeravagu, Z. Liu, G. Niu, K. Chen, B. Jia, W. Cai, C. Jin, A. R. Hsu, A. J. Connolly, V. Tse, F. Wang, and X. Chen, "Integrin alpha$_v$beta$_3$-targeted radioimmunotherapy of glioblastoma multiforme," *Clinical Cancer Research*, vol. 14, no. 22, pp. 7330–7339, 2008.

[215] M. S. Lesniak and H. Brem, "Targeted therapy for brain tumours," *Nature Reviews Drug Discovery*, vol. 3, no. 6, pp. 499–508, 2004.

[216] F. Mac Gabhann, B. H. Annex, and A. S. Popel, "Gene therapy from the perspective of systems biology," *Current Opinion in Molecular Therapeutics*, vol. 12, no. 5, pp. 570–577, 2010.

[217] J. S. Caldwell, *Cancer cell-based genomic and small molecule screens*, vol. 96 of *Advances in Cancer Research*, pp. 145–173. Academic Press, 2007.

[218] I. Collins and P. Workman, "New approaches to molecular cancer therapeutics," *Nature Chemical Biology*, vol. 2, no. 12, pp. 689–700, 2006.

[219] D. H. Kim and J. J. Rossi, "Strategies for silencing human disease using rna interference," *Nature Reviews Genetics*, vol. 8, no. 3, pp. 173–184, 2007.

[220] D. Bumcrot, M. Manoharan, V. Koteliansky, and D. W. Y. Sah, "Rnai therapeutics: a potential new class of pharmaceutical drugs," *Nature Chemical Biology*, vol. 2, no. 12, pp. 711–719, 2006.

[221] D. Castanotto and J. J. Rossi, "The promises and pitfalls of rna-interference-based therapeutics," *Nature*, vol. 457, no. 7228, pp. 426–433, 2009.

[222] A. M. Chen, M. Zhang, D. G. Wei, D. Stueber, O. Taratula, T. Minko, and H. X. He, "Co-delivery of doxorubicin and bcl-2 sirna by mesoporous silica nanoparticles enhances the efficacy of chemotherapy in multidrug-resistant cancer cells," *Small*, vol. 5, no. 23, pp. 2673–2677, 2009.

[223] C. H. Zhu, S. Jung, S. B. Luo, F. H. Meng, X. L. Zhu, T. G. Park, and Z. Y. Zhong, "Co-delivery of sirna and paclitaxel into cancer cells by biodegradable cationic micelles based on pdmaema-pcl- pdmaema triblock copolymers," *Biomaterials*, vol. 31, no. 8, pp. 2408–2416, 2010.

[224] S. M. Moghimi, A. C. Hunter, and J. C. Murray, "Long-circulating and target-specific nanoparticles: theory to practice," *Pharmacol Rev*, vol. 53, no. 2, pp. 283–318, 2001.

[225] S. Svenson and D. A. Tomalia, "Dendrimers in biomedical applications–reflections on the field," *Adv Drug Deliv Rev*, vol. 57, no. 15, pp. 2106–29, 2005.

[226] L. Roglin, E. H. M. Lempens, and E. W. Meijer, "A synthetic tour de force: Well-defined multivalent and multimodal dendritic structures for biomedical applications," *Angewandte Chemie International Edition*, vol. 50, no. 1, pp. 102–112, 2011.

[227] M. A. Mintzer, E. L. Dane, G. A. OToole, and M. W. Grinstaff, "Exploiting dendrimer multivalency to combat emerging and re-emerging infectious diseases," *Molecular Pharmaceutics*, vol. 9, no. 3, pp. 342–354, 2012.

[228] J. A. MacKay, M. Chen, J. R. McDaniel, W. Liu, A. J. Simnick, and A. Chilkoti, "Self-assembling chimeric polypeptide-doxorubicin conjugate nanoparticles that abolish tumours after a single injection," *Nat Mater*, vol. 8, no. 12, pp. 993–9, 2009.

[229] J. R. McDaniel, D. J. Callahan, and A. Chilkoti, "Drug delivery to solid tumors by elastin-like polypeptides," *Adv Drug Deliv Rev*, vol. 62, no. 15, pp. 1456–67, 2010.

[230] N. Wiradharma, Y. W. Tong, and Y. Y. Yang, "Self-assembled oligopeptide nanostructures for co-delivery of drug and gene with synergistic therapeutic effect," *Biomaterials*, vol. 30, no. 17, pp. 3100–9, 2009.

[231] H. Zeng, H. C. Little, T. N. Tiambeng, G. A. Williams, and Z. Guan, "Multifunctional dendronized peptide polymer platform for safe and effective sirna delivery," *Journal of the American Chemical Society*, vol. 135, no. 13, pp. 4962–4965, 2013.

[232] W. She, K. Luo, C. Zhang, G. Wang, Y. Geng, L. Li, B. He, and Z. Gu, "The potential of self-assembled, ph-responsive nanoparticles of mpegylated peptide dendron-doxorubicin conjugates for cancer therapy," *Biomaterials*, vol. 34, no. 5, pp. 1613–23, 2013.

[233] H. Lu, J. Wang, Y. Lin, and J. Cheng, "One-pot synthesis of brush-like polymers via integrated ring-opening metathesis polymerization and polymerization of amino acid n-carboxyanhydrides," *J Am Chem Soc*, vol. 131, no. 38, pp. 13582–3, 2009.

[234] T. Aliferis, H. Iatrou, and N. Hadjichristidis, "Living polypeptides," *Biomacromolecules*, vol. 5, no. 5, pp. 1653–6, 2004.

[235] D. A. Gewirtz, "A critical evaluation of the mechanisms of action proposed for the antitumor effects of the anthracycline antibiotics adriamycin and daunorubicin," *Biochem Pharmacol*, vol. 57, no. 7, pp. 727–41, 1999.

[236] A. A. Lane and B. A. Chabner, "Histone deacetylase inhibitors in cancer therapy," *J Clin Oncol*, vol. 27, no. 32, pp. 5459–68, 2009.

[237] M. S. Kim, M. Blake, J. H. Baek, G. Kohlhagen, Y. Pommier, and F. Carrier, "Inhibition of histone deacetylase increases cytotoxicity to anticancer drugs targeting dna," *Cancer Res*, vol. 63, no. 21, pp. 7291–300, 2003.

[238] P. N. Munster, D. Marchion, S. Thomas, M. Egorin, S. Minton, G. Springett, J. H. Lee, G. Simon, A. Chiappori, D. Sullivan, and A. Daud, "Phase i trial of vorinostat and doxorubicin in solid tumours: histone deacetylase 2 expression as a predictive marker," *Br J Cancer*, vol. 101, no. 7, pp. 1044–50, 2009.

[239] B. Groselj, N. L. Sharma, F. C. Hamdy, M. Kerr, and A. E. Kiltie, "Histone deacetylase inhibitors as radiosensitisers: effects on dna damage signalling and repair," *Br J Cancer*, vol. 108, no. 4, pp. 748–54, 2013.

[240] M. Namdar, G. Perez, L. Ngo, and P. A. Marks, "Selective inhibition of histone deacetylase 6 (hdac6) induces dna damage and sensitizes transformed cells to anticancer agents," *Proc Natl Acad Sci U S A*, vol. 107, no. 46, pp. 20003–8, 2010.

[241] D. J. Callahan, W. Liu, X. Li, M. R. Dreher, W. Hassouneh, M. Kim, P. Marszalek, and A. Chilkoti, "Triple stimulus-responsive polypeptide nanoparticles that enhance intratumoral spatial distribution," *Nano Lett*, vol. 12, no. 4, pp. 2165–70, 2012.

[242] T. Suzuki, A. Kouketsu, A. Matsuura, A. Kohara, S. Ninomiya, K. Kohda, and N. Miyata, "Thiol-based saha analogues as potent histone deacetylase inhibitors," *Bioorg Med Chem Lett*, vol. 14, no. 12, pp. 3313–7, 2004.

[243] C. He, X. Zhuang, Z. Tang, H. Tian, and X. Chen, "Stimuli-sensitive synthetic polypeptide-based materials for drug and gene delivery," *Adv Healthc Mater*, vol. 1, no. 1, pp. 48–78, 2012.

[244] J. A. Engelman, "Targeting pi3k signalling in cancer: opportunities, challenges and limitations," *Nature Reviews Cancer*, vol. 9, no. 8, pp. 550–562, 2009.

[245] A. B. Heimberger, D. Suki, D. Yang, W. M. Shi, and K. Aldape, "The natural history of egfr and egfrviii in glioblastoma patients," *Journal of Translational Medicine*, vol. 3, 2005.

[246] D. Opel, M. A. Westhoff, A. Bender, V. Braun, K. M. Debatin, and S. Fulda, "Phosphatidylinositol 3-kinase inhibition broadly sensitizes glioblastoma cells to death receptor- and drug-induced apoptosis," *Cancer Res*, vol. 68, no. 15, pp. 6271–80, 2008.